

Quantifying the Effects of Type II Hot Corrosion on the High Temperature Fatigue Cracking
Behavior of a Ni-based Superalloy

A Thesis

Presented to the faculty of the
School of Engineering and Applied Science
University of Virginia

in partial fulfillment
of the requirements for the degree

Master of Science

by

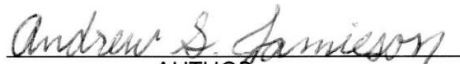
Andrew S. Jamieson

May

2018

APPROVAL SHEET

The thesis
is submitted in partial fulfillment of the requirements
for the degree of
Master of Science


AUTHOR

The thesis has been read and approved by the examining committee:

Prof. James T. Burns

Advisor

Prof. James M. Fitz-Gerald

Prof. Elizabeth J. Opila

Accepted for the School of Engineering and Applied Science:



Craig H. Benson, Dean, School of Engineering and Applied Science

May

2018

Abstract

This study investigates type II hot corrosion effects on the fatigue behavior of the nickel-based superalloy, ME3, also known as René 104. The primary application of ME3 is for turbine disks in the aerospace industry. Hot corrosion pitting caused by molten salt environments has been found to drastically reduce the fatigue life of ME3 components. A better understanding of the corrosion damage features/metrics and mechanisms that govern crack initiation is necessary to inform modeling of the safe remaining fatigue life of a corroded component.

High temperature fatigue testing was performed at two stress levels on samples that had two conditions of pre-corrosion which differed in salt concentration. Loading sequence induced markers on the fracture surface enabled the quantification of initiation life and small crack propagation life. Post-test fractography determined the crack initiation location which was analyzed in the context of the full distribution of damage on the surface obtained from pre-test topographic characterization. Specifically, corroded surfaces were characterized for various pitting metrics on both bulk and regional scales using white light interferometry. As expected, crack formation occurs at corrosion damage features. At low stress, the corrosion damage modestly reduced the crack initiation life, but the reduction was more significant at high stress. Furthermore, for all conditions, the primary fatigue cracks initiated at one of the largest 1% of pits, typically in regions of high pitting density. Such results provide novel insights into fatigue cracking evolution from corroded surfaces; furthermore, they support the common assumptions of using the deepest corrosion damage features as the initial damage feature in fracture mechanics based modeling of corroded components.

Contents

1	Introduction	6
1.1	Background	6
1.2	Corrosion and Fatigue	8
1.3	Goals	10
1.3.1	<i>Task I: Corrosion Characterization</i>	10
1.3.1.1	Objective	10
1.3.1.2	Bulk Surface Perspective	10
1.3.1.3	Regional Perspective.....	11
1.3.2	<i>Task II: Impact of Stress and Corrosion Level on Fatigue Behavior</i>	11
1.3.2.1	Objective	11
1.3.2.2	S-N Curve	11
1.3.3	<i>Task III: Analysis of the Crack Initiating Pits</i>	12
1.3.3.1	Objective	12
1.3.3.2	Bulk Surface Perspective	12
1.3.3.3	Regional Perspective.....	12
1.3.4	<i>Task IV: Crack Initiation and Crack Propagation</i>	12
1.3.4.1	Objective	12
1.3.4.2	Phase Dominance and Crack Growth	12
1.3.5	<i>Collaborators</i>	13
2	Methods	14
2.1	Tested Material	14
2.2	Testing Matrix	14
2.2.1	<i>Hot Corrosion Protocol</i>	16
2.2.2	<i>Corrosion Characterization</i>	17
2.2.2.1	Cleaning	17
2.2.2.2	White Light Interferometry	18
2.2.2.3	Data Processing.....	24
2.2.3	<i>Mechanical Loading Conditions</i>	29
2.2.3.1	Testing Equipment	33
2.2.3.2	Procedure	34
2.2.4	<i>Fracture Analysis</i>	37

2.2.4.1	Crack Initiation Site	38
2.2.4.2	Crack Initiation Region	38
2.2.4.3	Crack Initiation Life	39
2.2.4.4	Crack Growth	39
3	Results and Discussion	47
3.1	Task I: Corrosion Characterization	47
3.2	Task II: Impact of Stress and Corrosion Level on Fatigue Behavior	53
3.2.1	<i>Fatigue Life Results</i>	53
3.2.2	<i>Bulk Metrics</i>	54
3.3	Task III: Analysis of the Crack Initiating Pits	57
3.3.1	<i>Size Metrics</i>	57
3.3.2	<i>Localized Damage Region Metrics</i>	64
3.3.2.1	Pitting Density	68
3.3.2.2	Average Pit Size	69
3.3.2.3	Pit Spacing	72
3.4	Task IV: Crack Initiation and Crack Propagation	74
3.4.1	<i>Quantifying the Relative Roles of Crack Initiation and Propagation</i>	74
3.4.2	<i>Crack Growth Rates</i>	77
3.4.3	<i>Oxidation</i>	80
4	Summary/Conclusions	92
4.1	Task I: Corrosion Characterization	92
4.2	Task II: Impact of Stress and Corrosion Level on Fatigue Behavior	93
4.3	Task III: Analysis of the Crack Initiating Pits	93
4.3.1	<i>Pit Size</i>	93
4.3.2	<i>Region of the Crack Initiating Pit</i>	94
4.4	Task IV: Crack Initiation and Crack Propagation	95
4.4.1	<i>The Relative Roles of Crack Initiation and Propagation</i>	95
4.4.2	<i>Crack Growth Rates</i>	95
4.4.3	<i>Oxidation</i>	95
4.5	Future Work	96

1 Introduction

1.1 Background

Metal fatigue is a major concern in the aerospace industry due to its insidious manner of failure. Specifically, in many cases a component can demonstrate (or appear to demonstrate) normal performance until the instant it ruptures. The warning signs of component failure are seldom obvious without careful inspection prior to failure. Generally material fatigue failure occurs from at least one crack that has grown to a size such that the stress intensity (K), for the given operational loading condition and component geometry, exceeds the material fracture toughness. Therefore, it is important to understand where, when, and how a fatigue crack initiates. This study seeks to answer these questions for the nickel-based superalloy ME3, or René 104, whose primary application is in the aerospace industry as turbine engine disks.

Jet turbine disks must endure an arduous environment which includes high stress levels, high temperature, and corrosive environments. Higher operating temperatures are desired of turbine engines to increase their efficiency by being able to consume less fuel while achieving their desired performance levels. ME3 has the composition and metallurgical features to safely operate under such conditions. However, specialized processing and superior high-temperature properties for this material can come with a sacrifice of damage tolerance [1]. Furthermore, at higher operating temperatures, the turbine disks become more prone to hot corrosion where salt compounds from around and within the engine melt and serve as the corroding medium [2].

There are two classes of hot corrosion: type I and type II. They are distinguished by the temperature at which they occur. Type I hot corrosion occurs at temperatures above the melting point of sodium sulfate (884°C), and type II hot corrosion occurs below sodium sulfate's melting temperature [3]. General temperature ranges where type I and type II hot corrosion occur are 900°C-1000°C and 650°C-750°C, respectively [3]. As such, type I and type II hot corrosion are also known as high-temperature hot corrosion and low-temperature hot corrosion, respectively.

Turbine disks operate at temperatures around 1300°F, or 704°C [2,4]. Therefore, they experience type II hot corrosion which involves oxidation by salts whose sources include air intake, fuel (whether components or contaminants), combustion, and other parts of the engine [2,3,5–7]. The salt compounds are typically sulfates of sodium and magnesium (i.e. Na_2SO_4 , MgSO_4) [3,8–10].

Sodium sulfate is a particular threat to turbine disks in regions near the ocean where heightened amounts of sodium chloride can enter the engine by air intake and react with sulfur impurities in the engine fuel [3,7].

Though type II hot corrosion occurs below the melting temperature of pure sodium sulfate, the salt is still a threat in the type II hot corrosion temperature range because it can transform to a liquid on the ME3 surface with the assistance of solutes present in the environment and in the sulfate itself [3,11]. The solutes within the sulfate decrease the melting temperature of the compound, and material from the gaseous environment deposits onto the ME3 surface to further contribute to melt the salt as it contacts the disks [11]. Specifically, a mechanism that has been proposed to create the molten salt environment in type II hot corrosion entails NiO and CoO reacting with SO₃ in the gas to form sulfates that combine with solid Na₂SO₄, resulting in a liquid mixture of Na₂SO₄—NiSO₄ or Na₂SO₄—CoSO₄ [7]. NiO and CoO can be readily available on the surface of the Ni alloy by lying outside of the more stable passivating layer of Cr₂O₃ and/or Al₂O₃ [12–14]. The passivating layer could form inside the Ni and Co oxides due to their fairly high porosity to allow oxygen diffusion [12]. After the salt melts, either before or upon contacting the disks, the anions can electrochemically penetrate the protective oxide film of the ME3 surface (which, as mentioned above, consist of either a chromium oxide, Cr₂O₃, or an aluminum oxide, Al₂O₃ [3,7,9,15]) [2,16]. Corrosion pits (which are morphologically akin to craters but on the microscopic scale) form on the surface of the ME3 disks as a result.

These corrosion pits are a major concern for fatigue because these concave features on the material surface create local stress concentrations [6,17–22]. Though these stress concentrations are typically small, many of them are sufficient to result in local strain that induces cyclic plastic damage accumulation proximate to the pit, given cyclic loading that is sufficiently aggressive [23]. While there is general agreement that the accumulation of such local plastic deformation is a precursor of a crack (assuming the loading conditions continue) [24], there is ambiguity as to the precise combination of local damage accumulation and local stress that causes crack formation. To this end, various fatigue indicator parameters (FIP) have been postulated to quantitatively capture the combination of local conditions that lead to failure [25]. While such micro-mechanical modeling is outside the scope of this study, this effort aims to quantitatively characterize and

understand the relevant features of the type II hot-corrosion damage that impacts the fatigue behavior (crack initiation, small crack propagation, and overall fatigue life) of ME3.

1.2 Corrosion and Fatigue

Corrosion pits, generated via the hot corrosion process where the high temperature produces the molten salts and accelerates the oxidation, are a threat to the fatigue resistance of a material [10]. Prior work has demonstrated that corrosion can reduce the fatigue strength of a material by 50-80% [26–29]. It is thus not surprising that hot corrosion pits drastically reduce the fatigue life of a turbine disk alloy [2,9,30], thus strongly impacting its structural integrity [31]. Specifically, the fatigue life of ME3 has been found to be reduced by up to 98% due to hot corrosion pitting at 704°C [2]. Furthermore, Pao et al. [32] observed 300- μm fatigue cracks occurring two to three times earlier from pitted surfaces compared to pristine surfaces. As such, it is critical to understand how corrosion pitting will impact fatigue failure of materials while they are in service, especially materials that serve the aerospace industry. While it is known that hot corrosion pitting is a serious fatigue hazard, a further understanding of the features of hot corrosion damage that govern crack formation would inform more rigorous quantitative modeling that aims to predict the remaining useful life of a hot-corroded component.

Various studies exist in the realm of corrosion and fatigue that focus on the fatigue crack initiating feature. Pit size is commonly taken to be a critical factor as cracks tend to initiate at large pits with the factor of pit depth receiving particular attention [21,22,33–36]. Zhou and Turnbull [21] showed that a maximum pit depth of 35 μm decreased the endurance limit of a turbine blade steel by a stress range of at least 100 MPa. There have been speculations of critical pit depth [35,37–40], diameter [41], as well as both depth and diameter [2,19,36,42] that govern fatigue crack initiation for certain materials and conditions. It has been shown that the maximum stress concentration factor at a pit increases with an increased aspect ratio: depth/diameter [19,36,43].

Limited research has been conducted to characterize the pit that nucleates the fatigue cracking in the context of the overall distribution of pitting on a sample/component. In one study involving pitting and fatigue [40], the additional parameter of pitting density (amount of pits per unit area) on a stainless steel was included. Huang et al. were interested in the correlation of pitting density with time in a corrosive environment and compared pitting density growth rates among different loading modes, showing that pitting density grows faster under proportional loading than both non-

proportional and no loading. They also showed that the pitting density tends to plateau after long periods of time. However, they did not correlate pitting density values with fatigue life at the point of crack initiation or failure. Ishira et al. [41] also assessed pitting density under fatigue loading; but as their primary interest was in pit initiation and growth, they did not go as far as to connect pitting density with crack initiation or failure. Pitting density was also determined in the study of Mohammad et al. [44] but in relation to the concentration of corrosive material and to the duration of corrosion and not in relation to fatigue behavior. They noted that future work should be done on making connections between pitting density (as well as pit spacing) and the transition to fatigue cracking. Rozman et al. [45] connected pitting density with fatigue behavior but for two different alloys; as such they could not show the effects of pitting density for the same material at discrete stress levels. Pit spacing (the distance between pits) lacks experimental study even more than pitting density. However, it is noteworthy that in the modeling approach of Kolios et al. [19], it was shown that lower pit spacing resulted in increased stress concentration.

Average pit size, as represented by average pit depth, has been investigated as to how it affects fatigue behavior. King, Jr. [37] found a large variance in the fatigue life at the same stress level among different aluminum alloys that had similar average pit depths. Ghosh et al. [46] found the average pit depth to affect the S-N curve of an aluminum alloy, showing decreased fatigue life with increased average pit depth. They also showed maximum pit depth correlating with average pit depth in that study. Child et al. [47] found similar trends as Ghosh et al. for a nickel-based superalloy. Relations between average pit diameter and fatigue were not investigated in these studies. In the studies of Ghosh et al. and Child et al., pit depth was correlated with exposure time to a corroding salt solution (NaCl for the aluminum alloy, and NaSO₄ for the nickel alloy). As such, the decreased fatigue lives on the S-N curves were attributed to exposure time. The effect of salt concentration (with constant exposure time) in an aqueous solution was also evaluated by Donahue and Burns [48] where they found that the fatigue life of a stainless steel was inversely related to salt concentration. Therefore, exposure time to a salt solution, as well as salt concentration in a solution, deleteriously impacts the S-N curve of an alloy.

Limited research has been conducted to hone the perspective of the impact of the corrosion damage on fatigue to a smaller scale, local to the crack initiation site on the sample surface. Co and Burns [49], however, took this approach for pitting density in the region of the fatigue crack initiation

site and found that it showed large variability and that the crack initiation site occurred in the regions of neither the highest nor the lowest pitting density. This finding suggested that pitting metrics on a more local scale do not necessarily predict the location of a crack initiation site, but more research on the regional level is needed.

Given that an increased degree of corrosion (i.e. longer exposure times to a salt and higher salt concentrations) has been shown to degrade the fatigue performance of various alloys, the criticality of the pitting metrics of the corrosion is not fully understood. The lack of understanding of the interactions between corrosion and fatigue complicates modeling to predict the fatigue behavior of an alloy under hot corrosion conditions. Better understanding, incorporating the ability to predict a fatigue event like crack initiation, will allow hot-corroded components of turbine engines to be either repaired or retired before fatigue failure occurs. Such prediction capabilities will better ensure the safety and utility of turbine engines. As ME3 plays a vital role in the aerospace industry as an important component in jet turbine engines, this study illustrates relationships between various corrosion characterization metrics and the fatigue behavior of ME3.

1.3 Goals

1.3.1 Task I: Corrosion Characterization

1.3.1.1 Objective

This task aimed to characterize the corrosion damage on each corroded sample with pitting metrics from the bulk (entire surface) perspective and the regional (local) perspective.

Differences in these metrics were assessed between the two corrosion categories which were based on the corroding salt mixture: low salt concentration (LSC) and high salt concentration (HSC).

1.3.1.2 Bulk Surface Perspective

Characterization of the corrosion damage had to be accomplished before fatigue testing. Two different salt concentrations were assessed, each with the same exposure time. Pitting metrics within each salt concentration category were gathered for each sample to describe the severity of the corrosion. Pitting metrics included pitting density, pit diameter, pit depth, and pit spacing.

Pit count of all pits greater than 3 μm in both diameter and depth were determined for each sample. This count was needed to determine the pitting density on each sample in terms of the number of

pits per unit area. The two categories of salt concentration were then compared to each other with respect to pitting density.

Pit diameter and pit depth were the metrics used to describe the size of the pits. Distributions of diameter and depth were constructed to show the amount of pits in specified size ranges. The diameter and depth for each pit was also used to determine the average pit diameter and average pit depth among all pits that were included in the pit count for each sample. As with pitting density, the salt concentration categories were compared with respect to pit size.

Any trends that appeared between pitting density and pit size metrics were noted.

1.3.1.3 Regional Perspective

Pitting density and average pit size metrics were broken down to a regional level. Pit spacing, the average nearest neighbor distance between pits, was also included on this level. Each region was equal to each other region in surface area and was individually identified.

The purpose of this regional characterization was to identify where the fatigue crack initiated after testing and assess the pitting metrics in that region where the crack initiated. The metrics of the crack initiation region were then compared relative to all other regions on the sample surface.

The regional analysis was necessary to determine the significance of pitting metrics in the vicinity of the fatigue crack initiation site.

1.3.2 Task II: Impact of Stress and Corrosion Level on Fatigue Behavior

1.3.2.1 Objective

The objective of Task II was to assess the impact of the corrosion level (i.e. LSC and HSC) on the fatigue life of ME3. Effects of corrosion level on fatigue life were analyzed in light of bulk metrics.

1.3.2.2 S-N Curve

After fatigue testing, the general impact of corrosion on the fatigue behavior was analyzed from a general standpoint of the two categories of salt concentration. Beginning with a broad picture, a plot of stress vs. total fatigue life (S-N curve) was evaluated based on salt concentration.

Narrowing this analysis, a more specific evaluation of the results of this curve was then discussed based on the bulk pitting metrics of overall pitting density and average pit size.

1.3.3 Task III: Analysis of the Crack Initiating Pits

1.3.3.1 Objective

This task analyzed the fatigue crack initiating pits on from the bulk perspective and the regional perspective. The objective from the bulk perspective included comparing the size of the crack initiating pits to the overall distribution of pit sizes for each sample. The objective from the regional perspective compared the pitting density, average pit size, and pit spacing of the region of primary crack initiation to all other regions on each sample.

1.3.3.2 Bulk Surface Perspective

The primary fatigue crack initiation site (the initiation site of the crack that ultimately led to failure) was located on the fracture surface and specimen surface where the depth and diameter, respectively, of the crack initiating pit were determined. The diameter and depth of that pit was marked on the appropriate bin of the pit diameter distribution and pit depth distribution, respectively, for each corroded sample. This revealed how the size of the crack initiating pit compared to the rest of the pit sizes on each sample.

1.3.3.3 Regional Perspective

The focus of the impact of corrosion on the fatigue behavior was then shifted to the region of the fatigue crack initiation site. The metrics included average pit diameter, average pit depth, pitting density, and average nearest neighbor pit distance. The crack initiation region was compared to all other regions with respect to each regional metric on each sample. Any trends were noted to show the importance of each of these metrics on the regional scale for initiating a fatigue crack that led to failure.

1.3.4 Task IV: Crack Initiation and Crack Propagation

1.3.4.1 Objective

The objective of the fourth and final task was to determine relative magnitude of the crack initiation and crack propagation stages and their contribution to the overall fatigue life. Crack growth rates were then assessed for the crack propagation life.

1.3.4.2 Phase Dominance and Crack Growth

The crack initiation life—the number of cycles it took to achieve a fatigue crack of a certain small size—was determined. It was compared to the total fatigue life for each sample. The contributions

of crack initiation life vs. total fatigue life was determined based on the categories of stress level and salt concentration. Fatigue crack growth rates during crack propagation were also compared between these categories.

1.3.5 Collaborators

A few collaborators were involved with certain aspects of this study. NASA provided the original lot of ME3 fatigue samples, and Southwest Research Institute (SwRI) performed the pre-corrosion for eight samples before the corrosion damage was characterized. NASA also assisted in developing the cleaning protocol for the corroded samples. NASA and SwRI further provided certain mechanical property data of non-corroded (pristine) ME3, including fatigue life, elastic modulus, and fracture toughness.

The results of this study were used to inform the work of these collaborators in addition to the work of Elder Research Inc. SwRI and Elder Research have sought to produce fracture mechanics based models that account for the effect of hot corrosion damage on the fatigue behavior of ME3. The results of this study are used to evaluate these models.

2 Methods

2.1 Tested Material

The study is centered on the material system ME3 which has a nominal chemical composition of 50.3Ni-20.3Co-13.1Cr-3.8Mo-3.6Ti-3.5Al-2.3Ta-2.0W-1.0Nb-0.05Zr-0.04C-0.03B [50,51]. The samples were processed via powder metallurgy for more control of grain size given a relatively high fraction of a γ' phase and solid solution strengthening elements compared to other Ni-based superalloys [1,6,51]. Consequently, ME3 demonstrates excellent mechanical performance at high temperature, including fatigue behavior [51]. Room temperature mechanical properties include a nominal elastic modulus of ≈ 238 GPa, a yield strength of ≈ 1500 MPa, and a fracture toughness of ≈ 70 MPa-m^{1/2}. After testing, several Vickers hardness tests were done on multiple cross sections of the middle portion (gauge section) of two samples where only elastic loading was experienced. Vickers hardness, H_V , can be used to estimate the yield strength using the following relationship:

$$H_V = \frac{\sigma_y}{c} \Rightarrow \sigma_y = cH_V$$

H_V resulted in roughly 504. The unitless value for c is typically between 3 and 3.3 [52–54]. For a conservative estimate, 3 was used for c to determine the yield strength of this lot of ME3. As mentioned, the lot was provided by collaborators at NASA; however, its yield strength is higher than what was reported by NASA in a previous ME3 study [55].

2.2 Testing Matrix

The fatigue testing matrix (Table 2.2.3.a) consisted of eight corroded samples (which were corroded with either low or high salt concentration) and two non-corroded (pristine) samples. These were further divided into two stress categories (low and high stress). The pristine samples served as an accompanying comparison as the corroded samples were of primary interest for this study. Figure 2.2.a provides a visual comparison between a pristine sample and a corroded sample. The gauge section is the 20-mm portion of the specimens which is where fatigue cracking was expected to occur as it had the smallest cross-sectional area on each sample.

This section (2.2) details how the samples were corroded, the corrosion characterization method, the mechanical testing system/arrangement, and the fracture surface analysis techniques.

Pristine Corroded



Pristine

Corroded

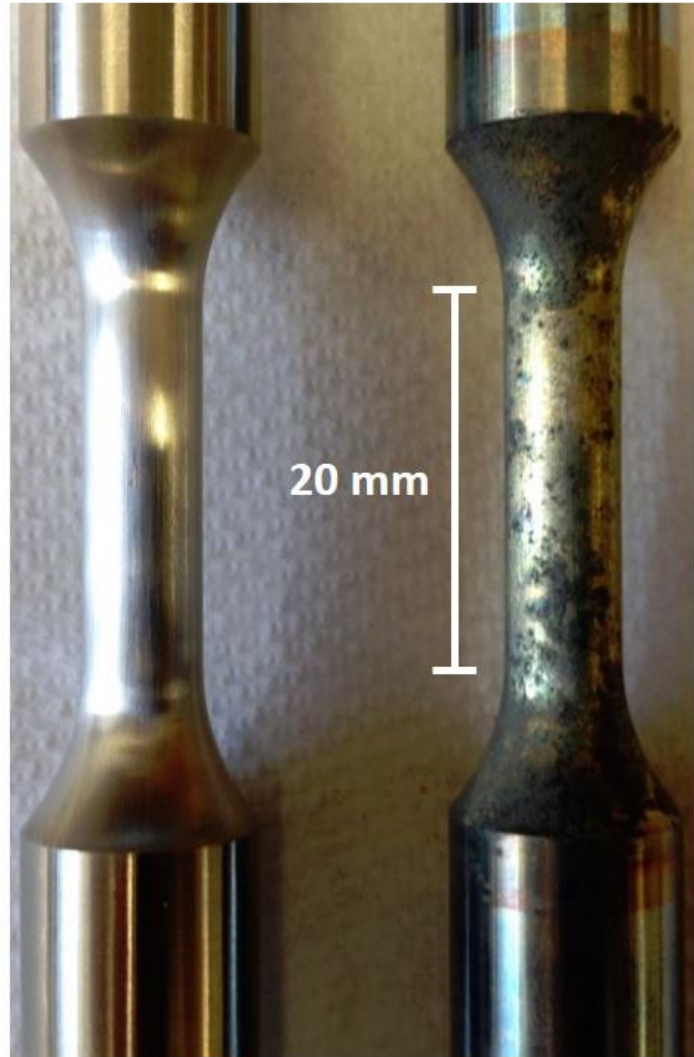


Figure 2.2.a

Visual comparison between ME3 fatigue samples: one pristine and one corroded. The gauge section of the samples was 20 mm in long (as indicated). High salt concentration was used for the corroded sample as detailed in Section 2.2.1. The image was taken after cleaning of the corroded specimen as explained in Section 2.2.2.1.

2.2.1 Hot Corrosion Protocol

Four of the corroded samples were baked with a solution of low salt concentration at 704°C (1300°F) for two hours, and the other four were baked with high salt concentration at 704°C for two hours. The corrosion process was performed by collaborators at Southwest Research Institute.

The salt consisted of a mixture of sodium sulfate (Na_2SO_4) and magnesium sulfate (MgSO_4) in deionized water (H_2O). The water was separated from the sulfates by evaporation then boiling at 110°C, leaving a solid salt mixture behind. Cellulose and alcohol were added to the salt mixture to form a paste that could be applied with a paintbrush to the surface of the fatigue samples. A layer of this salt paste (> 3 mm thick) was applied to each sample that was to be corroded, and each sample was rotated under a hot lamp until the salt mixture was dry. The sample was weighed after it cooled. This weight was compared to the sample weight before application of the salt to measure a salt concentration on the surface of each sample in milligrams per square centimeter. The samples that were corroded with low salt concentration had a surface concentration of ≈ 2 mg/cm^2 , and those that were corroded with high concentration had a surface salt concentration of ≈ 30 mg/cm^2 . Exact concentrations for each sample are displayed in Figure 2.2.1.a.

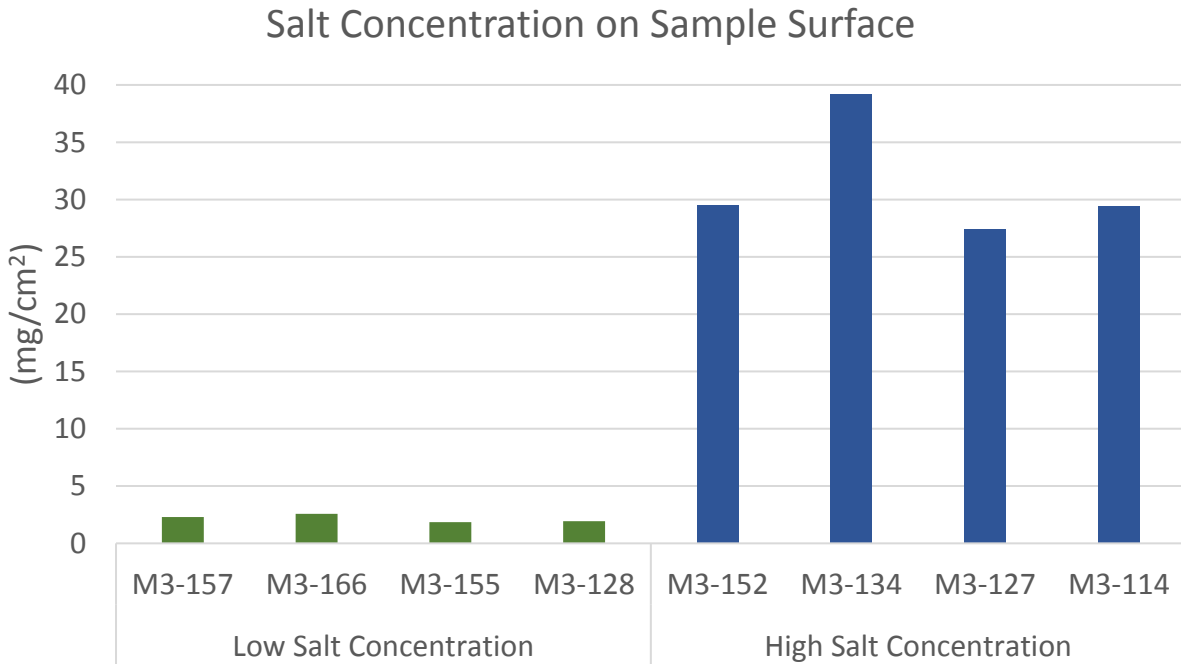


Figure 2.2.1.a

Surface salt concentrations with which the ME3 samples were corroded for 2 hr at 704°C.

2.2.2 Corrosion Characterization

An important piece of this study was to characterize the corrosion damage on two sets of samples differing the salt concentration by which they were corroded. A 3D characterization technique was necessary to capture the topographic features on the cylindrically shaped sample surfaces. A characterization method was developed which utilized the white light interferometry (WLI) technique. To rigorously measure the corrosion features, challenges included: (1) the presence of corrosion product that would obfuscate a direct view of the true damage to the sample surface and (2) the rounded nature of the cylindrical surface. A specialized characterization method was formulated and validated to address these challenges.

2.2.2.1 Cleaning

To ensure that the 3D WLI characterization captures the true damaged surface morphology of the ME3 material, it is necessary to remove the corrosion product which resulted from the two-hour hot-corrosion bake at 704°C. This cleaning enables accurate characterization of the pitting metrics, thus, the ability to analyze pitting metrics as they relate to the fatigue behavior of the material. This approach bypasses any speculations of pit-to-crack mechanisms that involve pit growth competing with crack growth [56] to strictly focus on crack initiation from fixed, known pitting morphology.

The cleaning protocol was developed in collaboration with personnel at NASA Glenn Research Center. Various protocols were tested which involved sonicating corroded ME3 surfaces in multiple solutions. The following protocol was finalized, but it was found (both at UVa and NASA) that a limited amount of corrosion product would remain on the surface no matter the severity of the cleaning protocol.

The cleaning protocol for each corroded sample began with sonication, for at least ten minutes, of the cylindrical gauge section which was fully immersed in a beaker of acetone to detach loose salt. This first step was followed by the second and third steps which were the same as the first but with the gauge section immersed in de-ionized (DI) water and methanol, respectively. The DI water cleaned residual product leftover from the acetone step. The methanol extracted leftover product that might have been caught with water in tight crevices. The final step was also similar to the first three (particularly to step two: sonication of the gauge section in DI water), but the DI water

was boiling at the commencement of sonication, and the sample was left to be sonicated for at least 12 hours after which it was rinsed in DI water and air-dried.

2.2.2.2 *White Light Interferometry*

White light interferometry (WLI) was the microscopy technique used to scan the corroded, then cleaned, sample surfaces using a Zygo NewView 7300. This technique has been utilized in multiple studies to characterize corrosion topography because of its ability to acquire efficient, non-invasive (non-contact), high-resolution, 3D measurements of a specimen surface [57–62]. A challenge that comes with WLI in this study is that the sample surfaces are cylindrical, not flat. This poses a threat to the accuracy of measuring true pit morphology for pits that sit at oblique angles, θ , from vertical alignment with the WLI lens during a scan. To illustrate this challenge, Figure 2.2.2.2.a shows a scenario in which $\theta = 45^\circ$. One scan in this case would cover 90° (with the center of the scan being the top of the rounded surface). Assuming a pit depth of $10\ \mu\text{m}$, the perceived pit depth is as shown in Table 2.2.2.2.a in reference to Figure 2.2.2.2.a for various angles, θ .

Decreasing the scan from 90° to 20° causes θ to decrease from 45° to 10° , greatly reducing the error involved with the curvature of the specimen, thus, with the morphology of the pit. As such, the maximum error is reduced to 1.5 % by making the scan increments as small as 20° (- to + 10° about the vertical). This is the maximum possible error by reducing the scan interval to 20° as nearly all pits lie somewhere inside each - to + 10° increment, including many pits situated closer to 0° . By fixing each scan to 20° increments, 10° is the maximum rotational location where a pit can be located in a scan. 20° scan increments amply cover the pitting topography of the sample surface. In Figure 2.2.2.2.a, a hemispherical pit geometry was assumed, and this geometry was actually an aggressive estimate for a typical pit on this ME3 material as most pits have diameters that are larger than twice their depths. Even with a hemispherical pit, light can still reach the bottom of the pit if the sample were rotated about its longitudinal axis by 45° . With the rotational increment between scans set to be 20° , 18 scans were required on each specimen to complete a full set of scans completing 360° around the sample. Each scan would have the format of - and + 10 degrees from vertical.

In preparation for each session of scanning, the functionality and accuracy of the interferometer was checked with a standard specimen which had a perfectly flat surface with incisions of known

depth. The walls of these incisions were also flat and perpendicular to the bulk surface, and the bottom of the incisions were flat as well. The depth of the incisions were 1.8 μm . A one-frame scan was taken of a section of this standard with an incision in the frame. The results of this scan were checked to have flat surfaces and the depth of the incision was checked to be within about 0.02 μm of 1.8. The standard was then removed from the stage and a corroded ME3 fatigue sample was placed in the specimen holder and positioned such that the gauge section lied under the objective lens.

Strict positioning of the specimens was assured before each scan. A specimen holder was designed especially for these samples which kept them in stable position for the scans and also included tick marks on the edge, spaced exactly 20-degrees apart, for precise 20-degree rotations between scans. As the sample sat in the holder, it was positioned such that each individual scan was assured to be parallel to the longitudinal dimension of the gauge section as another measure to preserve the precision of the array of 18 20-degree scans. Each scan was also assured to cover 20 millimeters (mm) along the longitudinal dimension as this was found to be the gauge length outside of which the longitudinal curvature of each specimen began to increase rapidly.

The samples each had a slightly tapered portion in the middle of the gauge section, accounting for a maximum of five microns in attenuated diameter which could not be noticed by the unaided eye but was enough to see under the microscope. As this attenuation was viewable under the WLI microscope, it enabled the center of each gauge section to be located which was where the attenuation was maximum. The lens was focused on this center section. The focusing mechanism was based on fringes present in the frame, not merely by sharpness of the image. The fringes are visible under the microscope as a set of light and dark streaks that form from the interference of light. They appear in the field of view on the specimen surface wherever the microscope is in focus.

The interferometer had two scan types: bipolar scan and extended scan. Bipolar could scan up to a depth range of 75 μm above and 75 μm below the depth of the point of focus (indicated by the depth of the fringes in the live image). As such, it can scan a depth range of 150 μm . In this case, the scan begins 75 μm above the set depth of focus and proceeds to scan down to 75 μm below. Extended scan begins at the depth of focus and proceeds to scan up to the amount at which the extended scan was set (up to a maximum of 500 μm).

Both of these scanning modes were tested on the same material surface. Both resulted in about the same number of data points for the desired depth range of 150 μm . Aside from this similarity in quality of scanning, another factor in the comparison between a bipolar-150- μm scan vs. an extended 150- μm scan was a matter of utility. Using the bipolar mode was more convenient because the home depth of focus was able to be set in the middle of the desired 150- μm depth range rather than at the bottom of that range. Thus, there was no need to move the focus down after finding the center of the depth of focus for the scan. As such, the bipolar mode of scanning was preferred over the extended mode. With a desired depth range of 150 μm , the bipolar mode was confirmed to consistently reach at least 300,000 data points out of the possible 307,000 for a single-frame scan (Figure 2.2.2.2.b). Therefore, the bipolar scan mode was used for all scans with a range of 150 μm which was sufficient to assure coverage of each 20-degree scan along the gauge section of each sample.

The 5X power lens was used for the scans because it was able to span 20 degrees in a single frame and still have high resolution (2.183 μm laterally). This benefit helped maintain control of the microscope within and between scans as each scan could start from the top of the gauge section, directly overhead the peak of the lateral curvature of the sample, and scan straight to the bottom of the gauge section without requiring any left or right movement. This also enabled more efficient data collection as it required less frames per scan, allowing for an entire sample to be scanned in a single day which furthermore helped to have consistent scans for each sample. The maximum number of data points the interferometer could output per frame with the 5X power lens was 307,000. As the scans reached closer to this number of points, the topography measurements were more representative of the actual specimen surface topography.

Dual light stitch settings had to be optimized for the WLI scans. It was found that dual light stitch settings of about 95 % light level and a 1.00-1.20 % offset above the light level consistently yielded the most data points for each scan (Figure 2.2.2.2.c). The former setting served as the primary light level of a subscan for each dual frame sub-scan of a full 20° scan of the gauge section; and the latter served as the secondary light level of the sub-scan for each frame. A light level of 90-100 % was recommended by the manufacturers. The offset was determined based on the light level of the baseline frame of the scan (in the center of the gauge section). For example, if the live image appeared brighter than normal at a 95% light level, the light level could be decreased to

90% and the offset increased to 1.2%; or if the image appeared darker than normal at 95%, the light level could be increased to 99% with a decreased offset at 1.0%. In such cases, setting the light level and offset became somewhat of an art to achieve the highest amount of data points possible.

The brightness of the live image could vary depending on the position and topography of the sample's surface which could require slight adjustments in the light level and/or offset in which case the scanning becomes a bit of an art. The objective is to acquire as many data points in the scan as possible. If either the light level or offset are either too high or too low, data points could be lost in which case the topography measurements would be less representative. For example, if the image is brighter after rotating the specimen 20°, the light level, light offset, or both could be decreased. If both are decreased, neither setting should be reduced by more than about half of the amount it would be reduced by if only that single setting were decreased. Fortunately, this matter was not much of a concern because the surfaces that were scanned did not differ much (in either position or topography) from either one increment to the next, or from one sample to the other, even with varying levels of corrosion damage.

In the end, the corroded samples each had 18 scans at 20° increments to cover the entire 360° cylindrical surface. Each scan was done in the bipolar mode with a 150- μm depth, sufficiently covering - and + 10° from the vertical for each of the 18 scans. The light level was determined to be optimal at 95% with adjustments that could be made between 90% and 100%, according to the brightness of the live frame. The optimal light offset was between 1.0% and 1.2%, depending on the brightness of the live image and the deviation from 95% light level (e.g. higher light level: lower offset; lower light level: higher offset).

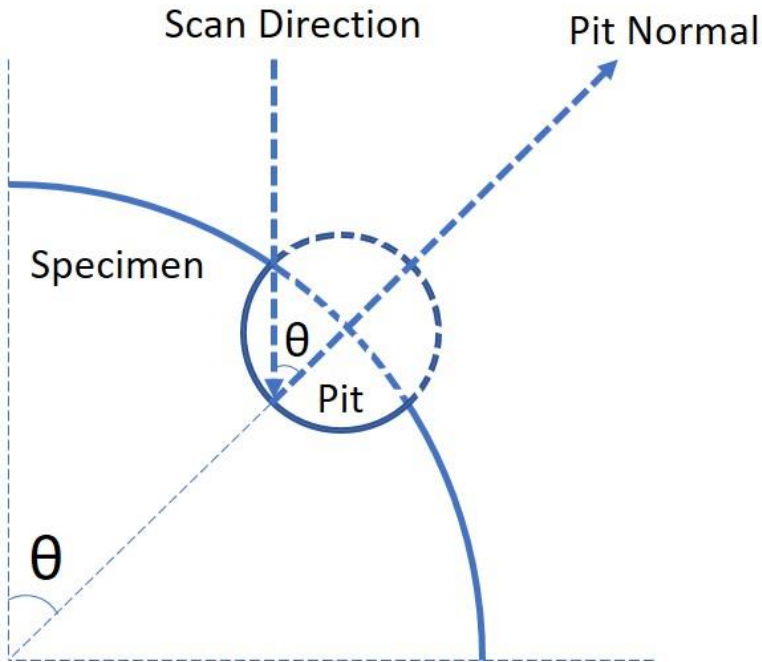


Figure 2.2.2.2.a

Schematic diagram of a cross section of a WLI scan over the gauge section of a corroded sample with a theoretical pit. As shown, $\theta = 45^\circ$, sufficient to detect the bottom of the pit but with error. Actual maximum θ for the WLI scans was 10° .

$$\text{perceived pit depth} = 10\mu\text{m} \cos \theta$$

Rotation from vertical	$\theta = 5^\circ$	$\theta = 10^\circ$	$\theta = 20^\circ$	$\theta = 45^\circ$
Perceived pit depth (μm)	9.96	9.85	9.40	7.07
Relative error	0.4 %	1.5 %	6 %	29 %

Table 2.2.2.2.a

For an ideal hemispherical pit having an actual pit depth of $10\ \mu\text{m}$, this table shows the perceived pit depth and associated relative error for various rotations, θ , from vertical alignment with the objective WLI lens.

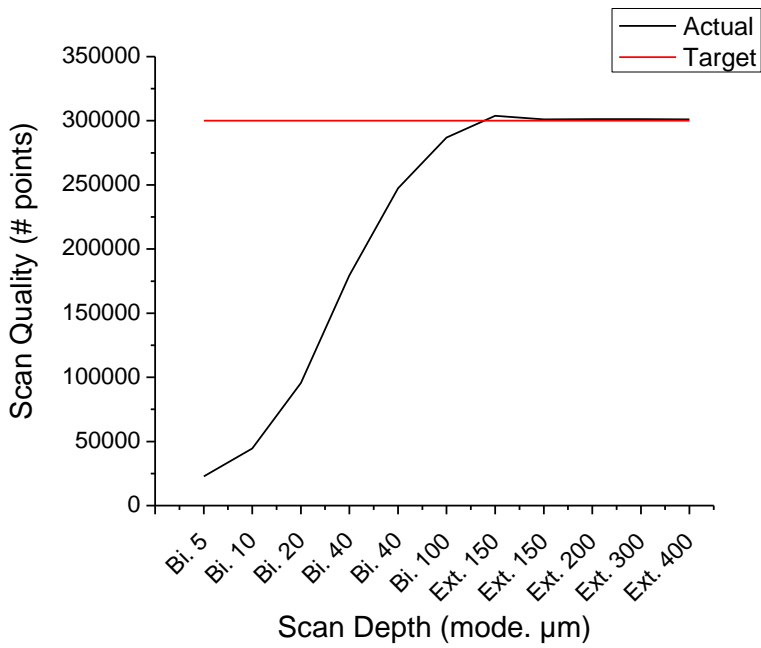


Figure 2.2.2.2.b

150- μm scans in the bipolar mode of WLI produced at least 300,000 data points (the target amount) per frame.

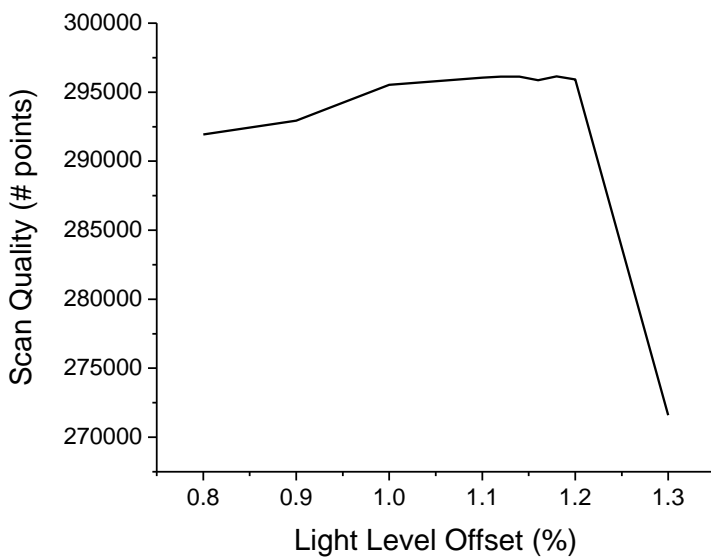


Figure 2.2.2.2.c

Given a light level of 95% for WLI, the optimum range of the light offset was 1.0-1.2%.

2.2.2.3 Data Processing

After the interferometry scans were completed, the data from those scans were processed in a software program called MountainsMap and subsequently filtered in Excel, ImageJ, and Matlab depending on the desired pitting metrics. Processing protocols were developed using the software to organize the WLI data to obtain the metrics of pit count, pit diameter, pit depth, and pit spacing on the on a bulk level (for the entire surface) and regional level (by dividing the surface into smaller regions of equal size).

Before proceeding with this processing, the definition of a pit had to be determined by defining minimum pit size metrics of diameter and depth as well as an appropriate aspect ratio (diameter/depth) range. These pit morphology thresholds were to be determined based on empirical data. The WLI method was then validated by comparing empirical data to processed data.

2.2.2.3.1 Empirical Data

Empirical data of pit sizes were obtained by directly measuring the diameter and depth of pits using optical microscopy performed on cross sections. A preliminary ME3 fatigue sample, corroded by Southwest Research Institute, was used to obtain this data to compare with the WLI data of the same sample. The gauge section of this sample was cleaned with the protocol previously described and cut with a saw into several lateral cross sections along its cylindrical gauge section. These sections were then polished along the same faces that were cut to enhance the exposure of pits in the cross section of the corroded surface under a Hirox KH-7700 digital optical microscope.

Under the optical microscope, features that appeared to possibly be pits with a diameter or depth of less than 3 μm were frequently questionable as to whether they were actually pits. Identification of actual pits was easy when the diameter and depth of the pit-like feature was greater than 3 μm . This fit the resolution for the 5X power lens on the Zygo white light interferometer which had a lateral resolution of 2.183 μm . Data for approximately 50 pits was obtained from the cross sections. For the aspect ratio, reasonable slack was added to both the high and low ends of the range of aspect ratios from the empirical data due to the cross sections not necessarily representing the entire population of potential pits on the corroded samples. Ultimately, the morphology of a pit was defined as having an aspect ratio (depth/diameter) of within 0.08 and 2 in addition to having

a minimum diameter and depth of 3 μm each. This data was to be later compared with the processed data from the WLI scans to validate the scanning and processing method.

2.2.2.3.2 WLI Data Processing Protocols

For a single sample, each individual WLI scan (of the set of 18) was cropped to a 20-degree width and a 20-mm height. The resultant area was then separated into five sections which were each 4 mm in height. This separation into five sections served a dual purpose: (1) to assist the function of removing curvature/undulation of the bulk surface of the gauge section for subsequent measurements of the corrosion pits and (2) to divide the gauge section into five rows of regions along the axial dimension of the gauge section for regional analysis of pitting metrics.

Splitting the gauge section into five parts in the longitudinal (axial) direction for each scan helped diminish curvature in for the form removal step about a lateral axis. The first and fifth sections (top and bottom, respectively) had the most curvature about the lateral axis of the gauge, the second and fourth sections were less curved about the lateral axis but more curved about the longitudinal axis, and the middle section had the least curvature about the lateral axis but the most curvature about the longitudinal axis. These differences in curvature were minimal, accounting for an overall dimensional difference between the middle of the third section and the edges of the outer sections of 9 μm in the lateral dimension and 25 μm in the longitudinal dimension.

The purpose of the form removal function in MountainsMap was to transform the curved bulk surface of each scan into a flat surface. This flat surface provides a single vertical reference point for any local undulations such as pits. As such, the form removal function flattened the bulk curvature of the surface of the gauge section of each sample while retaining the presence of pits. The form removal setting of “polynomial order 4” sufficiently removed the curvature of the bulk surface as shown in Figure 2.2.2.3.a where the curvature is color-coded according to depth. Before form removal, depth varies throughout the section; and after form removal the depth of the bulk surface is constant while showing pit depth measurements with respect to that surface.

These five sections (for each of the 18 scans) were also utilized for constructing a grid for regional analysis of pitting metrics. For each of the five rows of the gauge section, the 18 20-degree sections were combined into sets of three adjacent sections. With an average diameter of 6.36 mm in the gauge section, this arrangement created 30 regions on the gauge section of nearly square form: 4

mm × 3.33 mm. As such, each region had an area of 13.3 mm², together comprising a total area of 400-mm² on the gauge section.

After this geometric processing, the “volume of islands” function was performed. For this function to work, the data for each scan needed to be mirrored about the plane of the surface (hence, the pits became islands as they protruded above the surface instead of below). This mirroring also caused the data of pit depth to become positive instead of negative. The “water level” for the volume-of-islands function was set to 3 μm above the average bulk surface, exposing all pitting deeper than 3 μm. After setting the water level (depth threshold), the volume-of-islands function was set to record the diameter and depth of each pit. The diameter for each pit was the diameter equivalent to that of a circle if every pit were converted to a circle according to its area. The depth for each pit was the maximum depth that the interferometer measured within that pit.

At this point, the processing protocols split to two different routes. The objective of one route was to acquire the pitting metrics of pit count, diameter, and depth; the objective of the other was to acquire the metric of pit spacing.

2.2.2.3.2.1 Pit Count, Diameter, and Depth

With the minimum depth threshold set in MountainsMap at 3 μm, the 3-μm diameter threshold was also set. MountainsMap then provided diameter and depth data for each individual pit that passed the thresholds for these pit size metrics.

This data from MountainsMap was then filtered in Excel. A Visual Basic for Applications (VBA) code was developed to perform a final filter which included the aspect ratio thresholds. The purpose of this filtering was to expunge any data that appeared to represent pits but in actuality did not. In other words, this further processing removed any noise from the data that survived through MountainsMap. In Excel, the procedure began by adding 3 μm to the depth of all pits. As all pits that were above the 3-μm water level (depth threshold) in MountainsMap had depths relative to the water level, this three microns was added back to all pits. Afterwards, the aspect ratio threshold was set for all pits where every pit was required to fall within the range of 0.08-2; otherwise, the pit was considered invalid and was therefore discarded. Finally, all pits that survived the filters were counted. At this point, the data for the bulk surface metrics (representing the entire gauge

section) of pitting density (based on pit count), pit diameter, and pit depth was finalized and ready for analysis.

The characterization method was validated before proceeding to scan the remaining corroded samples—as well as determine the pit spacing—by comparing the empirical data from the preliminary sample to its processed WLI measurements in Figure 2.2.2.3.b. This plot validated the WLI method as the empirical data overlapped well with the WLI data. It also suggested that the cleaning protocol was sufficiently successful to justify its use.

2.2.2.3.2.2 *Pit Spacing*

The other processing route (from the point of setting the 3- μm pit depth threshold in MountainsMap) was then applied to each corroded sample to determine the average nearest neighbor distance (ANNd) between pits which was derived from a resource by a geographic information systems group, Esri [63]. ANNd was defined as the average distance from the center of each pit to the center of the pit that was located the shortest distance away. This metric was to be part of the regional data set for each sample to avoid the error that would accompany this metric at the bulk level.

The diameter threshold for ANNd was set at 5 μm in MountainsMap instead of 3 μm because it was found that a 3- μm diameter could not be resolved in later processing in ImageJ (an image processing software), but 5 μm could be resolved. Specifically, the 3- μm diameter threshold was found to cause a discrepancy of as much as 20% in pit count after further processing in ImageJ, primarily due to Image J's binarization function, causing some small pits (between three and five microns in diameter) to vanish. The 5- μm diameter threshold resulted in less than 5% of a pit count discrepancy when accounting for all pits that were at least 5 μm wide. Ultimately, the 2D coordinates of pits that were wider than 5 μm were determined in ImageJ.

The coordinate data were then taken to Matlab to compute the average nearest neighbor distance for each of the five sections of the 18 20-degree scans that contained more than one pit greater than 5 μm in diameter. The basic procedure in Matlab was to first, calculate the distance between each pit and all other pits; second, determine the minimum of those distances (nearest neighbor) for each pit; and third, calculate the average of those minimum (nearest neighbor) distances. The

resulting ANNd data were combined by weighted average for the three sections in each of the 30 regions on the gauge section of each corroded specimen.

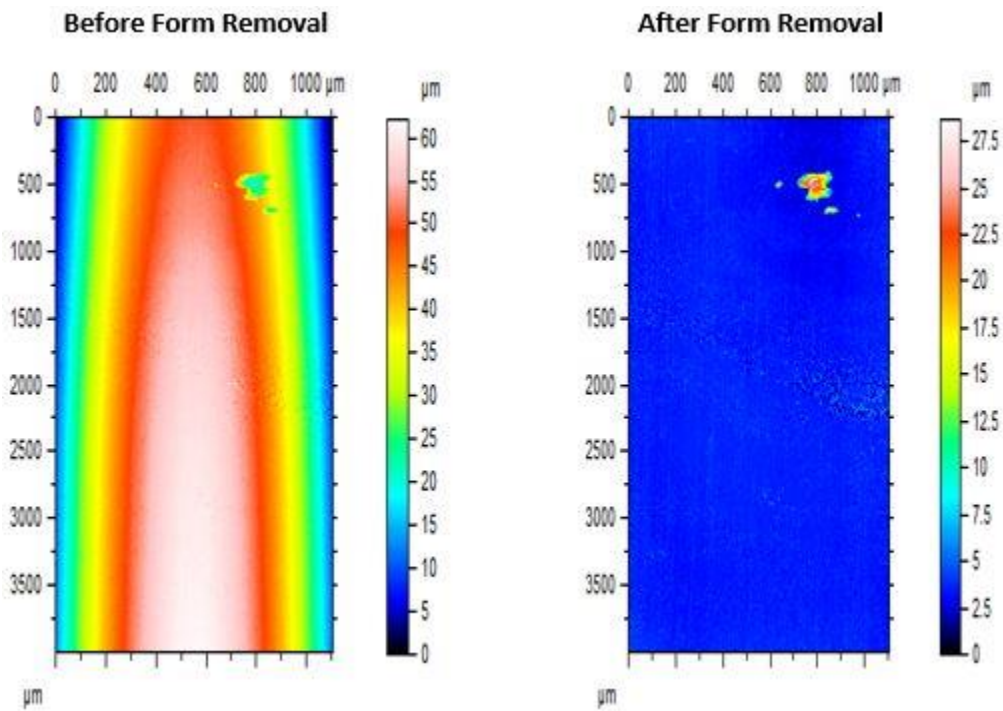


Figure 2.2.2.3.a

Example of the form-removal function for processing the WLI scans in MountainsMap. The pits are preserved while the bulk surface is averaged to resemble a flat surface.

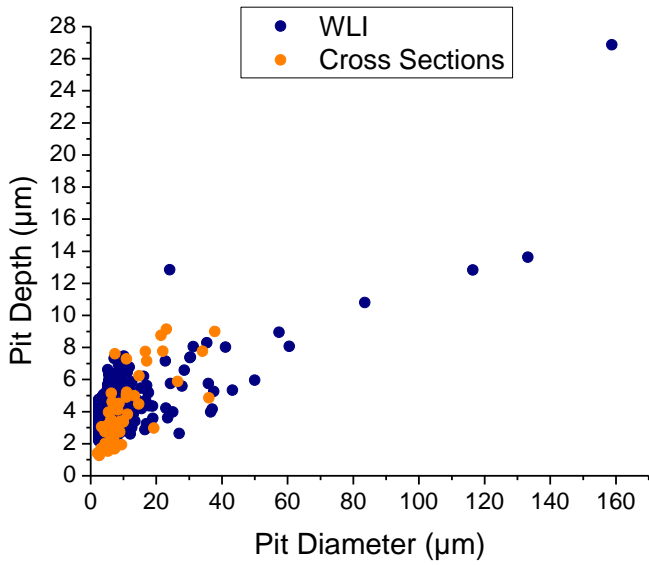


Figure 2.2.2.3.b

Empirical data of cross sections overlapped well with the WLI data, validating the WLI technique.

2.2.3 Mechanical Loading Conditions

The pristine, and low-/high-salt corroded samples were fatigue loaded at both low ($\Delta\sigma = 1055$ MPa) and high stress ($\Delta\sigma = 1165$ MPa) levels. All tests were run with a stress ratio ($R = \sigma_{\min} / \sigma_{\max}$) of 0.1. Cycling was performed under load control using a servo-hydraulic load frame controlled via MTS software. The maximum strain values are 0.847% and 0.936% for the low and high stress conditions, respectively. While these are rough estimates based on Hooke's Law at 704°C, they are useful in that they enable reasonable comparisons with strain controlled data reported in the literature for similar temperatures [64]. The complete testing matrix is shown in Table 2.2.3.a.

As previously mentioned, this study evaluated the fatigue behavior of the samples on multiple levels, specifically: fatigue crack initiation, crack propagation, and fatigue failure. To accomplish such analysis, a means to determine the fatigue crack initiation life and crack growth rates was needed. Prior efforts have demonstrated significant success in the use of programmed loading sequence to mark the surface, thus enable (1) clear identification of crack formation location, (2) calculations of the crack initiation life, and (3) quantitative characterization of the small crack growth kinetics [17,20,49,65–73]. Specifically, a variable fatigue loading sequence in which

applying a pattern of cycles that have differing stress ratios (R) had to be created for each low and high stress categories. This variable loading sequence made topographical markers on the fracture surface. Such markers are referred to as marker bands. They are a periodic collection of cycles in which R alternates between 0.1 and some other specified value, like 0.6, for a limited number of cycles each. These sets of cycles are repeated a specified number of times to ensure visibility of the marker band on the fracture surface under a microscope. After a marker band is complete, the fatigue loading returns back to the baseline loading conditions, $R = 0.1$, for another long set of cycles. After the baseline is complete, another marker band ensues. This sequence is applied throughout the fatigue test until the specimen fails. Such a loading sequence in its entirety is referred to as a marker band protocol.

Figures 2.2.3.a and 2.2.3.b illustrate the finalized marker band protocols for the low stress and high stress categories, respectively. During the course of this study, the protocols evolved for both the high and low stress conditions to maximize the visibility, clarity, and spacing of the marks on the fracture surface to aid in analysis. Specifically, the criteria used to develop the marker band protocols was that enough marker bands should appear on the fracture surface to enable the determination of the crack initiation life and to allow sufficient tracking of the fracture surface to determine crack growth rates for different crack sizes. However, there should not be too many marker bands, and they should not be too large; in such instances, the number of fatigue cycles for which $R \neq 0.1$ increases; thus, causing the fatigue data of cycle numbers to be less representative of the numbers they would be had all cycles been applied at $R = 0.1$. As such, each low and high marker band protocols were adjusted after each test after examination of the fracture surface to attain enough visible marker bands on the fracture surface of the next sample while keeping the number of cycles where $R \neq 0.1$ to less than 10% of the total life.

T = 704°C, R = 0.1, f = 0.3 Hz		
	Low Stress $\Delta\sigma = 1055$ Mpa $\sigma_{\max} = 1172$ MPa 0.847% total strain	High Stress $\Delta\sigma = 1165$ Mpa $\sigma_{\max} = 1294$ MPa 0.936% total strain
Pristine	1	1
Low Salt Concentration	2	2
High Salt Concentration	2	2

Table 2.2.3.a

Fatigue testing matrix. Samples were divided into corrosion categories (rows) and stress categories (columns).

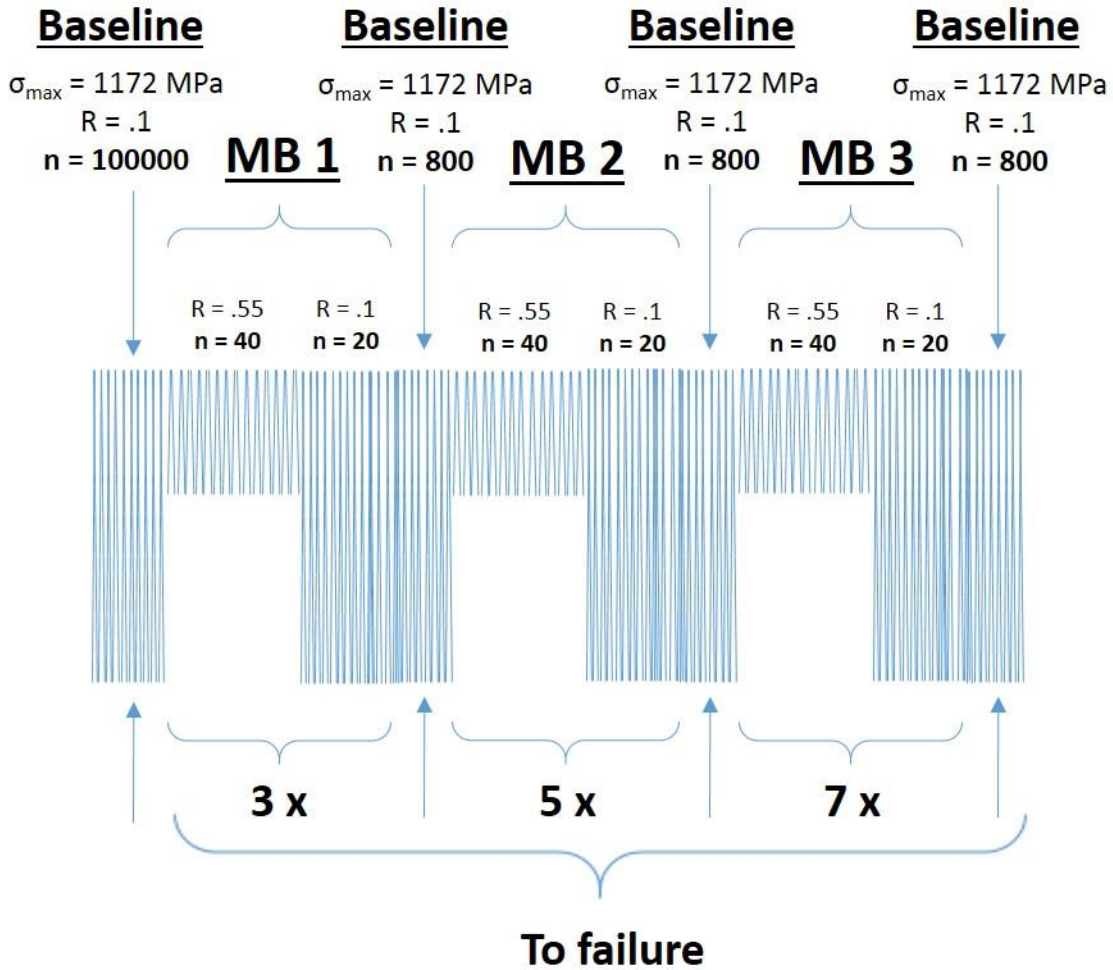


Figure 2.2.3.a

Finalized loading sequence (marker band protocol) for the low stress tests. First baseline sequence was large as cracking was confidently not expected to occur until after 10^5 cycles. All other subsets (n) were larger than those in the high stress protocol (Figure 2.2.3.b) due to the increased crack growth rates at high stress. Cycle counts for subsets in which $R > 0.1$ within MBs are larger due to the increased R decreasing the crack growth rate. If they were too small, the MBs would possibly not be detectable. Varying the number of markers for each MB (i.e. 3x, 5x, 7x) assists in identifying marker bands on the fracture surface.

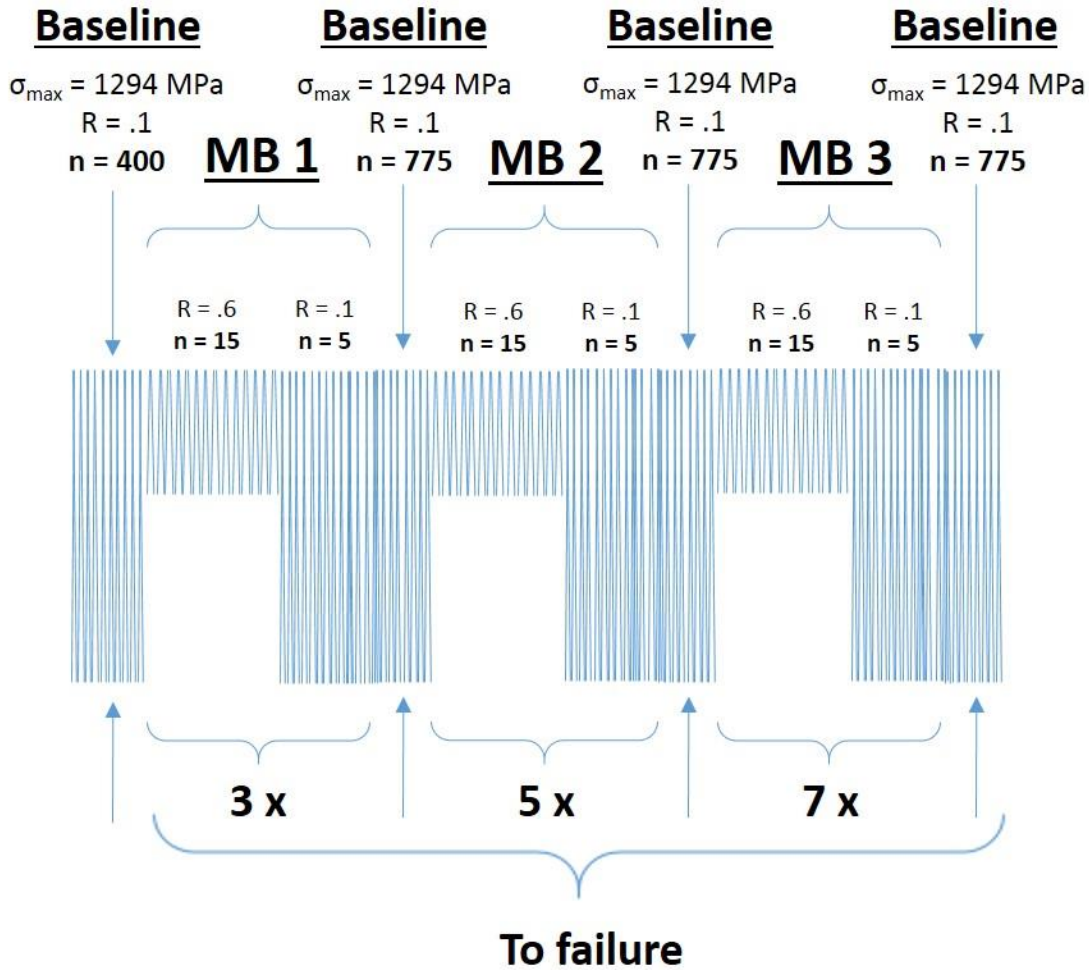


Figure 2.2.3.b

Finalized loading sequence (marker band protocol) for the high stress tests. First baseline was small in case cracking began very early after commencement. All other subsets (n) were smaller than those in the low stress protocol (Figure 2.2.3.a) due to the increased crack growth rates at high stress. Cycle counts for subsets in which $R > 0.1$ within MBs are larger due to the increased R decreasing the crack growth rate. If they were too small, the MBs would possibly not be detectable. Varying the number of markers for each MB (i.e. 3x, 5x, 7x) assists in identifying marker bands on the fracture surface.

2.2.3.1 Testing Equipment

Fatigue testing was performed using a mechanical test frame from MTS Systems Corporation (MTS). Multipurpose Testware (MPT) was the MTS software used for programming the marker band protocol (e.g. the protocols in Figures 2.2.3.a-b) for the fatigue tests. MPT also allowed for real-time monitoring of the load and displacement commands to the frame as well as monitoring

of actual values. Furthermore, data was collected during testing as specified through MPT which included time, cycles, load, and displacement.

The elevated temperature environment was provided by an MTS 653 Furnace from which a thermocouple was embedded. This thermocouple was connected to a control, Omega AH806AU, which measured the temperature every second and recorded the temperature on a programmed interval.

2.2.3.2 Procedure

To run a test, a certain procedure was followed to maintain consistency among the tests and to ensure safety and rigor in the testing method. To begin, the marker band protocol and data acquisition plan were programmed in the MPT software. All cycles were assigned a sinusoidal function of load vs. time with a frequency of 0.3 Hertz (cycles per second). The test hardware was prepared, beginning with fastening a 100-kN load cell into the crosshead of the mechanical test frame (Refer to Figure 2.2.3.2.a for test hardware arrangement). With a 6.34-mm minimum cross-sectional diameter through the gauge section of the sample and maximum stress levels of 1172 MPa and 1294 MPa for the low stress and high stress testing, respectively, the maximum applied forces that were input into the MPT test programs were:

Low stress:

$$\sigma_{max} = \frac{P_{max}}{A} \Rightarrow P_{max} = \sigma_{max}A = (1172 \text{ MPa}) \left[\frac{\pi}{4} (6.34 \text{ mm})^2 \right] = 37.0 \text{ kN}$$

High stress:

$$P_{max} = (1294 \text{ MPa}) \left[\frac{\pi}{4} (6.34 \text{ mm})^2 \right] = 40.9 \text{ kN}$$

Steel extension rods were attached to the load cell (at the top of the frame) and to the actuator (at the bottom of the frame). Each upper and lower arm consisted of a base (thick rod) and a clevis. Grips, which held the fatigue samples by threading on each end of the sample, were to be pinned in these clevises. Before proceeding to fasten the sample to the grips and pin the grips in the clevises, an MTS 653 Furnace was attached to the frame. This furnace was capable of achieving the desired testing temperature of 704°C. The furnace was able to fit around the sample without touching it.

The hydraulic pump for the actuator was activated after attaching the furnace to the frame. The pump enabled the actuator to move up and down during testing according to immediate feedback from the load cell (as these were stress-controlled tests rather than displacement-controlled). The frame was then put temporarily on manual displacement command for fastening of the sample, referencing the load cell to zero, and final positioning of the crossbar, furnace, and actuator. The clevises were then aligned perpendicularly to each other to prevent bias of the location(s) of fatigue cracking in the sample.

A 24-hour monitoring system was arranged. An Omega thermocouple with its HH806AU control/monitoring device was an essential piece of this system, ensuring an accurate and consistent temperature of 704° C at the center of the furnace where the sample was to be tested. The furnace had its own thermocouples; however, they were situated on the far sides of the furnace and were thus less accurate in measuring the temperature at the center of the furnace. An alarm was set on the thermocouple control piece if the temperature exceeded a specified range around 704°C during the test. This range did not exceed 700°C – 708°C for any given test. A camera was set up for remote audio and visual monitoring of the test. Audio and visual alerts were arranged on a remote monitoring device such that the experimenter could be alerted if the camera sensed excessive movement or noise.

The temperature was a critical parameter to monitor for this type of environmental testing because if the temperature went out of range, it could reflect any of several issues or events, including but not limited to: a leak in the furnace insulation, failure or inadequate positioning of a fixture (e.g. clevis, fan), a power-outage, and specimen failure. With the monitoring system, such an event could be promptly addressed. A time interval for recording temperature was set on the thermocouple control according to the expected duration of the fatigue test. Due to limited memory on the device, this interval would be as short as 30 seconds or as long as 2 minutes for high and low stress tests, respectively.

Two fans were positioned about the frame such that one blew ambient air onto the upper grip and the other blew ambient air onto the lower grip. This arrangement ensured that test fixtures did not become overheated. By cooling the grips, the temperature of the clevis pins was lowered as well as the clevises and bases. This simple cooling action helped ensure accurate readings from the load cell and accurate displacement movement by the actuator.

The manual command module for the test frame was then switched from displacement to force to allow the sample to slightly expand after increasing the temperature in the furnace. From this point forward, the test frame was in force control; however the command would still be manually controlled until starting the test. As the temperature stabilized around 704° Celsius, the force and displacement thresholds were finalized on MPT. If these thresholds were reached at any point in the test, including at the point of fatigue failure, the pump for the actuator would turn off. After the thresholds were adjusted, the test was ready to begin. The camera was turned on, the thermocouple was set to acquire temperature data, the manual command was deactivated on the MPT software, and the fatigue test was started. The test was left to run after it was assured to be running properly and safely. In addition to remote monitoring, the test would occasionally be checked on site throughout its duration. Tests lasted anywhere from several hours to about one month.

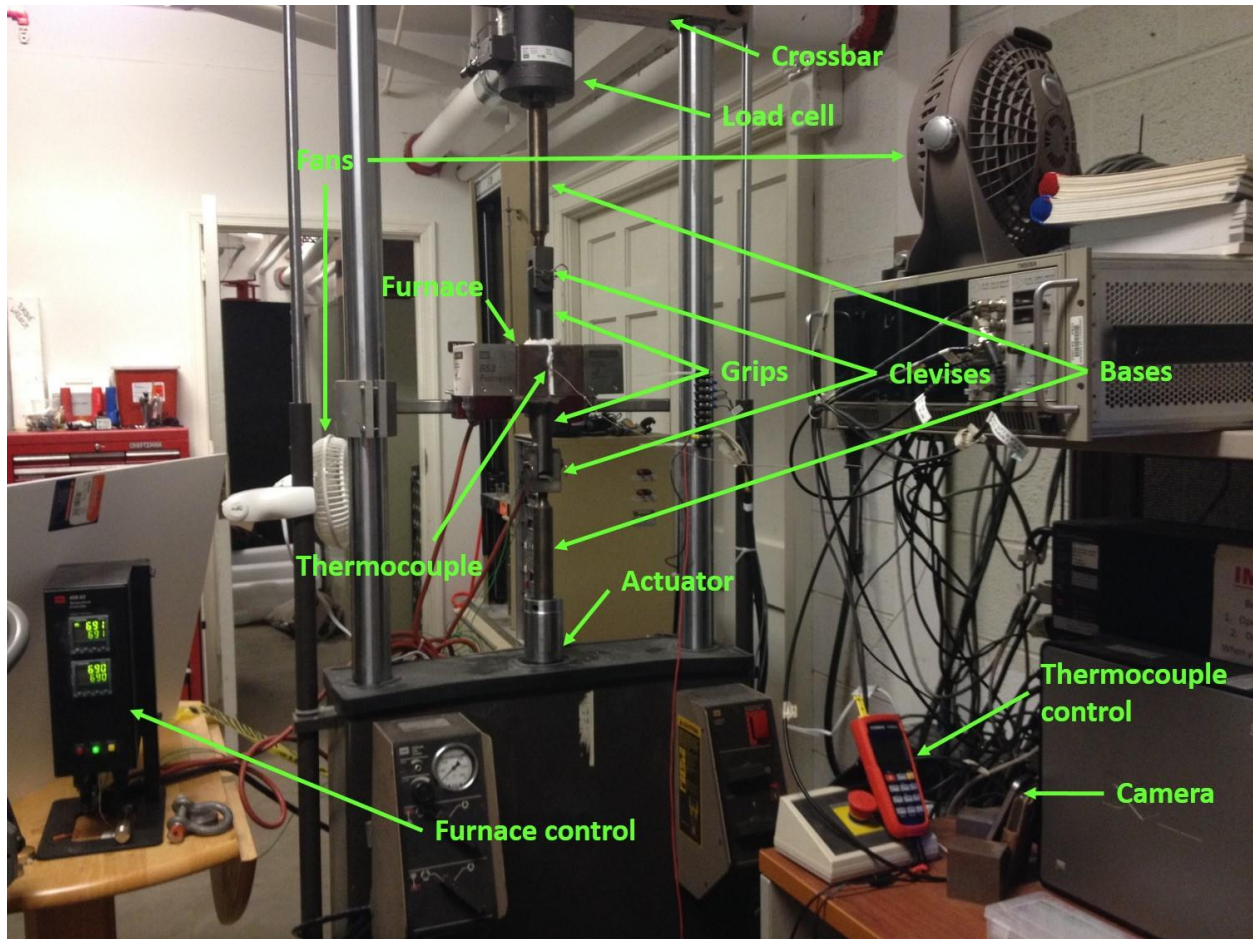


Figure 2.2.3.2.a

Test hardware arrangement. Furnace envelops sample; thermocouple inserted in furnace; sample attached to grips which are attached to perpendicularly-positioned clevises attached to long bases; top base attached to load cell, and load cell attached to adjustable crossbar; bottom base attached to actuator.

2.2.4 Fracture Analysis

Fracture analysis followed the fatigue tests. This analysis involved both the fracture surface and the corroded surface (surface of the gauge section). On the fracture surface, the fatigue crack initiation site was found, and the depth of the crack initiating pit was measured. Any marker bands were located on the crack surface to assess the crack initiation life and crack propagation behavior. The same crack initiation site was then located on the corroded surface to transfer this location to the WLI scans taken prior to loading. This enabled analysis of the regional metrics of the crack initiation site along with the diameter of the crack initiating pit.

2.2.4.1 *Crack Initiation Site*

After each sample failed, fracture analysis was performed using a Quanta 650 scanning electron microscope (SEM) by FEI. The fracture of the bottom piece of the sample would typically be chosen for ease of connecting fiducial features with the WLI scans. Prior to analysis, the specimen would be cleaned by sonication for at least ten minutes in acetone followed by at least ten minutes in methanol. SEM images were taken of the fracture surface at low magnification to give an overview. This overview helped to determine the number of cracks present on the fracture surface and the feature that nucleated fatigue cracking. For example, two fatigue cracks were present on the fracture surface of Sample M3-114 (HSC, high stress) shown in Figure 2.2.4.a. In all cases, crack initiation occurred at a corrosion feature on the surface, with the exception of Sample M3-166 (LSC, low stress) whose crack initiation site was roughly 250 μm inside the outer surface where brittle fracture initiated at a microstructural inhomogeneity.

Images were then taken of the primary fatigue crack (defined as the crack that lead to final failure) at higher magnification, usually between 50x and 75x (e.g. Figure 2.2.4.b). Marker bands that appeared later during crack propagation were typically visible at this magnification because they were thicker due to increasing crack growth rates. Images at higher magnification were taken (between 500x and 2500x), and later stitched together if necessary, to find marker bands that appeared at or soon after crack initiation because they were more difficult to identify due to their small size. All marker bands were then traced on the crack (Figure 2.2.4.c) for later analysis of crack initiation life and crack propagation.

2.2.4.2 *Crack Initiation Region*

The crack initiation sites on each sample were then located on the outer sample surface (on the gauge section). Other pits and features in the vicinity of the crack initiating pit were used as fiducial points to find corresponding features in the WLI scans. This approach has been previously applied to determine the local region in which the initiation site was located [49]. Figures 2.2.4.d-e help illustrate this approach. Knowing the crack initiating region enables the comparison of the metrics of that region to the rest of the regions on the sample (that did not form cracks) with respect to the corrosion metrics of average regional pit size, regional pitting density, and regional pit spacing.

2.2.4.3 Crack Initiation Life

The marker bands observed on the fracture surface can be used to determine the crack initiation life [49]. The first visible marker band was consistently found 25-50 μm away from the crack initiation site (which was at some point on a pit) in a direction perpendicular to the marker band as illustrated in Figure 2.2.4.f (in reference to Figure 2.2.4.c). As such, the crack initiation life for this study was the number of fatigue cycles it took for a crack to grow to the size of 25-50 μm . To determine this number of cycles, the marker band lying within the 25-50 μm range was identified in the marker band protocol. Cycles of large R ($R > 0.1$) were excluded from this initiation life.

While the marker band technique can be optimized to produce detectable marker bands by the time a crack size reaches 5 μm , such high fidelity characterization is time-consuming and requires an iterative protocol development that could not be performed due to the limited specimen count in the current study [74]. Regardless, the current marker loading sequence was able to produce clearly evident marker bands in the range of 25-50 μm crack sizes. As such, the calculated fatigue crack initiation life was functionally defined in this study as the life to the point of a marker band that fell within this range.

2.2.4.4 Crack Growth

After determining the fatigue crack initiation life, it could then be compared to the crack propagation life to show the contribution of each to the total fatigue life to failure through the following relation:

$$N_f = N_i + N_p \Rightarrow \frac{N_i}{N_f} + \frac{N_p}{N_f} = 1$$

This information would reveal which stage is more of a concern in the big picture of the total life of the material, given the loading and environmental conditions.

It was established that each marker band in the marker band protocol between the points of crack initiation and the end of the fatigue crack could be found on the fracture surface. These marker bands enabled the tracking of the crack progression between the events of crack initiation and material rupture. The crack growth rate could therefore be estimated at different crack sizes.

The crack growth rate was determined at each midpoint between marker bands along a vector perpendicular to each marker band. As the number of cycles between marker bands was known,

and the crack lengths were known between the end of the first of two consecutive marker bands and the start of the second marker band, the crack growth rate, da/dN , was estimated for the midpoint as such:

$$a = \frac{a_{1,end} + a_{2,start}}{2}$$

$$\frac{da}{dn} = \frac{a_{2,start} - a_{1,end}}{\# \text{ baseline cycles}}$$

With this data, crack growth rate vs. crack length, a , was plotted as well as crack length vs. number of cycles of crack propagation—the number of cycles from crack initiation, starting at the crack length of 25-50 μm . These plots showed the fatigue crack propagation behavior according to load and salt concentration.

Crack growth rates vs. crack length could not reasonably be plotted over the entire propagation life (all the way from crack initiation to failure). Specifically, data could not be plotted both early and late in the crack propagation life. Therefore, the plot of crack length vs. the number of cycles of crack propagation was necessary to produce as it illustrated the fatigue crack propagation in a manner that enables an accurate crack propagation behavior from crack initiation all the way to failure. It also exhibited another facet of the crack propagation behavior, demarcating the size of the crack at specific points in crack propagation life, for further insight in the analysis of crack growth patterns among the categories of salt concentration and stress level.

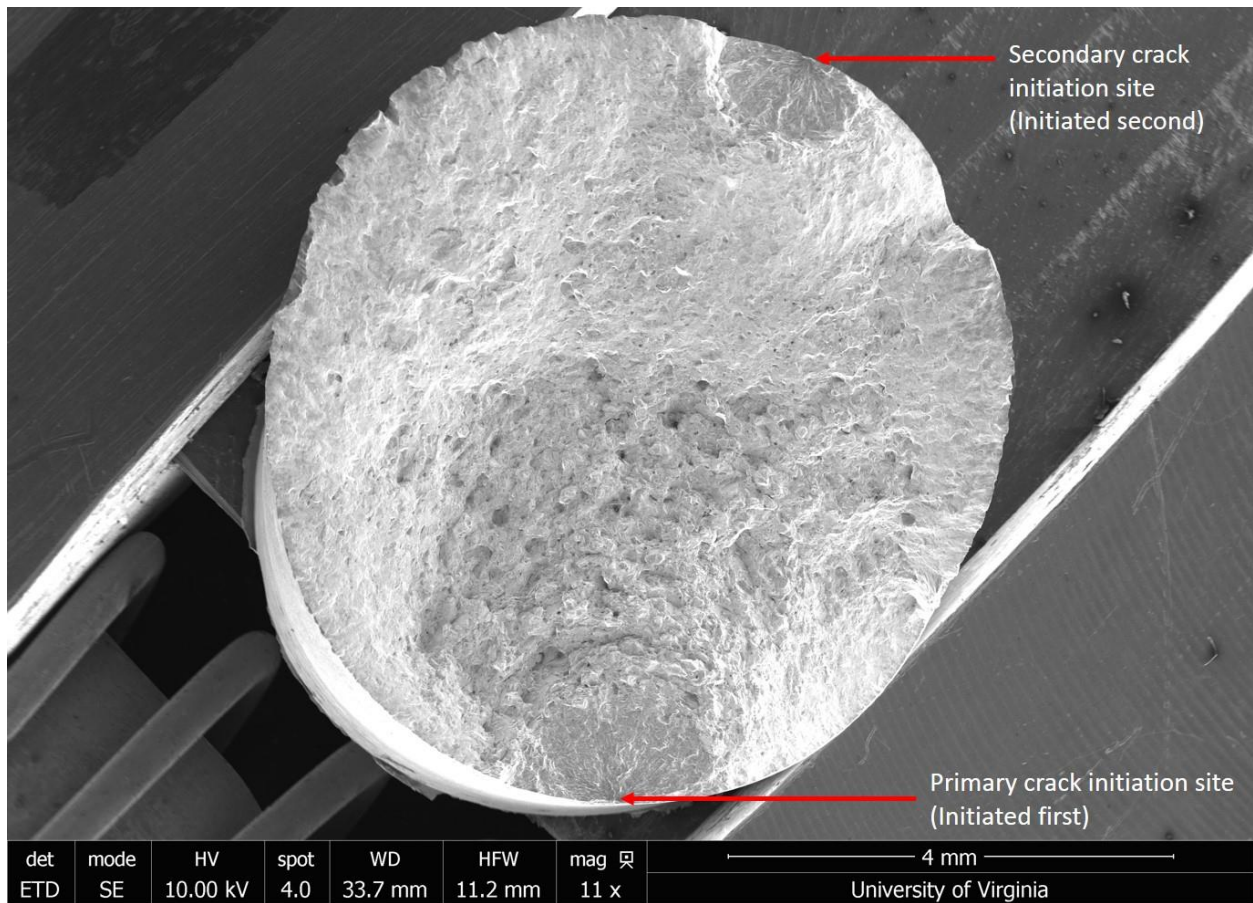


Figure 2.2.4.a

A fracture surface with two fatigue cracks. The primary crack is the crack that ultimately lead to failure and initiated before the secondary crack. Note the primary crack's larger size.

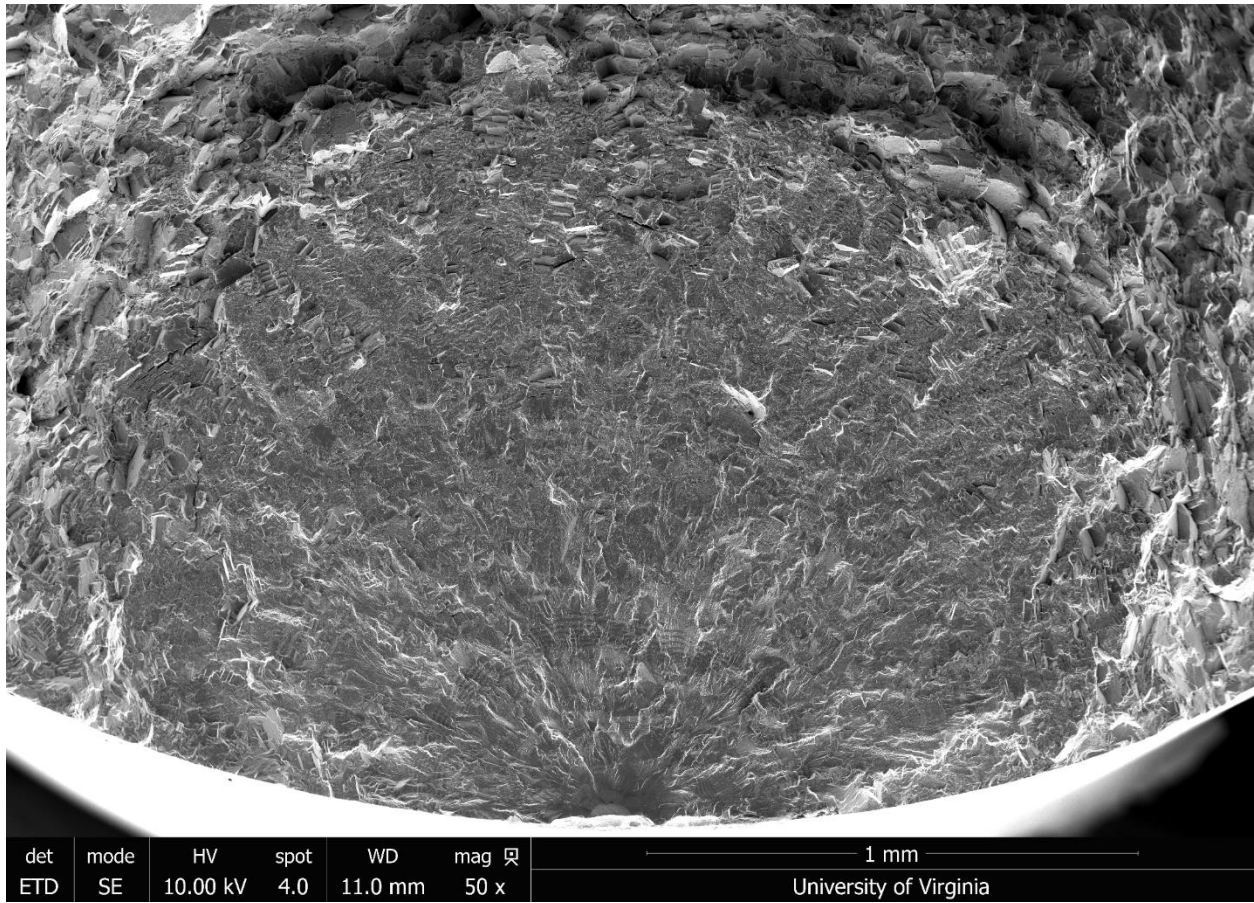


Figure 2.2.4.b

SEM image of a primary fatigue crack (Sample 155: HSC, Low stress).

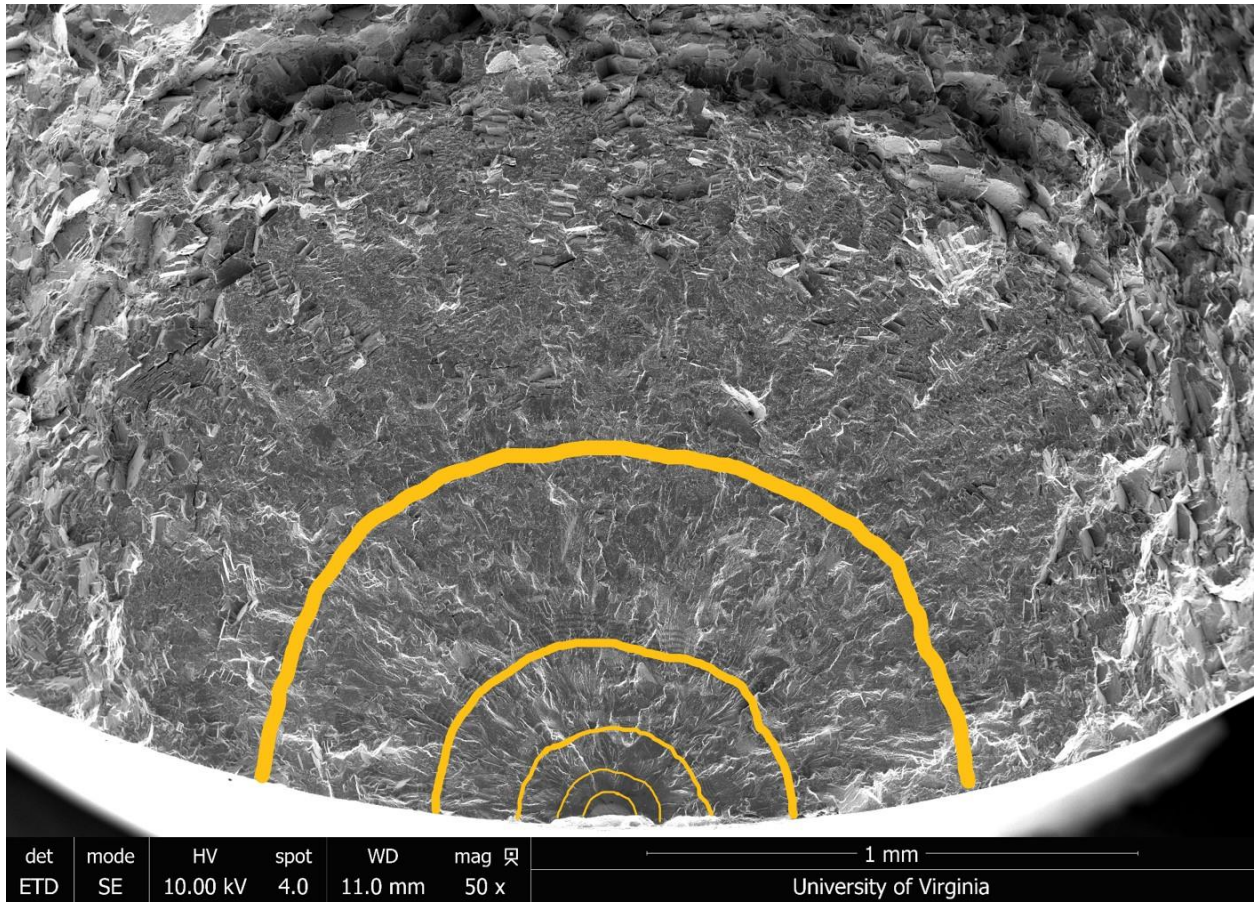


Figure 2.2.4.c

The fatigue crack from Figure 2.2.4.b with marker bands traced in orange for tracking the crack front and determining fatigue crack initiation life and crack propagation life.

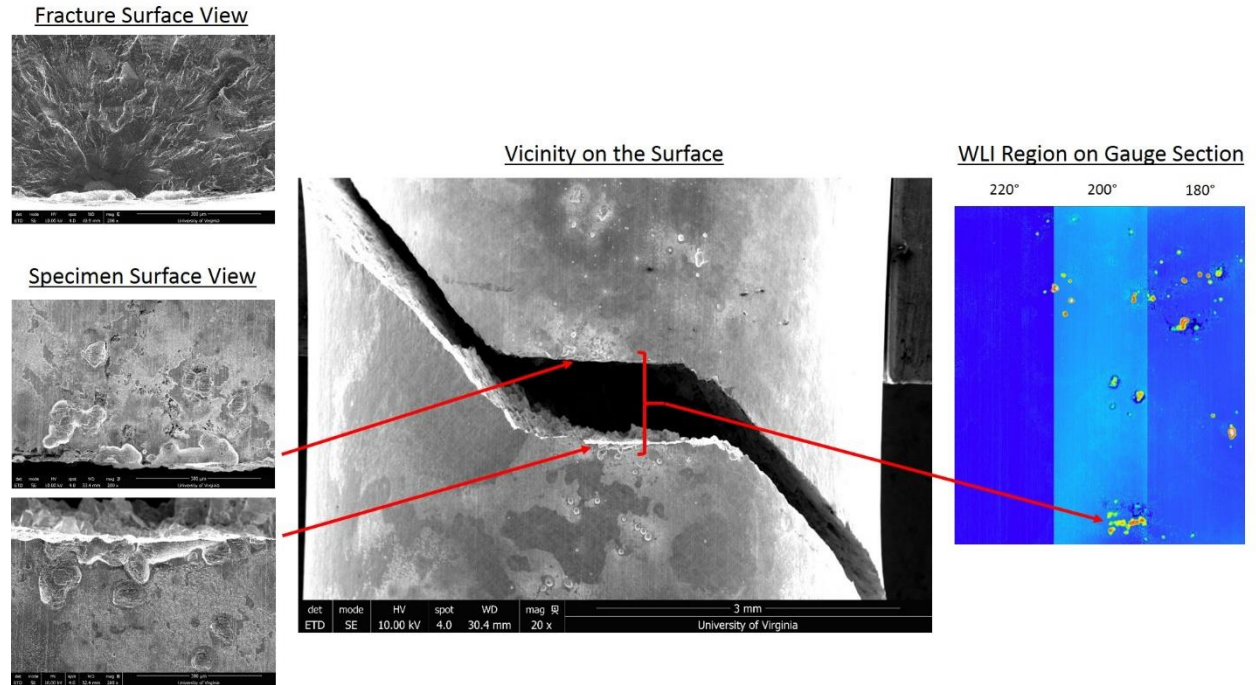


Figure 2.2.4.d

The region where the crack initiation site was located involved (1) noting the shape of the crack-initiating pit, (2) noting the vicinity of the initiating pit, and (3) matching the crack-initiating pit shape and vicinity to the WLI scans.

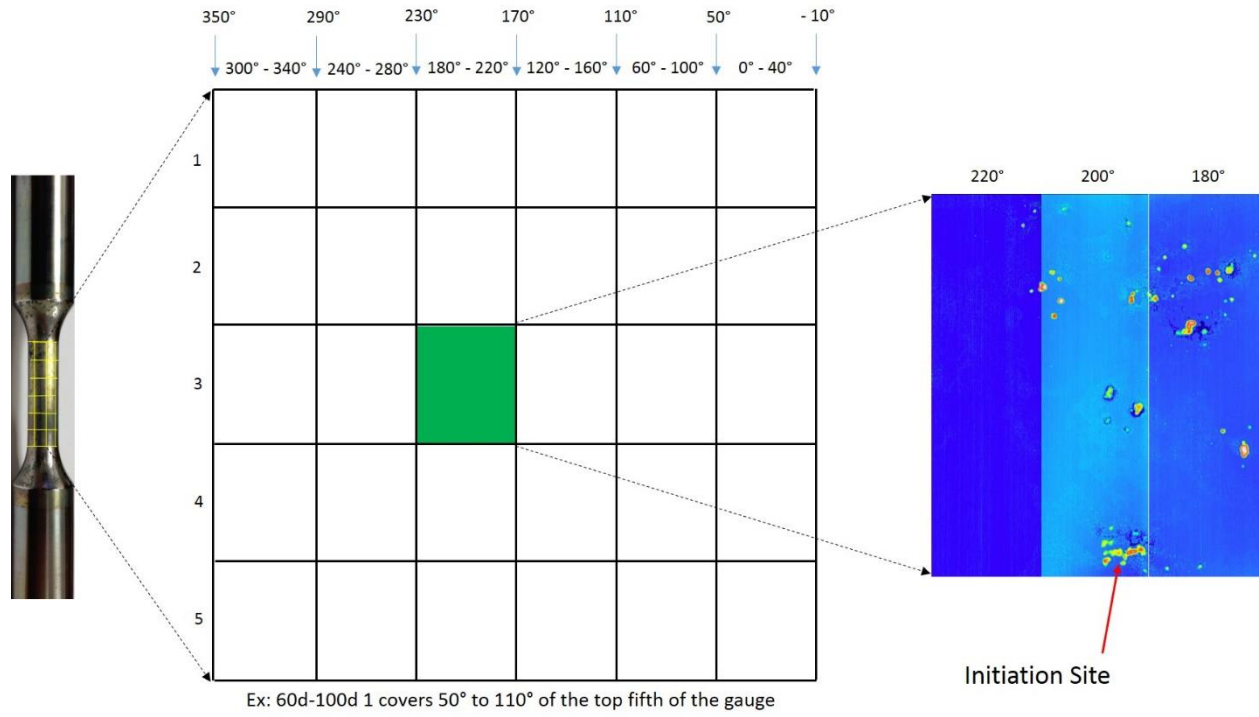


Figure 2.2.4.e

The specific region on the 30-region grid of the gauge section was noted after finding the crack-initiating pit on the WLI scans.

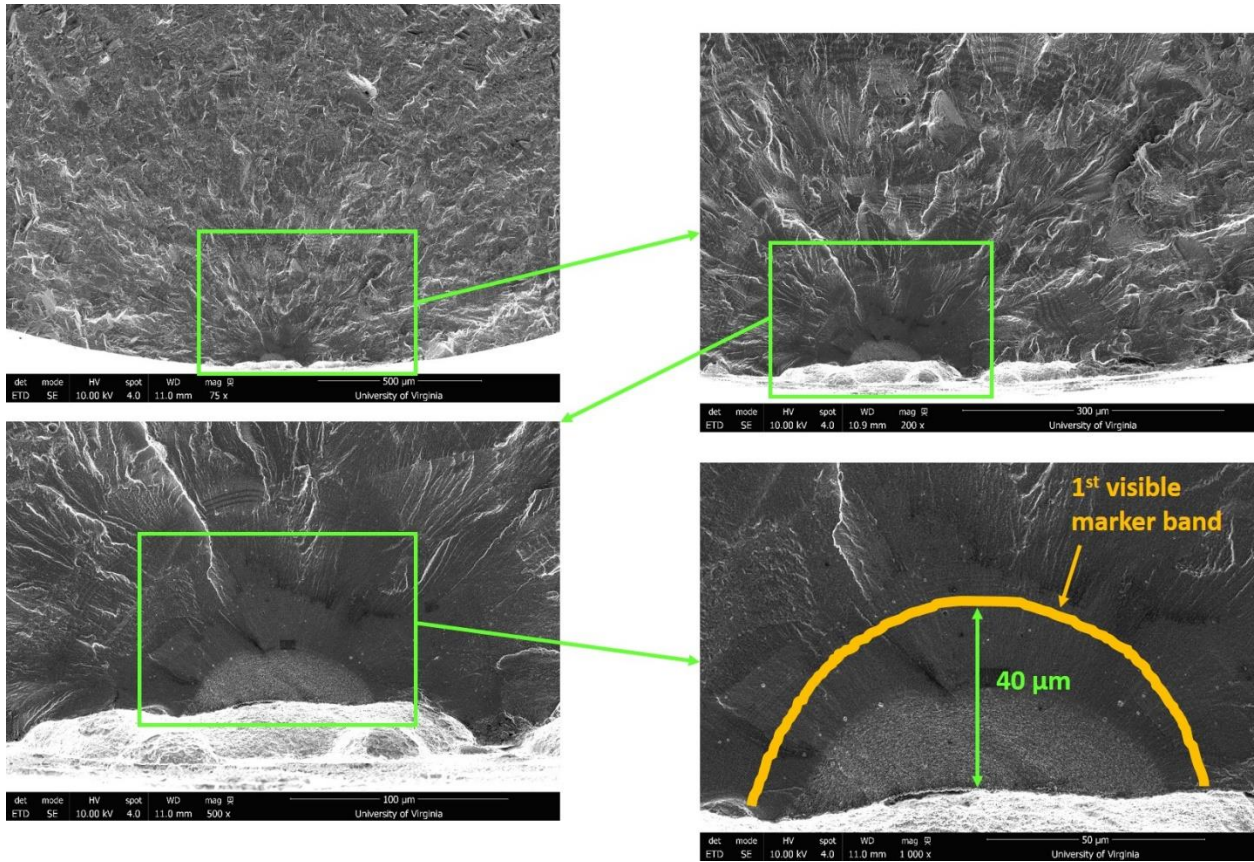


Figure 2.2.4.f

Zooming in on the same crack as displayed in Figures 2.2.4.b-c to find the first visible marker band, marking the crack initiation life at a crack length of between 25-50 μm.

3 Results and Discussion

This section aims to present the experimental results and data analysis for each of the four primary tasks of the study. The tasks were: (I) corrosion characterization, (II) assessing the impact of salt concentration on the S-N behavior, (III) analyzing the crack initiating pits, and (IV) assessing the impact of crack initiation and crack propagation on the overall fatigue behavior.

The task of corrosion characterization (Task I) provided data of the corrosion damage for the high and low salt concentration levels. This task was essential for describing the corrosion damage in terms of specific pitting metrics in connection with each level of salt concentration. Task II assessed the impact of salt concentration on the S-N behavior provided insight as to how much the salt concentration affected the S-N curve of ME3 at 704°C. Analysis of the crack initiating pits (Task III) first provided an in-depth evaluation of the crack initiating pit size with respect to the entire sample. Secondly, it assessed the importance of the regional pitting metrics where the crack initiating pit was located. Critically, these regional metrics where the crack initiation site was located were able to be compared to the metrics of all other regions of the sample to determine how much each of the metrics matter on a regional scale. Task IV first analyzed the relative dominance of the crack initiation life vs. the crack propagation life over the total fatigue life of each sample. These results were broken down by salt concentration and stress level to determine the influence of each of these categories on the dominance of the two general components of fatigue behavior. Further analysis in this task included a more detailed analysis of the environmental impact on crack initiation as well as a more in-depth look at crack propagation behavior.

3.1 Task I: Corrosion Characterization

The first task was aimed at characterizing the 3D distribution of corrosion damage that results from the high and low salt concentration exposures. The WLI methodology that was described and validated above is the basis for this analysis. The focus of this characterization was to establish descriptors of the bulk corrosion damage distribution that are hypothesized to be relevant to the fatigue initiation process; specifically this work will characterize the pitting density, average pit diameter, and average pit depth.

Pitting density was obtained for each sample by dividing its pit count by the area of the gauge section. This data is displayed in Figure 3.1.a. The pit densities are quite similar (with the

exception of M3-134), given the large disparity in salt concentration with which the samples were corroded. Given this similarity, however, the samples corroded with high salt concentration generally had smaller pitting densities (again, with the exception of M3-134, which was scanned twice, resulting in similar numbers each time).

Pit diameter and pit depth were the pit size metrics for this study. Pit diameter denoted the diameter of the pit as it would be as a perfect circle based on its area with respect to the plane of the bulk surface. Pit depth denoted the deepest point in the pit with respect to the plane of the bulk surface. Histograms of pit diameter and pit depth were constructed and are displayed in Figures 3.1.b and 3.1.c respectively. In these histograms, the size distributions between the categories of salt concentration were again somewhat similar; but as with pit density, there was a subtle difference in the pit size distributions. Samples corroded with low salt concentration (LSC samples) tended to have more pits on the smaller end of the distribution, whereas samples corroded with high salt concentration (HSC samples) tended to have more pits on the larger end of the distribution.

It was speculated that, under high salt concentration, clusters of small pits coalesced during the corrosion process. As such, the general trend should be that, though high salt concentration might result in lower pitting density than low salt concentration, the pit sizes should generally be larger with high salt concentration than with low concentration. This same trend was observed by Jilani et al. [75] where smaller pit depths correlated with higher pit density. This trend makes sense in light of the findings of Huang et al. [40] who showed that pitting density plateaus, given enough corrosion time. And it was previously mentioned that with increased corrosion time, pit sizes increase [36]. This general size difference was noted when computing the average pit size metrics, shown in Figure 3.1.d. All of the HSC samples had a larger average pit depth, and two of them had a significantly larger pit diameter than all other corroded samples.

The variability of these mean metrics still should not be underestimated as they do not necessarily reflect the large difference in the salt concentration with which the samples were corroded. A large difference in salt concentration translated into mere subtle differences in mean pitting metrics which even included overlap between the two categories of salt concentration. This is not particularly surprising considering the very high number of small pits. However, a more pertinent metric to the fatigue crack initiation behavior is the upper tail of the size distribution of the pits. Figures 3.1.e-f demonstrate that HSC samples generally had more pits of large sizes than LSC,

particularly for pits whose diameters were greater than 50 μm and whose depths were greater than 15 μm . This difference between LSC and HSC in the upper tail of the pit size distributions reflects that the generally larger average pit sizes of HSC over LSC samples (Figure 3.1.d) is primarily due to HSC having a greater number of large pits.

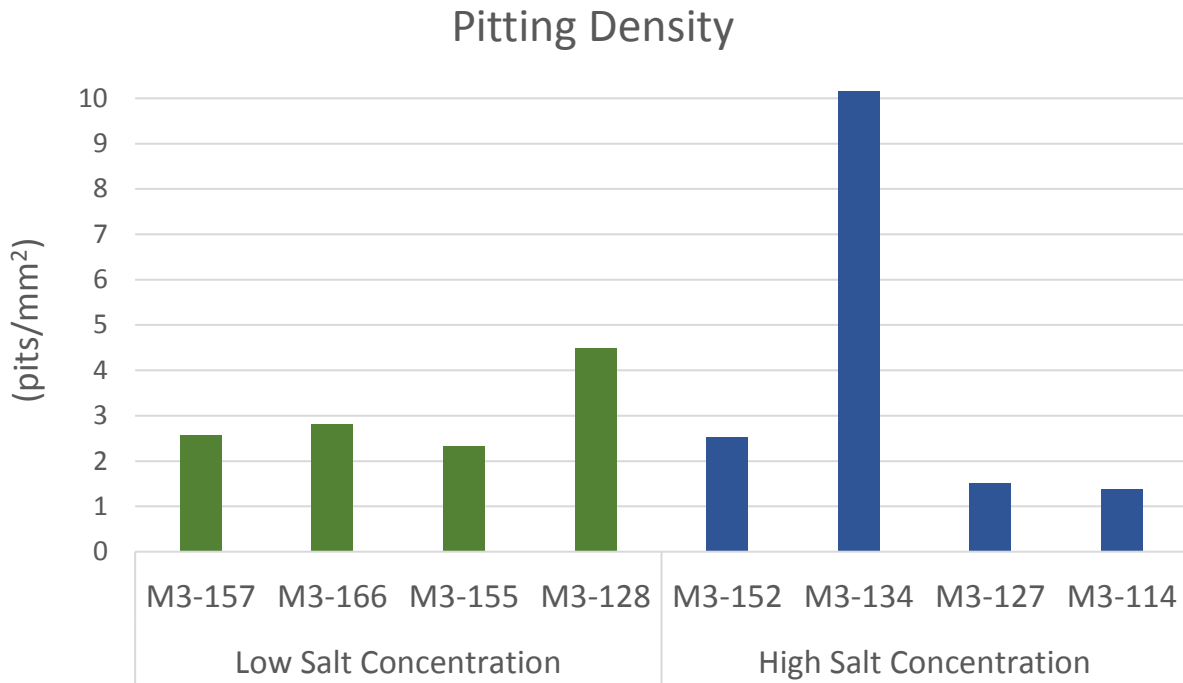


Figure 3.1.a

Pitting densities of the corroded samples. With the exception of M3-134, HSC generally had lower pitting densities.

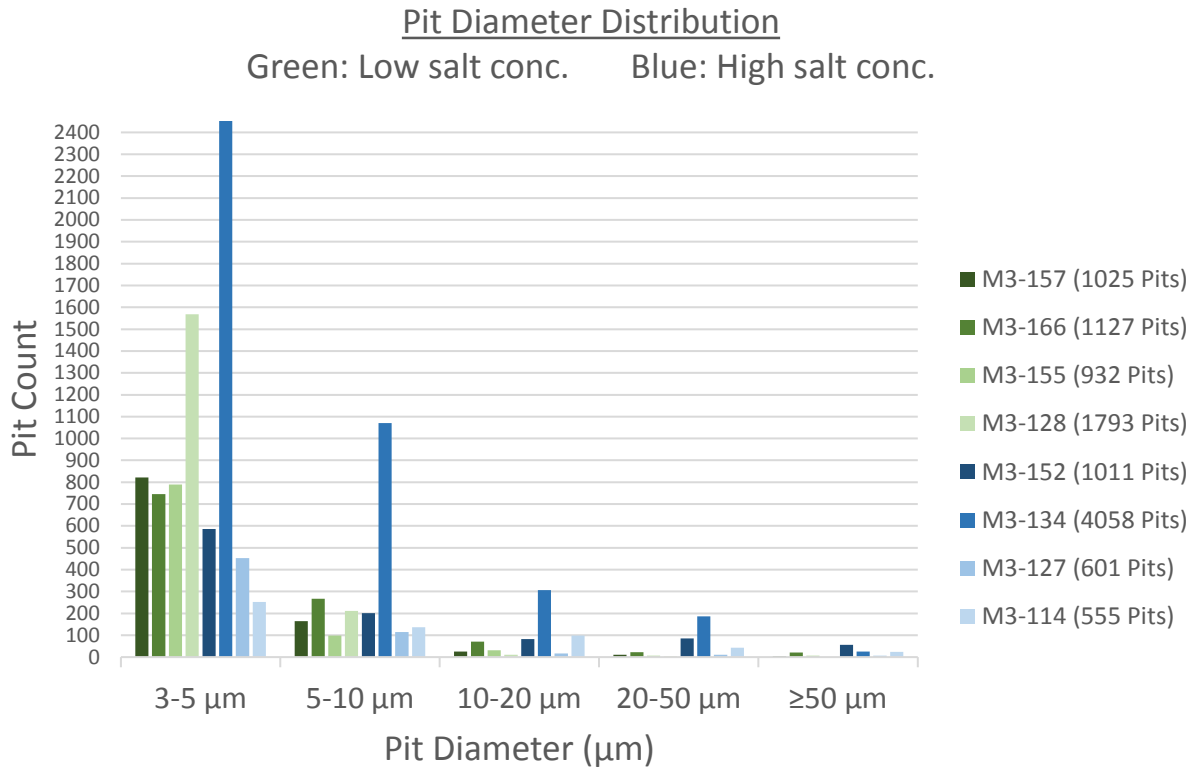


Figure 3.1.b

Distribution of pit diameter for all corroded samples. The distribution is positively skewed with many small pits and few large pits. LSC tended to have less wide pits whereas HSC tended to have more wide pits.

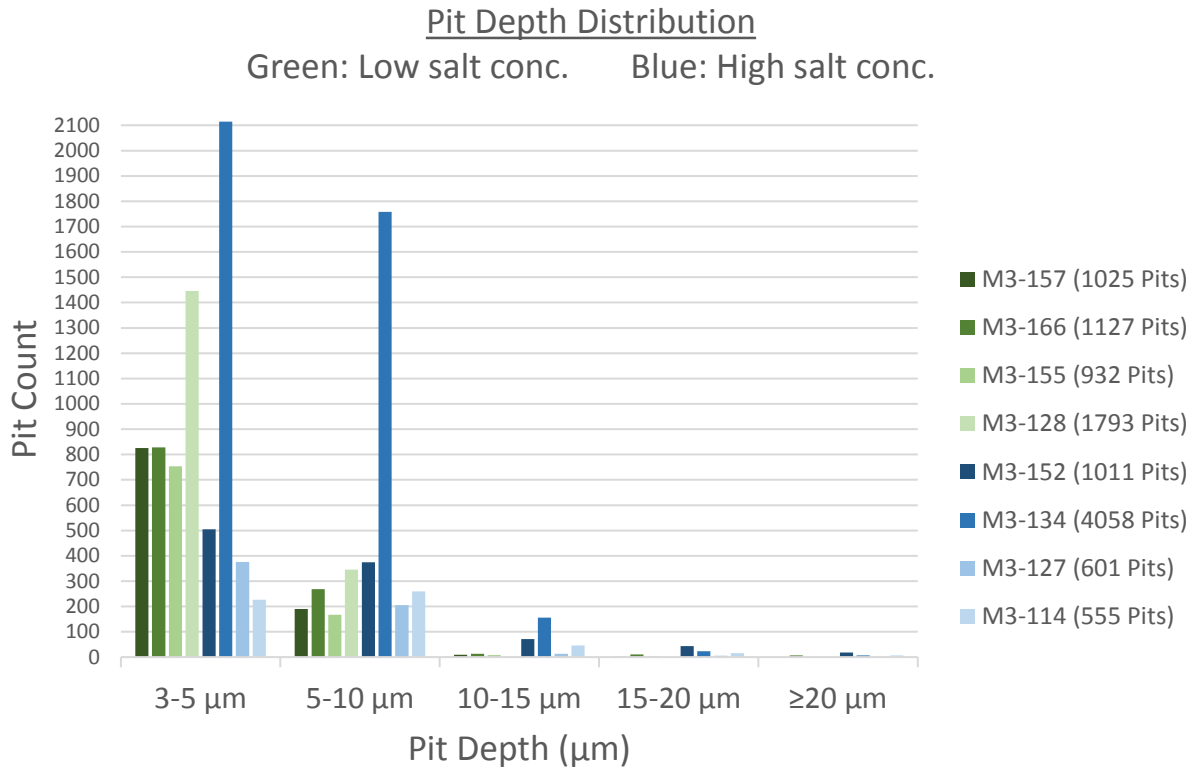


Figure 3.1.c

Distribution of pit diameter for all corroded samples. The distribution is positively skewed with many small pits and few large pits. LSC tended to have more shallow pits whereas HSC tended to have more deep pits.

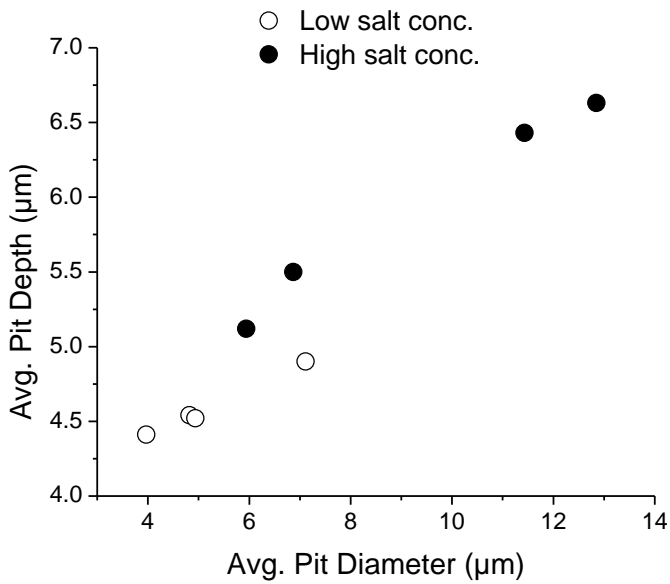


Figure 3.1.d

Average pit size metrics: average pit depth vs. average pit diameter. Given the variability, HSC samples generally had larger average pit sizes.

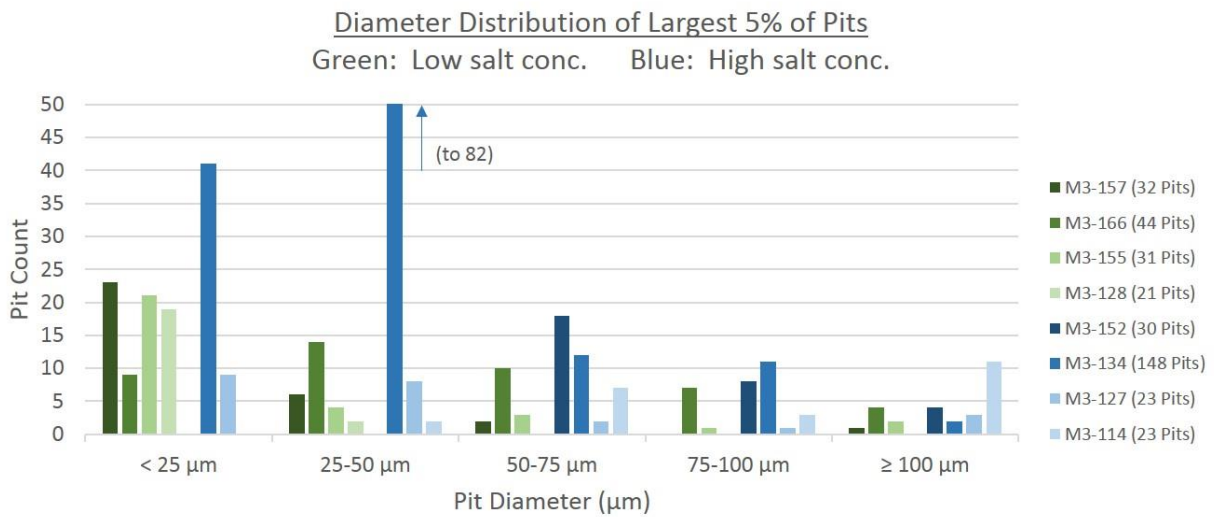


Figure 3.1.e

Distribution of pit diameter for the largest 5% of pits on each corroded sample. This histogram illustrates how HSC generally had more pits of large diameters than LSC.

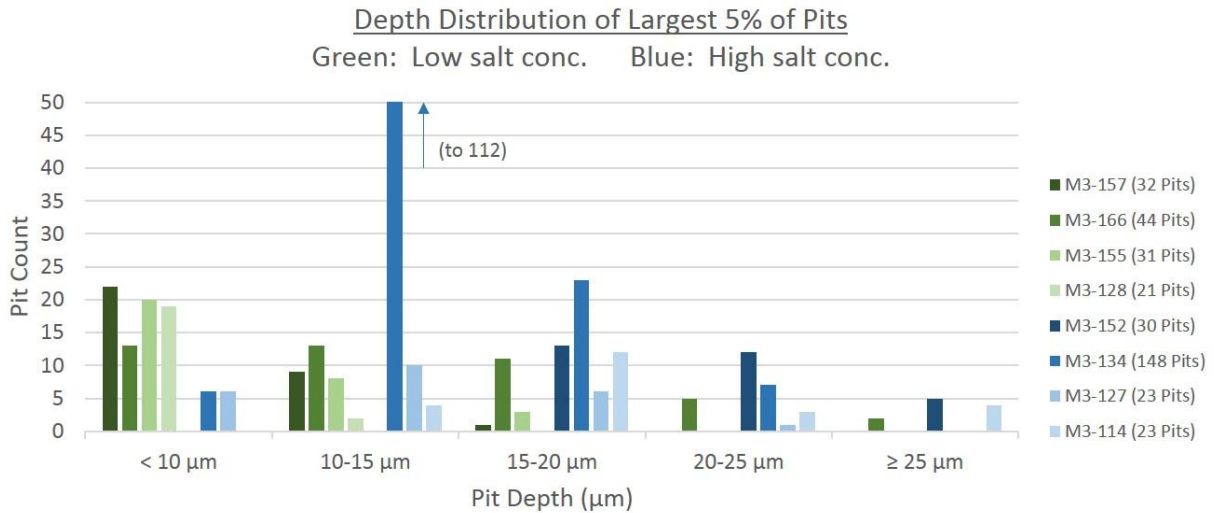


Figure 3.1.f

Distribution of pit depth for the largest 5% of pits on each corroded sample. This histogram illustrates how HSC generally had more pits of large depths than LSC.

3.2 Task II: Impact of Stress and Corrosion Level on Fatigue Behavior

This analysis first presents the fatigue results in the format of an S-N curve. The stress levels are embedded in this curve; as such, the primary variable of interest is salt concentration and how it impacts the 704°C S-N curve. Further investigation analyzes this impact in regards to bulk corrosion metrics. Bulk metrics of pitting density, average pit diameter, and average pit depth were analyzed in light of the fatigue test results in an effort to explain the S-N curve with respect to pitting metrics.

3.2.1 Fatigue Life Results

The effect of salt concentration on the S-N curve at 704°C is shown in Figure 3.2.a. This plot illustrates the stress range of fatigue testing for each sample against the number of cycles the samples lasted until failure. The pristine samples, though there were only two of them, attempt to represent the baseline S-N trend at 704°C with no corrosion. The stress ranges of 1055 MPa and 1165 MPa on the S-N curve were ultimately the designated low and high stress ranges, respectively. (Of note, M3-134 was initially tested at a stress range of 945 MPa. It was the first sample that was tested after the high-stress tests (of 1165 MPa stress range) were completed. Due to the unexpected duration of the M3-134 test, the stress range for this test, and for the remaining

tests, was increased to 1055 MPa after M3-134 ran for 825,000 cycles at the stress range of 945 MPa. Since the M3-134 was tested at two stress levels, its data was omitted from the S-N curve.)

One of the low-salt-concentration (LSC) samples at the high stress range of 1165 MPa nearly outlasted the pristine sample at that stress level. Both LSC samples at the low stress range of 1055 outlasted the pristine sample at that stress level. This observation was unexpected; however, as stress decreases, the range of fatigue life increases [76], and this study shows no exception for that. LSC samples typically outlasted the high-salt-concentration (HSC) samples, though not in all cases. Similarly, pristine samples typically outlasted the LSC samples. Nonetheless, HSC samples did tend to have the shortest fatigue lives while LSC samples tended to exhibit shorter fatigue lives than pristine samples.

3.2.2 Bulk Metrics

Further analysis of the impact of salt concentration on the S-N curve seeks to understand what is behind the impact of LSC and HSC samples on the S-N curve. It was previously shown that higher salt concentration does not necessarily correlate with higher pitting density. Though salt concentration was very different between the two categories, there was only a slight difference in pitting density in that low salt concentration generally resulted in higher pitting density than high salt concentration. This weak inverse correlation between salt concentration and pitting density is reflected by the test results in Figure 3.2.b. Each data point is identified by its category of salt concentration and stress level. Though HSC samples generally had lower pitting density (due to coalescence of small pits into larger pits), which corresponded to shorter fatigue lives, there was large variability in this relationship.

As for the average pit diameter and average pit depth for each sample, Figures 3.2.c-d also showed no outstanding effect on the fatigue tests as fatigue life varied among these two metrics. However, subtle effects between LSC and HSC become more apparent when isolating the stress levels. HSC generally had shorter fatigue life for a given stress level as these samples generally had a larger average pit size even though there was still some overlap in pit diameter and overlap in fatigue life at high stress.

These findings can be put in the context of two sets of similar components exposed to significantly different salt concentrations. It was shown that the salt concentration has only a weak correlation with the resulting fatigue life. Unfortunately, this lack of clear correlation between these average

pitting metrics and the fatigue life does not reveal which pitting metric(s), if any, pose a distinct threat to the fatigue behavior of the two sets of components. Therefore, it is necessary to investigate the effects of corrosion damage on fatigue behavior in more detail by analyzing the corrosion damage local to the crack initiation site in the context of the overall distribution of damage.

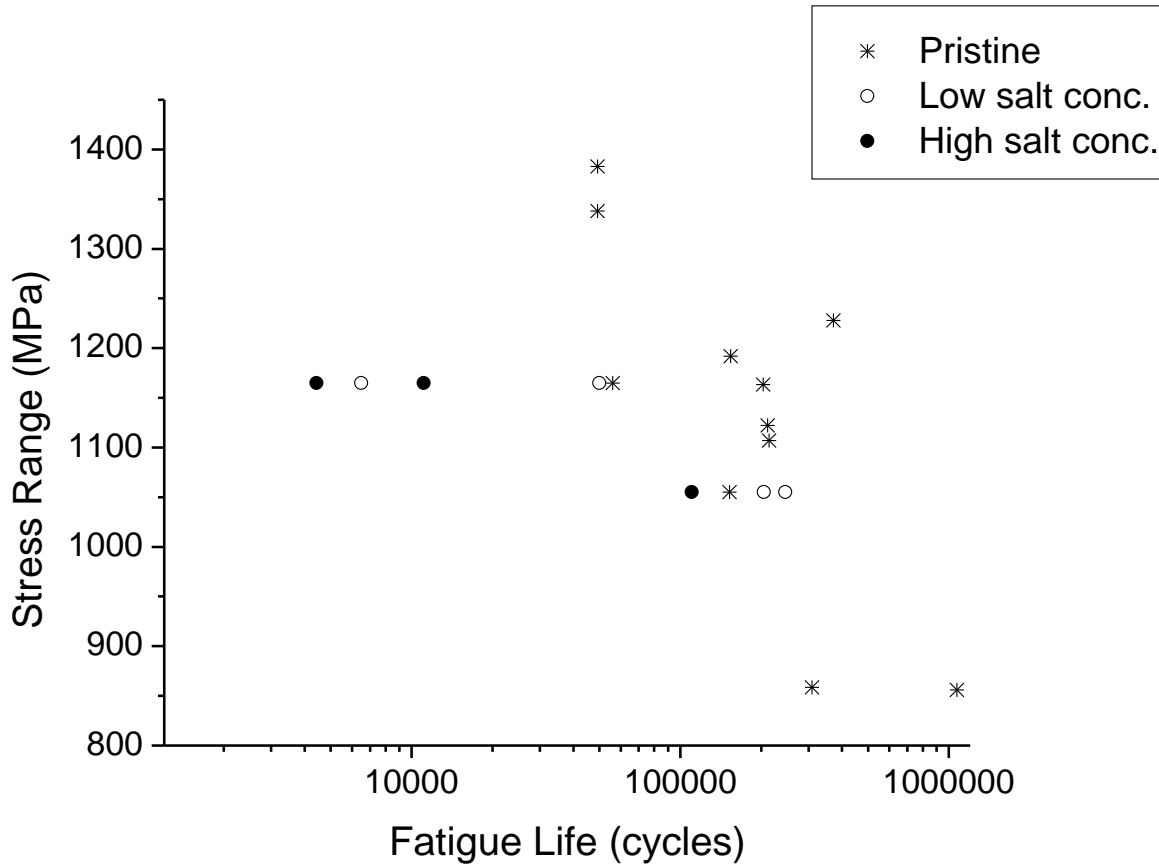


Figure 3.2.a

Resultant S-N curve of the fatigue testing matrix at 704°C on a log scale (with additional pristine data from collaborators). LSC did not show a distinguishable difference from pristine behavior at low stress but did have shorter fatigue lives than all pristine samples at high stress. HSC had shorter fatigue lives than all pristine samples and all but one LSC sample. Similar to LSC, the impact of HSC is more distinguishable at high stress.

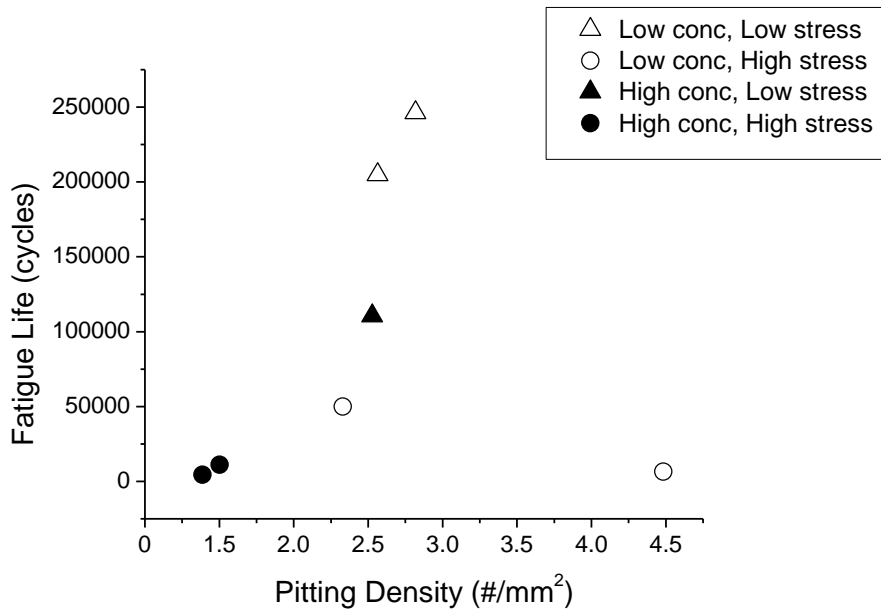


Figure 3.2.b
Influence of pitting density on fatigue life.

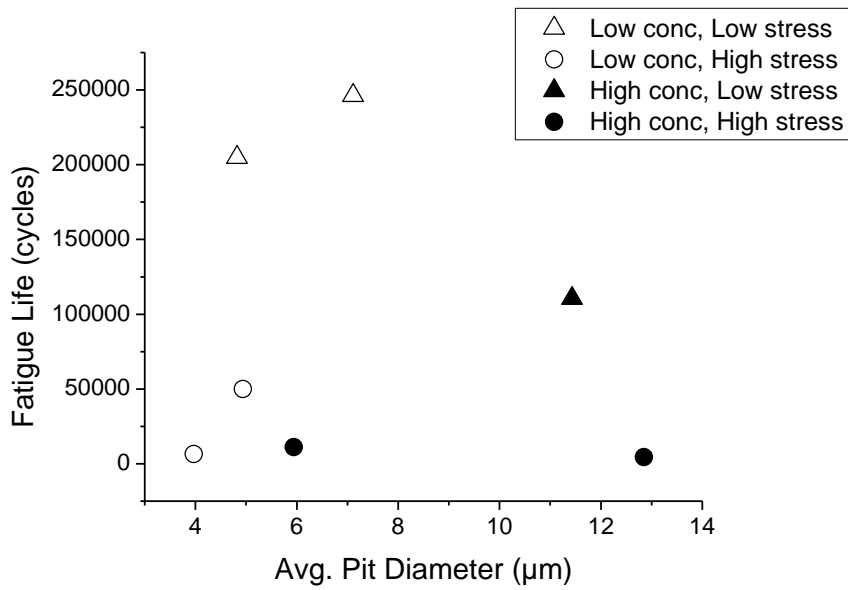


Figure 3.2.c
Influence of average pit diameter on fatigue life. When isolating stress levels, a larger average pit diameter generally corresponds to shorter fatigue life. This trend is not observed, however, when isolating LSC within stress levels.

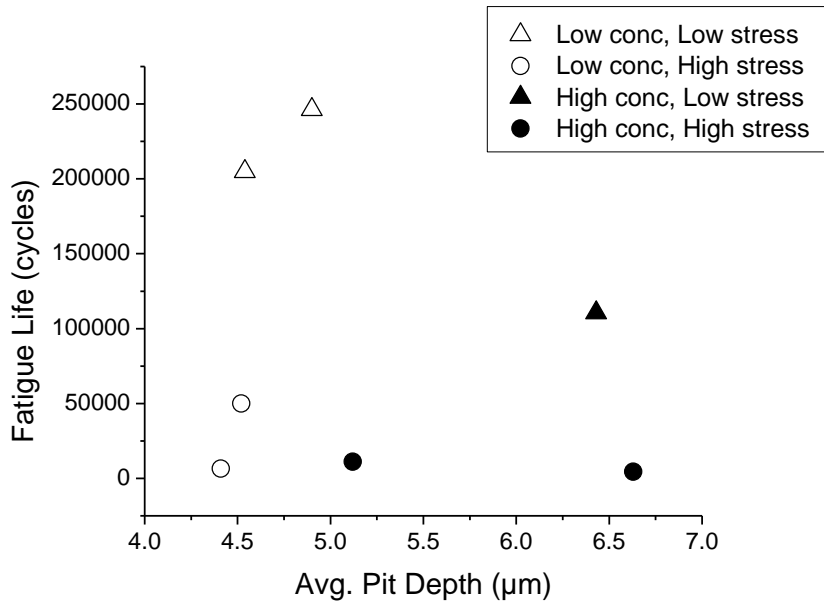


Figure 3.2.d

Influence of average pit depth on fatigue life. When isolating stress levels, a larger average pit depth generally corresponds to shorter fatigue life. This trend is not observed, however, when isolating LSC within stress levels.

3.3 Task III: Analysis of the Crack Initiating Pits

3.3.1 Size Metrics

This section (3.3) investigates pitting metrics further by narrowing the scope of analysis to the local level. First, the size metrics of the fatigue crack initiating pit were compared to the rest of the pits on the sample to see where they fall on the pit size distributions. These results for each sample were then compared to those of the other corroded samples to see if there was a trend of where the crack initiating pit sizes fell on the pit size distribution for each sample. The size of the primary crack-initiating pit was determined for each corroded sample. Metrics of pit size included pit diameter and pit depth. These metrics were obtained from SEM in conjunction with the WLI data. They were then compared to the size metrics of all other pits in the gauge section of the sample. Figures 3.3.1.a-b, indicate the diameter and depth, respectively, of the crack initiating pit in the context of the distribution of the largest 5% of pits. In fact, no matter the salt concentration or the stress level, the primary crack initiating pit was among the largest 1% of pits with respect to both pit diameter and pit depth, even for the primary crack initiating pits that lied outside the gauge

section (Samples M3-127 (HSC, high stress) and M3-128 (LSC, high stress)) as was determined by post-test SEM. This has been observed before where crack initiation occurs at one of the largest pits on a material [22,33–35]. Chen et al. assumed that the pit-to-crack mechanism was simply crack growth out-competing pit growth [34,35]. This mechanism was supported by the fact that the crack-initiating pit size was larger at lower stresses and smaller at higher stresses, allowing more time for the pit to grow at low stress and allowing less time at high stress. Thus, once a pit grows large enough, a crack initiates. Though the initiating pits lied within the largest one percent of all pits on each sample, the primary crack initiating pit was usually not the largest in either metrics of diameter and depth, and in no case the largest in *both* diameter and depth, as demonstrated by the examples in Figure 3.3.1.c.

This result of cracks initiating from one of the largest pits, but not the largest, has been observed before. Medved et al. [77] claimed that the critical factor causing fatigue cracks to not necessarily initiate at the largest pit was because of the presence of higher stress concentrators elsewhere (e.g. at another pit or cluster of pits, especially where rigid corrosion damage features exist [49]) whereas the largest pit would have a more blunt morphology (lacking rigid features). Another factor that can affect the distribution of stress concentration about a pit—resulting in fatigue crack initiation not to occur at the largest pit—is the orientation of a pit’s diameter with respect to the loading direction. Huang et al. [78] determined that for two overlapping pits, which create an elongated pit with a shared perimeter (hence, larger shared diameter than the diameter of either pit alone), their stress concentration is maximum as the length of these overlapping pits is oriented perpendicular to the loading direction. As such, if a pit has an elongated diameter (as is common for two coalesced pits, especially of similar size), its stress concentration is maximized if aligned perpendicular to the direction of the load and minimized when aligned parallel to the direction of the load. These are subtle differences that can cause crack initiation to occur at a pit with slightly higher maximum stress concentration as opposed to another pit of similar size. Nevertheless, given the subtlety of the differences, cracking still initiates from one of the largest pits.

The fact that cracks initiated at one of the largest pits makes sense, given the differences between the categories of salt concentration. HSC samples tended to have more large pits as shown by the pit size distributions and as reflected by HSC’s higher average pit sizes as was shown in Figures

3.1.d-f. Therefore, the HSC samples generally had the shortest fatigue lives of the three categories of pristine, LSC, and HSC.

Further investigation was done in light of the fact that the crack initiating pits fell within the top one percent in pit size. The average diameter and depth of the largest one percent of pits were determined (Figure 3.3.1.d) which showed similar overlap as when comparing averages of pit diameter and pit depth for all pits. Such average pit size metrics did not necessarily reflect the large difference in salt concentration with which the samples were corroded, even when isolating the largest one percent of pits. Similar variability in pit size was present among the largest 1% of pits as it was for all pits within each salt concentration category. Again, this variability reflects similar overlap in pit size between salt concentration categories for the largest 1% of pits as it was when accounting for all pits. Nevertheless, HSC samples generally had larger pit sizes among the largest 1% of pits even as there was some overlap of size between low and high salt concentration.

Plots were also constructed of fatigue life vs. average pit diameter (Figure 3.3.1.e) as well as fatigue life vs. average pit depth (Figure 3.3.1.f). These demonstrate that the average pit size of the top one percent of pits is not necessarily connected with fatigue life as was the case when considering the average pit size of all pits. However, a subtle trend can be found within each stress level where a higher average pit size of the largest 1% of pits roughly corresponds to a shorter fatigue life. This trend is not observed, however, when isolating salt concentration within stress levels. Due to the variability in these plots, another plot was constructed to illustrate fatigue life vs. the amount of pits greater than 10 μm (Figure 3.3.1.g). A 10- μm depth was chosen for this purpose since the pit depth distribution in Figure 3.1.1.c showed very low pit counts on all samples above a 10- μm depth compared to below 10 μm . A similar relationship was found for the high stress level where a higher number of large pits (> 10 μm) generally corresponded to a shorter fatigue life. This trend is also exhibited at the low stress level. Again, however, when considering only salt concentration for each stress level, this trend is not observed (particularly for low salt concentration). This suggests that bulk pit sizes, even when considering large pits only, do not entirely reflect fatigue behavior, though they are decent indicators. Therefore, other corrosion damage metrics must have also played a role, suggesting that an analysis of pitting metrics from a perspective local to the crack initiation site would provide more insight into the fatigue behavior.

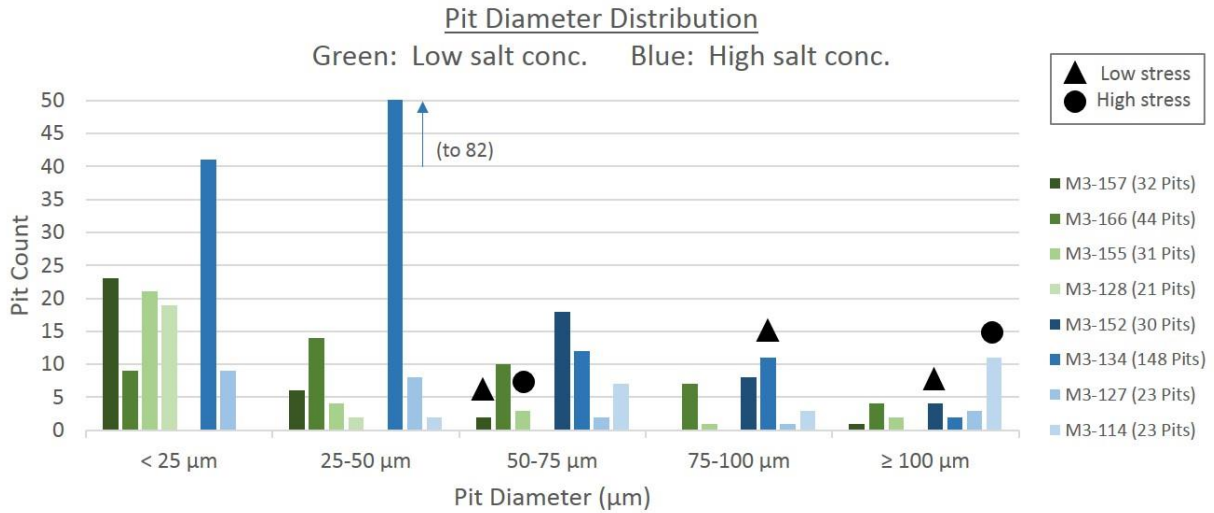


Figure 3.3.1.a

Pit diameter distribution of the largest 5% of pits on each corroded sample with the primary crack initiating pit marked over its respective bin (initiating pits that lied outside of the gauge section were not included as WLI scans only captured the gauge section of each sample).

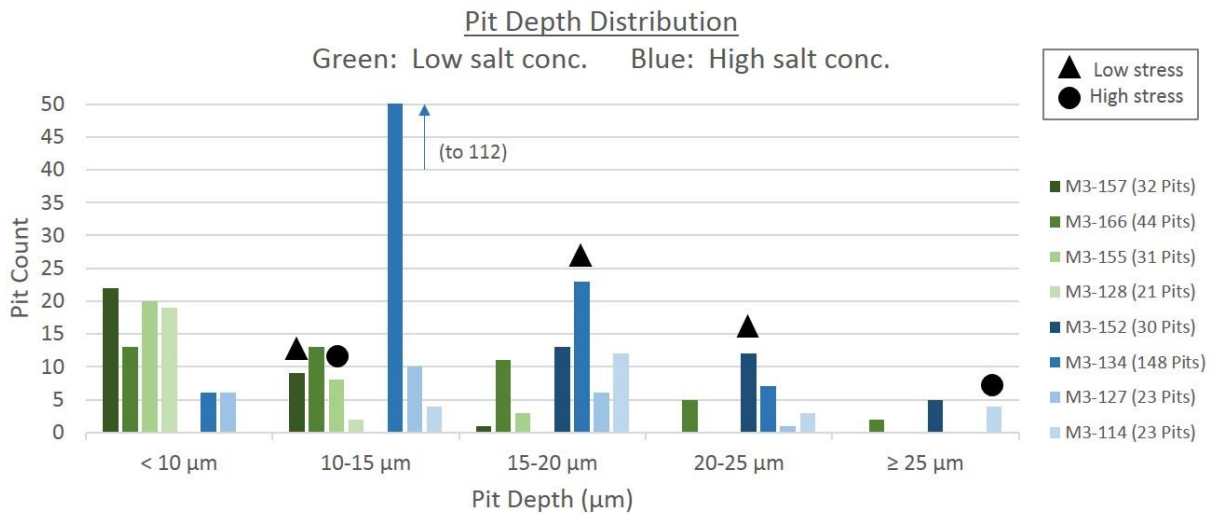


Figure 3.3.1.b

Pit depth distribution of the largest 5% of pits on each corroded sample with the primary crack initiating pit marked over its respective bin (initiating pits that lied outside of the gauge section were not included as WLI scans only captured the gauge section of each sample).

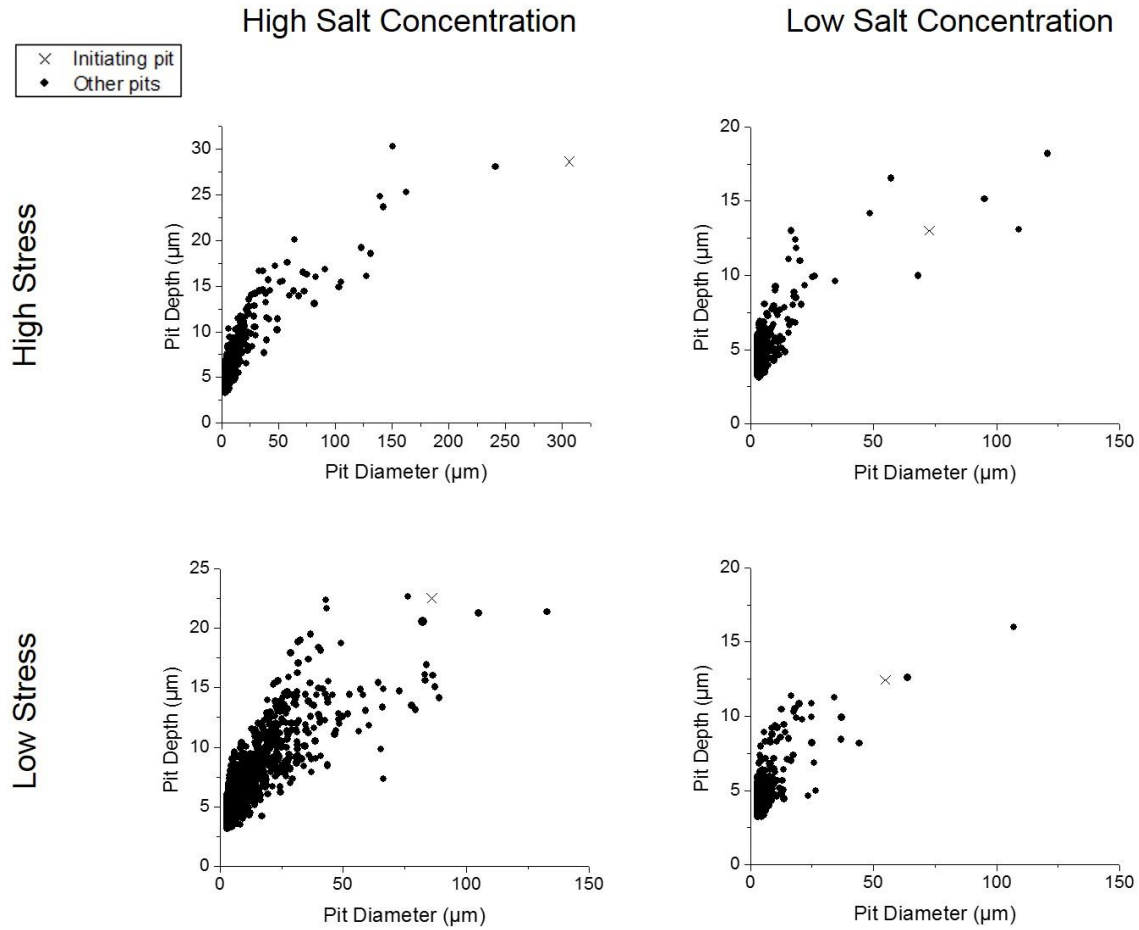


Figure 3.3.1.c

Primary crack initiating pits marked among all pits for samples from each category. Initiating pits were among the largest 1% of all pits for each corroded sample, but they were usually not the largest in either depth or diameter, and in no cases were they the largest in both depth and diameter.

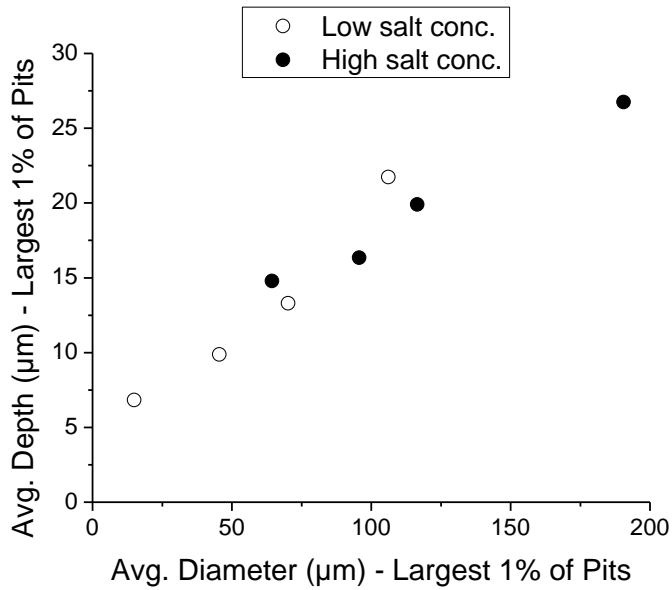


Figure 3.3.1.d

Average pit depth vs. average pit diameter of the largest 1% of pits on each sample. This resembles the trend when accounting for all pits on each sample (Figure 3.1.d). There is variability and overlap, but average pit sizes of the largest 1% of pits on each sample are generally larger on HSC than on LSC samples.

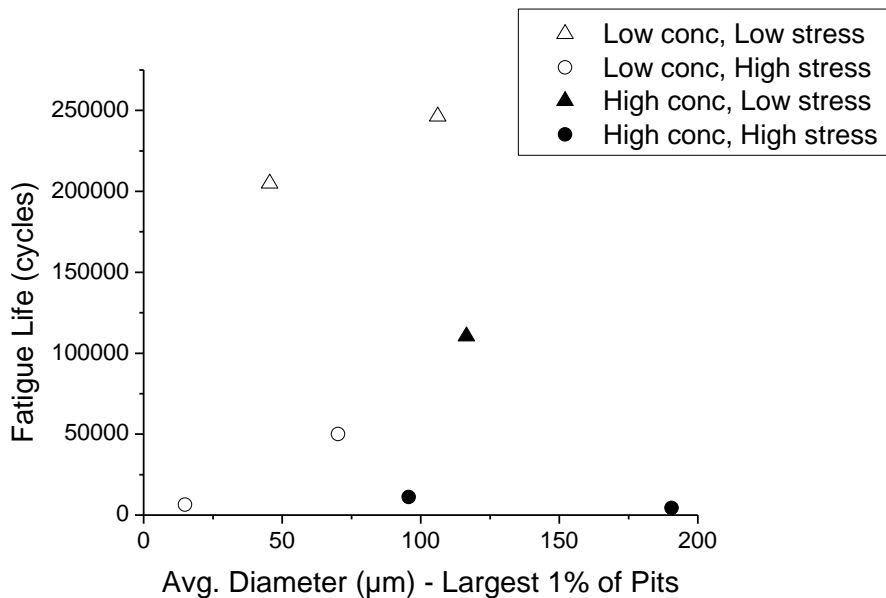
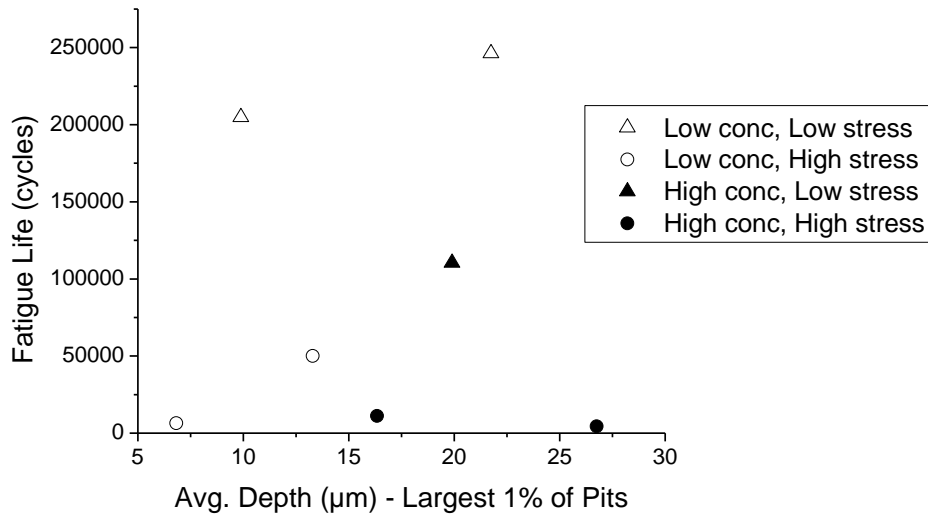


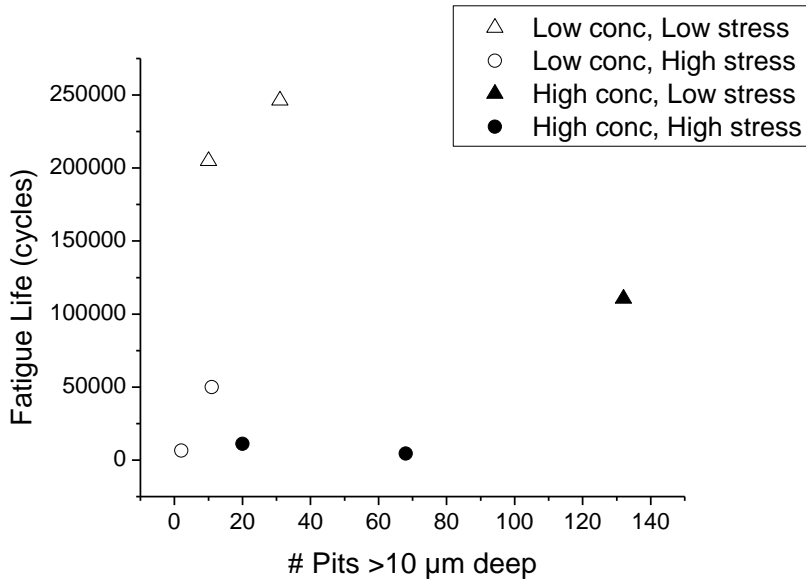
Figure 3.3.1.e

Even when isolating the largest 1% of pits on each sample, a similar trend results as when accounting for all pits on each sample (3.2.c). A higher average pit diameter roughly correlates with lower fatigue life when isolating stress levels, but this is not the case when isolating LSC within stress levels.



3.3.1.f

Even when isolating the largest 1% of pits on each sample, a similar trend results as when accounting for all pits on each sample (3.2.d). A higher average pit depth roughly correlates with lower fatigue life when isolating stress levels, but again, this is not the case when isolating LSC within stress levels.



3.3.1.g

Considering only the pits on each sample that were deeper than 10 μm, a trend can be seen for each stress level where higher numbers of pits greater than 10 μm generally resulted in shorter fatigue life. However, this trend is not observed for LSC within stress categories.

3.3.2 Localized Damage Region Metrics

The regional metrics included average pit diameter and depth, pitting density, and pit spacing. The objective of this effort was to determine if any regional metrics stood out among the others in terms of their connection with fatigue behavior. To do this, the metrics of the 13.3-mm² region where the primary crack initiated were compared to the metrics of all other regions of the sample. If, for example, the average pit depth of the crack initiating region had the highest value of all other regions on the sample surface, it would suggest that the average regional pit depth was an important variable for the fatigue behavior particularly if this result were consistent among all corroded samples.

For each corroded sample, after the primary initiating pit and its respective region were found, this region was then compared to the rest of the regions on the gauge section with respect to various pitting metrics. These regional metrics included pit count, average pit diameter, average pit depth, and average nearest neighbor distance (ANNd). Examples of such results are shown in Figures 3.3.2.a-d for Sample M3-152 (HSC, low stress).

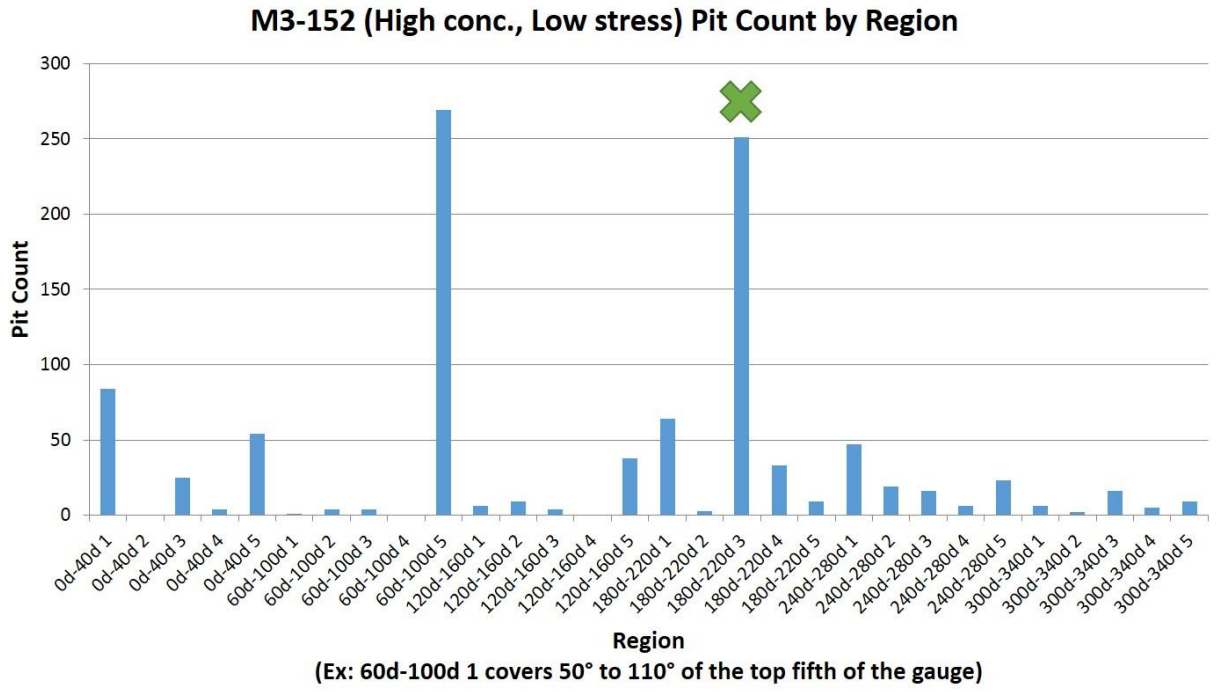


Figure 3.3.2.a

The crack initiation region was marked to compare with all other regions on each sample (e.g. M3-152: HSC, Low stress) with respect to pit count.

M3-152 (High conc., Low stress) Average Pit Diameter by Region

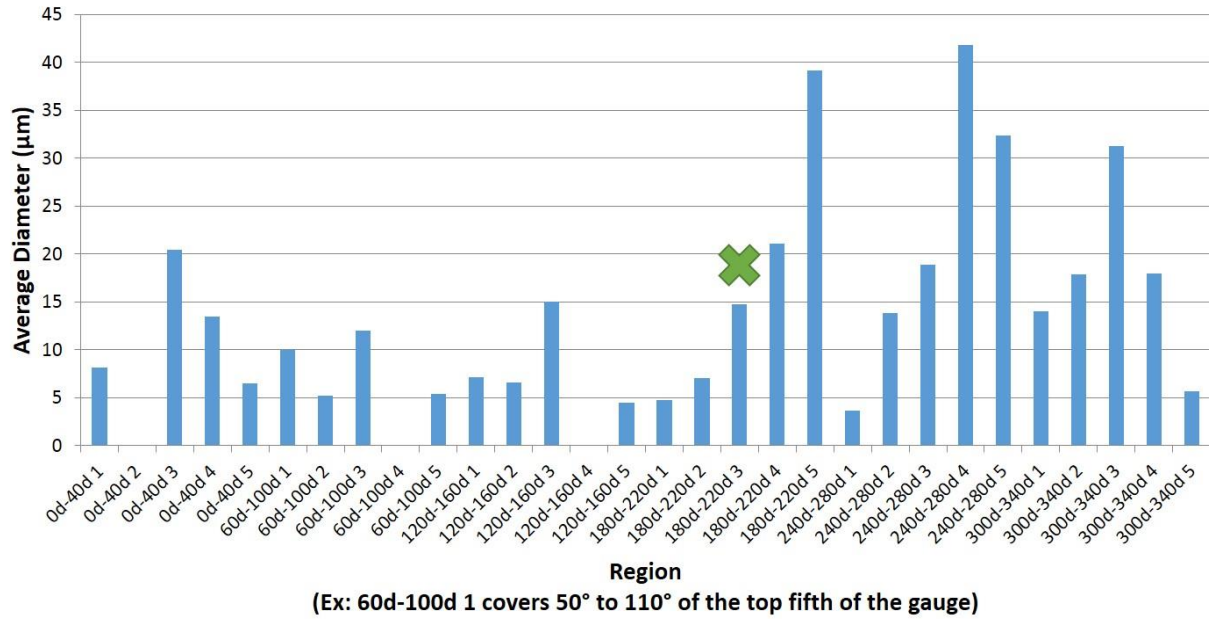


Figure 3.3.2.b

The crack initiation region was marked to compare with all other regions on each sample (e.g. M3-152: HSC, Low stress) with respect to average pit diameter.

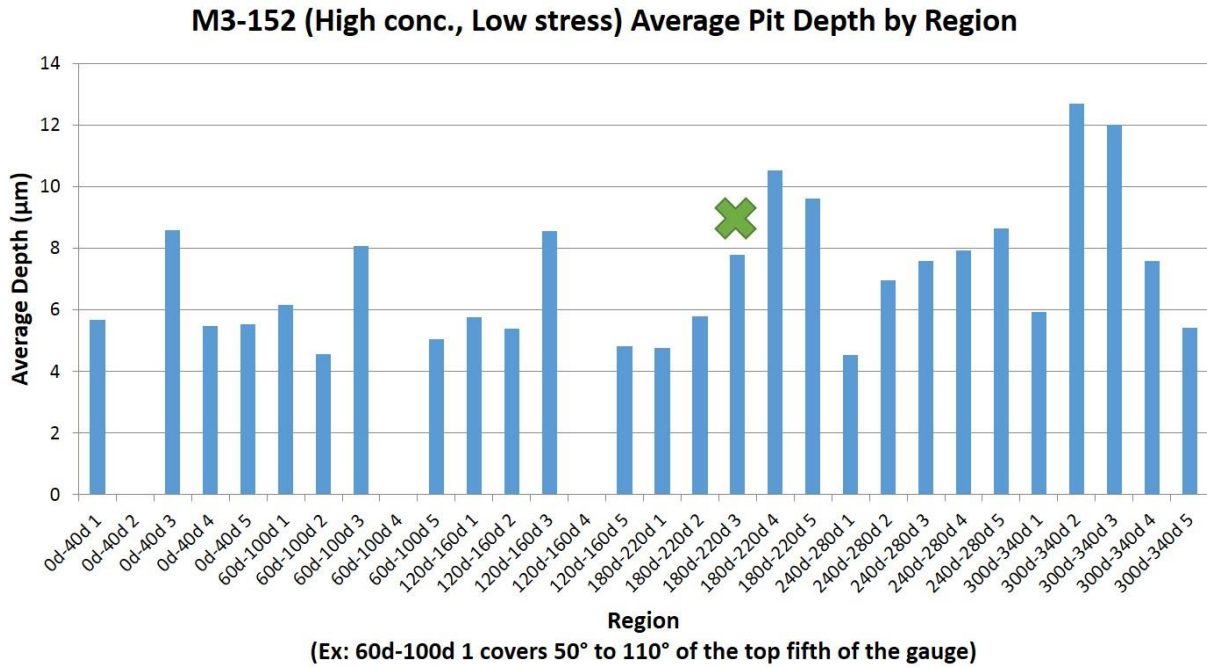


Figure 3.3.2.c

The crack initiation region was marked to compare with all other regions on each sample (e.g. M3-152: HSC, Low stress) with respect to average pit depth.

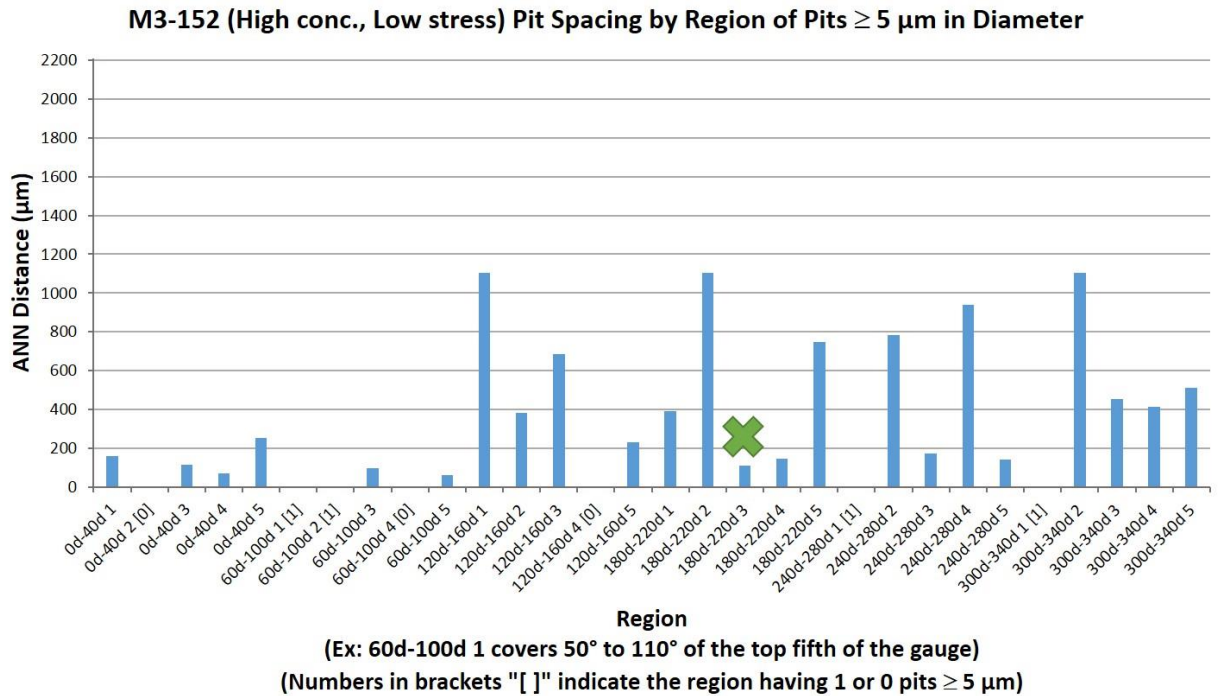


Figure 3.3.2.d

The crack initiation region was marked to compare with all other regions on each sample (e.g. M3-152: HSC, Low stress) with respect to average nearest neighboring pit distance (ANNd).

3.3.2.1 Pitting Density

The percentile with respect to pitting density of the crack initiation region for each sample is shown in Figure 3.3.2.1.a. On four of the seven samples, the primary crack initiation region had a pitting density that was greater than 80% of the other regions on the sample; however, only one sample had its primary crack occur in the most densely pitted region. The results suggest that pitting density is a more critical metric on the regional scale as opposed to the bulk scale for the purposes of predicting fatigue cracking.

It was also observed from the results that pitting density tended to show a better correlation with the crack initiation location for samples that were corroded with the high salt concentration (3 out of 4 samples above the 80th percentile) and at high stress levels (3 out of 4). These observations suggest that higher salt concentration is more likely to produce regions of relatively high pitting density that are more vulnerable to fatigue crack formation. They also suggest that regions of

relatively high pitting density are more vulnerable to fatigue crack formation than other regions when the specimen is under relatively high stress.

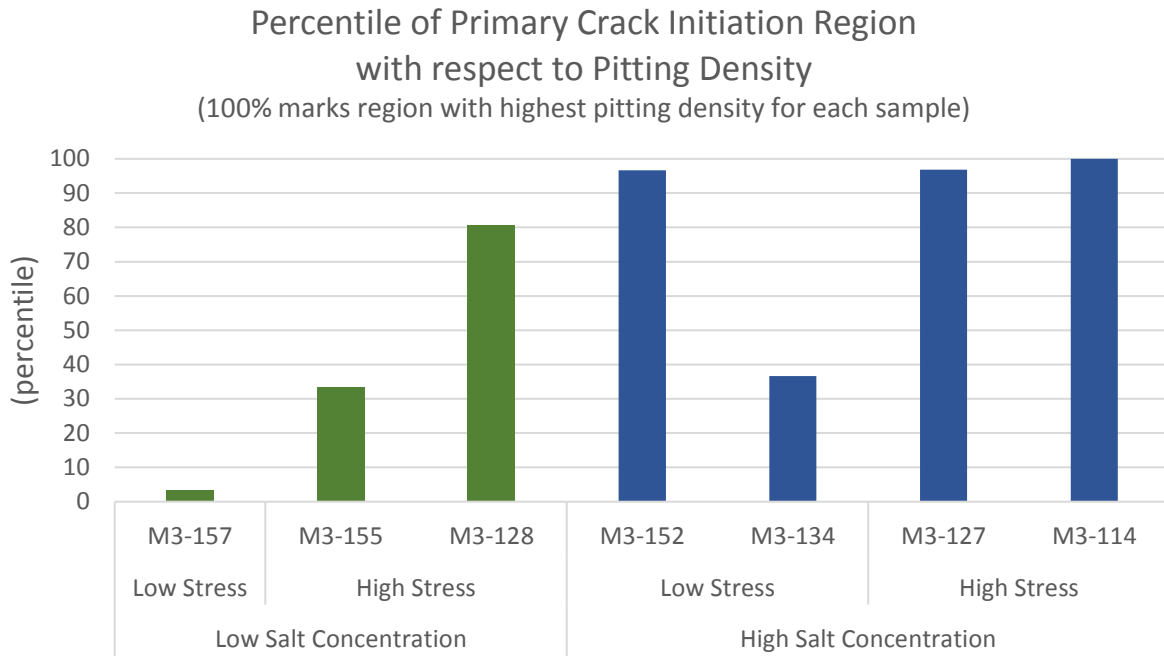


Figure 3.3.2.1.a

Most crack initiation regions were above the 80th percentile, primarily relating to high salt concentration and high stress. There was strong variability, however, with the remaining regions below the 40th percentile.

3.3.2.2 Average Pit Size

The percentile of the average pit diameter of the crack initiation region for each sample is shown in Figure 3.3.2.2.a. For five of the seven samples, the region where the primary crack initiated had an average pit diameter that was greater than the fiftieth percentile among all regions on the sample surface. However, crack initiation occurred in the region of highest average pit diameter on only one of the samples. Generally, average regional pit diameter showed the best correlation with the crack initiation location for the HSC samples (3 of 4 samples above the 50th percentile). As such, higher levels of salt concentration tended to cause fatigue crack initiation in regions of large pit diameter.

Average regional pit depth of the crack initiation region showed similar results (Figure 3.3.2.2.b). Most of the samples had crack initiating regions which were above the fiftieth percentile in average pit depth; however, none of them had the highest average regional pit depth.

In summary, for regional pit size as well as regional pitting density, the variability in percentiles reflected a weak trend as to the location of crack initiation. Plots were made to demonstrate if there was a coupled effect of the regional metrics of average pit size and density. The results exhibited variability in that the crack initiation regions were not always high in both pitting density and average pit size, showing no consistent relationship between these two regional metrics. The plot in Figure 3.3.2.2.c shows a sample’s regional data that demonstrated a relationship between these two metrics in which the crack initiated in a region of high pitting density and relatively high average pit size, but this was not the case for most samples. These results again emphasize that variability should be expected, even when considering regional metrics. A crack is merely more likely to form in a region of relatively high pitting density; also, a crack should form at a large pit, but that does not mean the average pit size reflects the large size of the crack initiating pit.

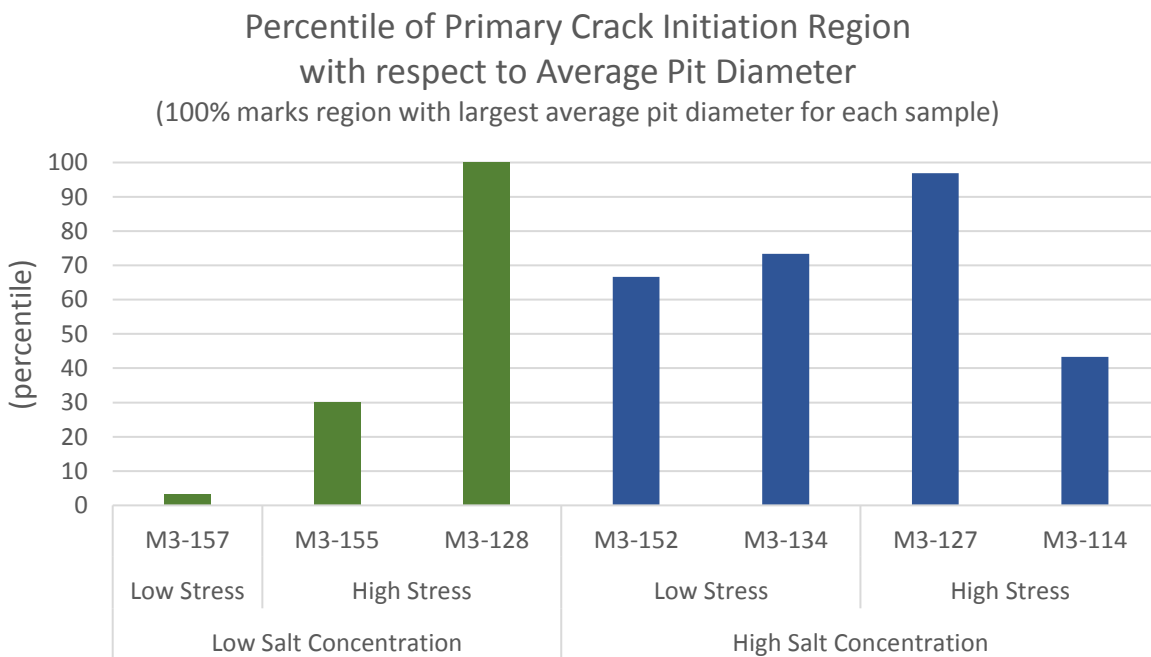


Figure 3.3.2.2.a

Most crack initiation regions were among the top third with respect to average pit diameter. There was much variability, however, as the remaining regions were below the 45th percentile.

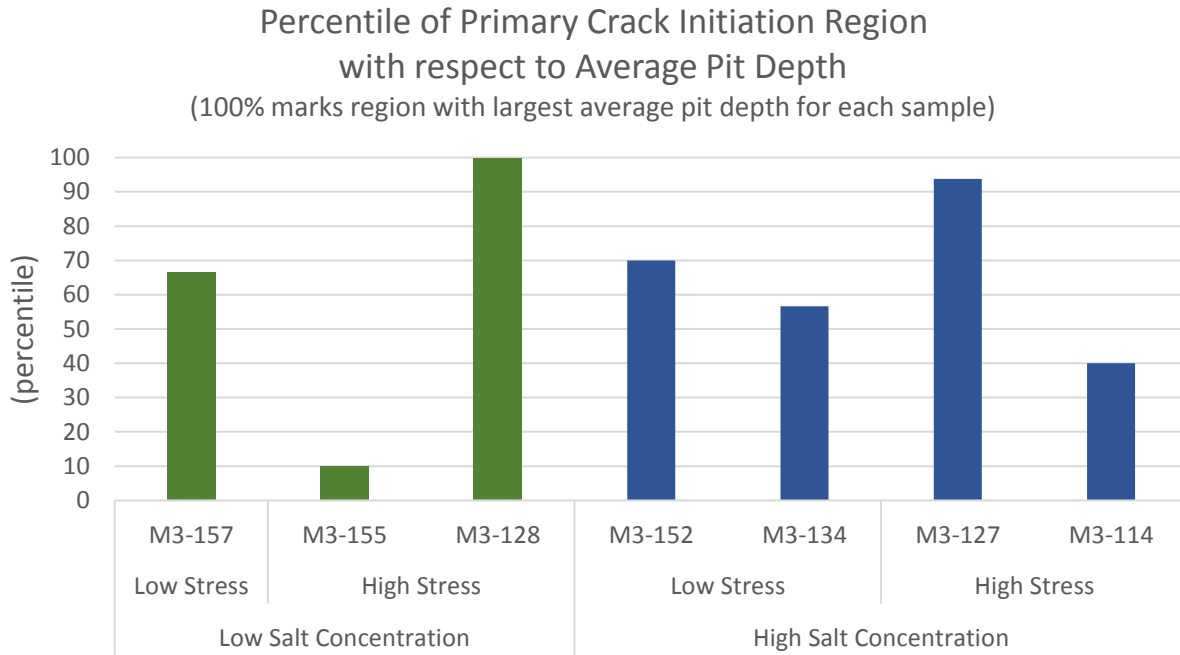


Figure 3.3.2.2.b

Most crack initiation regions were among the top third with respect to average pit depth, all but two were above the 50th percentile, and all but one were at least of the 40th percentile.

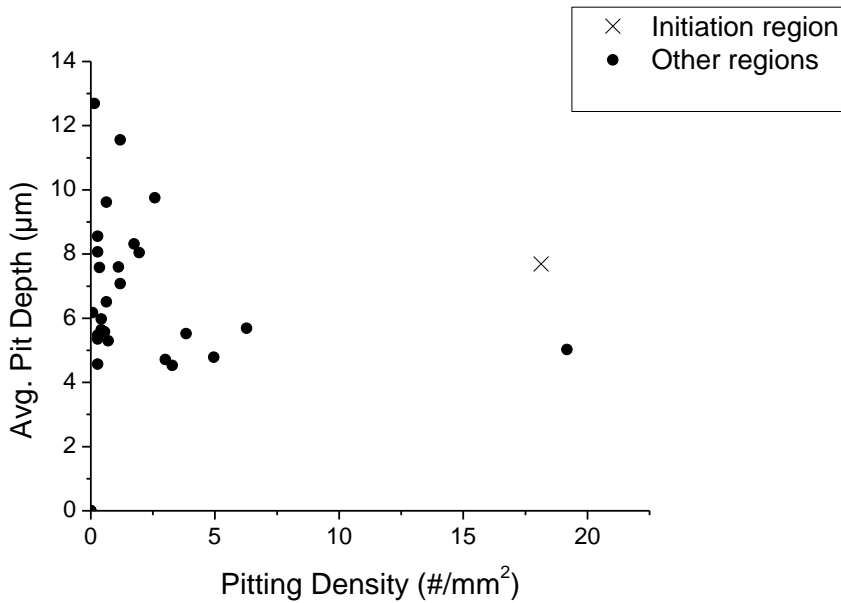


Figure 3.3.2.2.c

Average regional pit depth vs. regional pitting density of the regions on M3-152 (HSC, Low stress). This sample demonstrated unsurprising results where the crack initiated in a region of high pitting density and relatively high pit size. However, this was not a trend among the corroded samples as several cracks initiated in regions of either or both low average pit size and pitting density.

3.3.2.3 Pit Spacing

Pit spacing was the final regional metric investigated. Medved et al. found fatigue cracking to often occur where pits were clustered [77], i.e. where there was smaller pit spacing. It was hypothesized that fatigue cracks would tend to initiate in regions of lower pit spacing, meaning that they would tend to initiate where pits were closer together. The metric to measure this “closeness” was the average nearest neighbor distance, ANNd, which was defined as the average distance from the center of one pit to the center of its nearest neighbor.

Figure 3.3.2.3.a shows the percentile of the crack initiation region with respect to the pit spacing metric of ANNd. Only samples whose crack initiation site fell within the gauge section are included in this analysis. The results showed high variability in the percentile. However, there was no overlap for this metric between salt concentration categories. The crack initiation regions were lower in percentile of ANNd for the HSC samples than they were for the LSC samples. This suggests that the likelihood for the crack initiation location to be in a region of lower pit spacing

is increased with higher salt concentration. *In toto*, the variation in the data suggest that the pit spacing, as described by ANNd, within each region is not a strong predictor for the location of crack formation.

In summary of these results along with the rest of the local/regional results, it was determined that average regional pit size and regional pitting density are important metrics to consider. Regional pit spacing appears to only be important with high salt concentration. Unlike other results, the size of the crack initiating pit being among the largest 1% was a consistent result, suggesting that pit depth and diameter are important on an individual basis. Primary cracks can be expected to nucleate from one of the very largest pits. Salt concentration generally influenced the trends of the pitting metrics, thus the crack initiation behavior, in that HSC samples accounted for most of the primary cracks that initiated in regions of large average pit size, high pitting density, and short pit spacing.

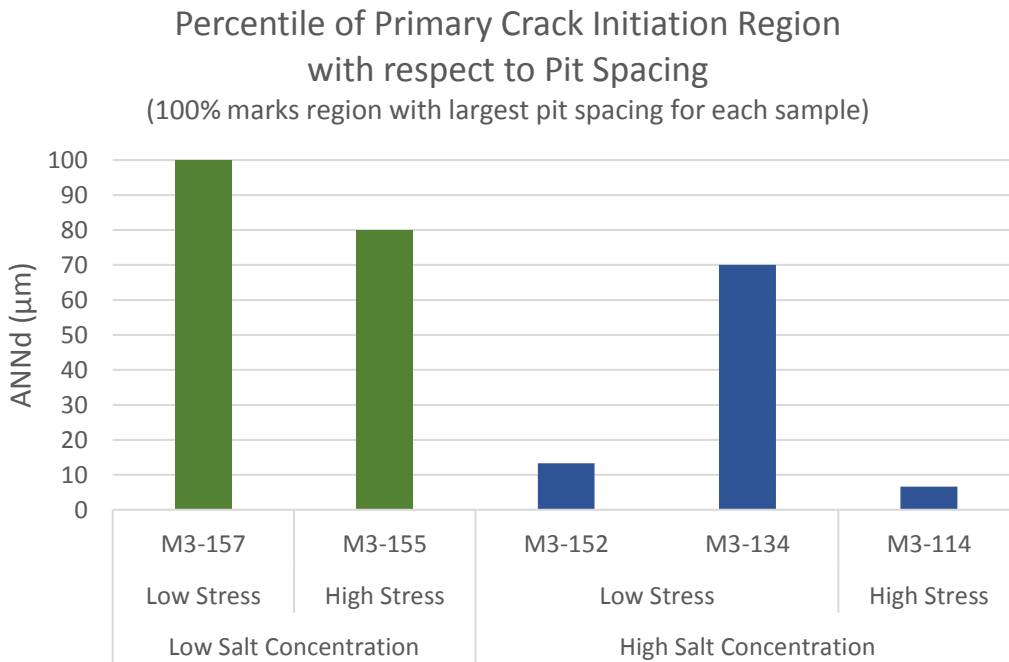


Figure 3.3.2.3.a

Only two crack initiation regions were below the 50th percentile in average nearest neighboring pit distance. Though variability was high, there was no overlap, i.e. HSC samples here showed shorter ANNd for their crack initiation regions than those of the LSC samples.

3.4 Task IV: Crack Initiation and Crack Propagation

3.4.1 *Quantifying the Relative Roles of Crack Initiation and Propagation*

The proportion of crack initiation life out of the total fatigue life for each sample was determined to assess the contribution of crack initiation life vs. crack propagation life. Plots were constructed to demonstrate the relative contributions of crack initiation and crack propagation to the total fatigue life for each sample and for each category of salt concentration and stress.

The crack initiation lives are displayed in Figure 3.4.1.a (by sample) and in Figure 3.4.1.b (averaged by category of salt concentration and stress level). Sample M3-134 was excluded because it was not representative due to being tested at two different stress levels. These graphs plot the percentage of the total fatigue life necessary to initiate a crack to 25-50 μm . The plots show a trend that crack initiation represents a large portion of the fatigue life at low stress and a smaller portion at high stress, especially with high salt concentration. This trend is shown to be steady when the samples are averaged by category.

These results evoke two important considerations. One is that the crack initiation life to 25-50 μm constitutes the majority of the overall fatigue life at low stress levels. This trend is uniform for pristine, LSC, and HSC samples. An increased role of the crack initiation life of the overall fatigue life with decreased stress is expected for pristine samples. However, as discussed previously, researchers have suggested that the presence of sufficiently severe corrosion damage can decrease fatigue life by well over 50%, even toward nil for hot corrosion on nickel-based superalloys. The current results demonstrate that the severity of the current corrosion damage features due to hot corrosion with the low salt concentration are not sufficient to drastically reduce the crack initiation life. This observation is upheld by comparing the crack initiation life and total life of the LSC samples to that of the pristine sample at low stress. These similarities suggest that the corrosion damage features did not serve as crack initiation sites that were drastically more severe than the native microstructural features. This furthermore parallels the prior explanation for the crack initiation site of Sample M3-166—an LSC sample fatigued at low stress—which was at a location that was not a corrosion pit but rather at a microstructural inhomogeneity. Such results are likely due to the nature of the corrosion damage morphology where prior research has shown that smooth corrosion pits (as observed in this study) are significantly less potent for crack initiation than pits with more rigid morphology [17,48,49], and Turnbull et al. [79] suggested that deviations in ideal

pit shape, i.e. smooth and uniform morphology, fluctuate the strain distribution about a pit. The other consideration is that even at high stress, the pristine sample, as well as one of the LSC samples, demonstrated similar crack initiation proportion of total fatigue life as all samples in the low stress category. The HSC samples at this high stress, along with the other LSC sample, demonstrated a significantly diminished role of initiation life. This suggests that at such higher stress levels the severity of the corrosion damage exceeds some critical threshold to cause a drastic reduction in the overall fatigue life.

The primary crack initiation regions of the samples that showed significantly shorter crack initiation lives than the rest of the samples (i.e. where crack initiation life was less than 65% of the total life) were all above the 80th percentile in regional pitting density. Two of these three samples also had primary crack initiation regions that were above the 90th percentile in average pit size; whereas the third of these three (M3-114: HSC, high stress) had a primary crack initiation region of below the 10th percentile in pit spacing (i.e. closely-neighboring pits), had the largest of all primary crack initiating pits, and had the largest bulk average pit size of all corroded samples. The crack initiation region of Sample M3-152 (HSC, low stress) had the second-highest pitting density, pit size, and lowest pit spacing of all primary crack initiation regions. It also had a larger primary crack initiating pit size than that of M3-128 (LSC, high stress) whose crack initiation life was just over 30% of the total life. However, because M3-152 was fatigued under low stress, M3-152 exhibited an initiation life that was 96% of the total.

These results are consistent with the corrosion damage distributions for LSC and HSC reported in Figures 3.3.1.a-b, where the number of pits on the high end of the distribution is substantially higher for the HSC than for the LSC. Coupled with the crack initiation analysis, these data reinforce the importance of considering the upper tail of the distribution. Specifically, the increased number and severity of the largest corrosion pits on the HSC sample resulted in a higher probability of such a feature being in a deleterious local region (as quantified in Section 3.3.2 using pitting density, average pit size, and pit spacing) or near a deleterious microstructural feature to enable an enhanced crack formation process. While such behavior is not overtly novel, this work systematically demonstrates this synergy and identifies that corrosion morphologies with a less severe tail of the distribution (and/or less severe local regions) can result in lower crack formation lives.

In toto, the results suggest that the corrosion damage features serve as preferential locations for crack nucleation. However, due to the nature of the damage (likely the smooth morphology and relatively small scale of pitting), crack initiation life is not drastically reduced at low stress levels. At higher stress, the driving force for crack nucleation about the pits becomes sufficient to significantly reduce the required portion of fatigue life responsible for crack initiation.

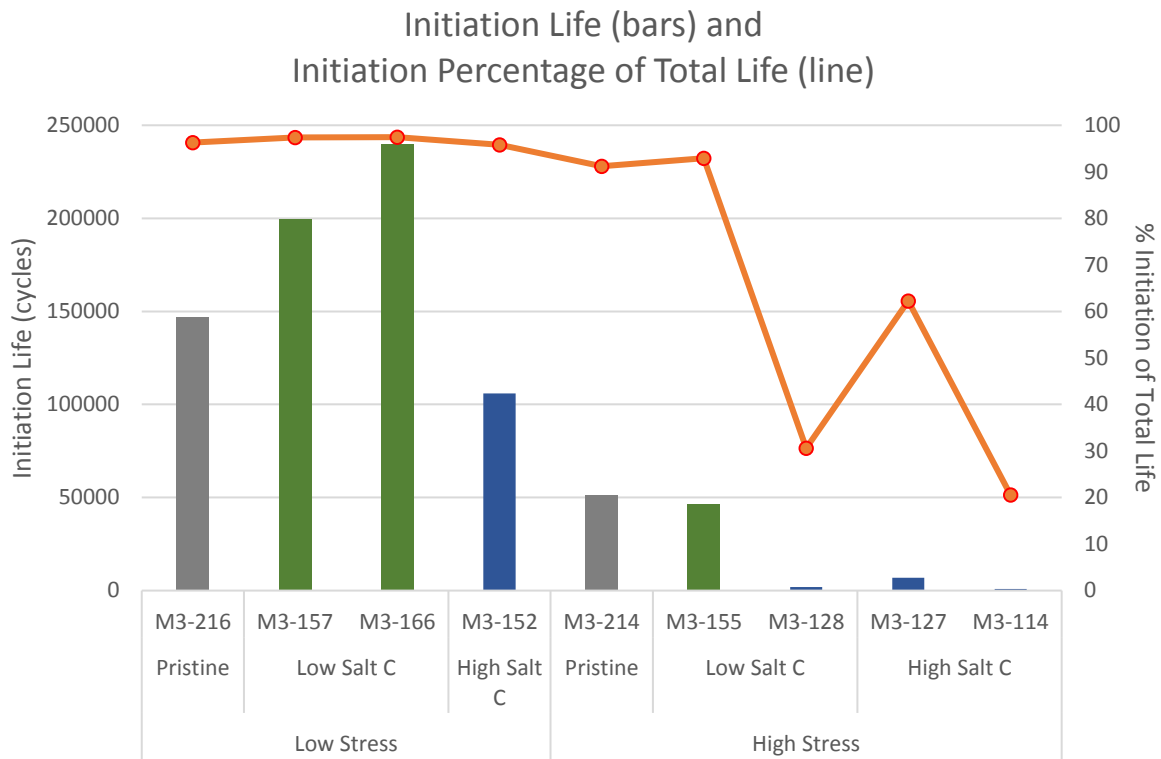


Figure 3.4.1.a

Crack initiation life and its percentage of total fatigue life. Fatigue behavior was dominated by crack initiation at lower stress, and the dominance of initiation tended to decrease with an increase in stress level and salt concentration. (Excludes M3-134 due to being tested at two different stress levels.)

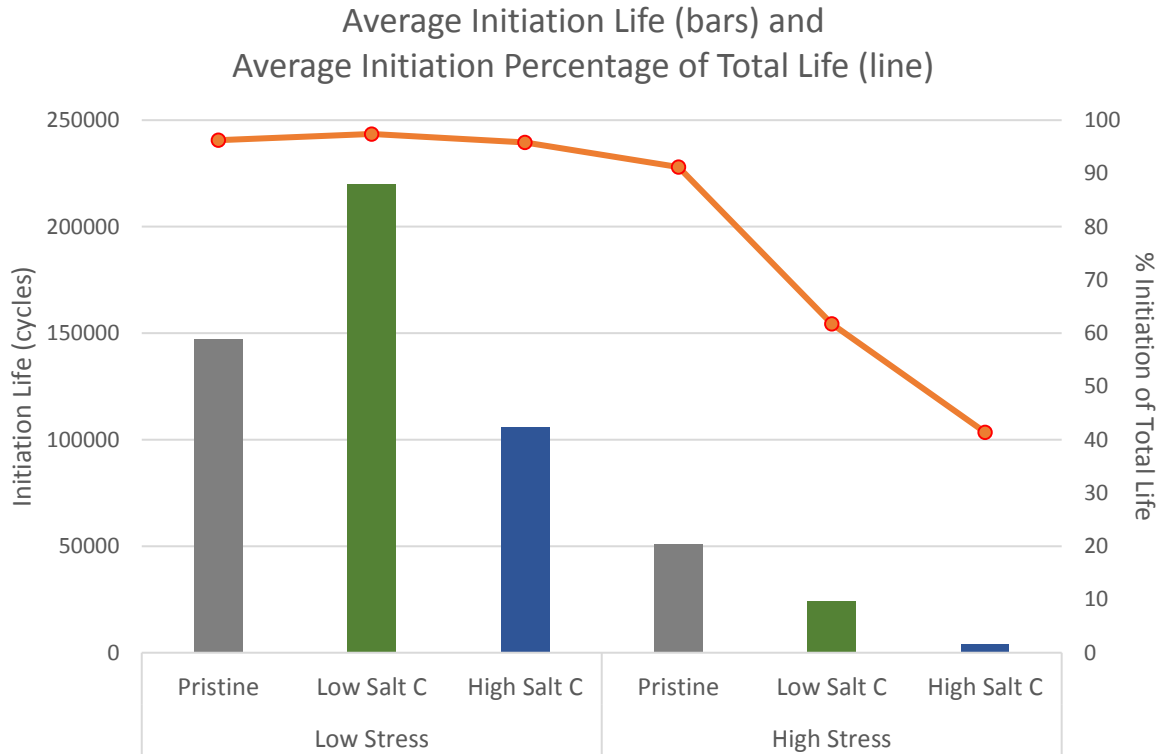


Figure 3.4.1.b

Average crack initiation life and its percentage of total fatigue life. Fatigue behavior was dominated by crack initiation at lower stress, and the dominance of initiation tended to decrease with an increase in stress level and salt concentration. (Excludes M3-134 due to being tested at two different stress levels.)

3.4.2 Crack Growth Rates

This section discusses the crack growth behavior of the material. The fatigue cracks involved in this study were small, particularly during early crack growth. The complications of quantifying the stress intensity factor for such crack sizes is discussed. An alternate route of analyzing crack growth was taken, and corrosion severity (via LSC or HSC) and stress level were evaluated for their roles in fatigue crack growth.

Using linear elastic fracture mechanics (LEFM) to determine the stress intensity, K , is straightforward for larger continuum cracks. However, for smaller crack sizes, especially in the cases of this study where cracks initiate from a pit rather than from the bulk surface, some linear elastic assumptions break down. In such cases, the free ends of the initial crack front do not yet envelop the pit to reach the outer sample surface. The fatigue cracks on the samples for this study

can be considered small during the early stages of crack propagation. Criteria for what is considered a small crack, where a stress intensity range, ΔK , based on LEFM is not necessarily accurate, are: (1) the crack length is at most on the order of the microstructural dimensions (e.g. grain size), (2) the plastic zone is large compared to the crack (i.e. the plastic zone essentially envelops the crack, and the crack does not make any appreciable size change to the plastic zone), and (3) the crack is simply physically small (i.e. ≤ 0.1 -1 mm) [80,81]. At least two of these criteria, (1) and (3), are met in this study as the average grain size is 25-27.5 microns. Crack sizes below about 250 microns in these samples can be considered both microstructurally small (being on the order of the grains size) and physically small (being shorter than 0.1-1 mm long).

Aside from enhanced plastic zone and grain boundary effects for cracks being small relative to the plastic zone, grain size, or mere absolute length, another consideration for the expected ΔK value to not necessarily represent the actual stress intensity range for small cracks is that crack closure may occur during cyclic loading at relatively low stress ratios, i.e. $R = 0.1$ [82,83]. With closure, the crack tip does not experience an effective load even though the applied load on the sample is still above zero. Due to the lack of crack wake distance, such closure effects are not considered pertinent as they would be for low ΔK values for long cracks. This is one postulated reason for the well-known small crack behavior that is higher than standard long crack results. To avoid non-conservative evaluations of the fatigue behavior of a material, Suresh and Ritchie [81] proposed that ΔK should be adjusted such that it begins at a smaller value at a higher crack growth rate than the customary threshold stress intensity, ΔK_{th} .

Due to the complications outlined above and lack of clarity on the true K-solution for the small cracking about a 3D corrosion feature, no attempt was made to calculate the ΔK value associated with a given crack size [69]. Alternatively, forms of illustrating the crack growth were constructed as shown in Figures 3.4.2.a-b. A select sample was used to represent each category on these plots to control for geometry. Excluded samples had crack initiation sites that either lied inside the outer sample surface or outside of the gauge section.

The crack growth rates could only be obtained for a limited range of crack lengths for each category on the graph of crack growth rate, da/dN , vs. crack length, a (Figure 3.4.2.a). Growth rates are shown for the bulk of the propagation life on this plot, but the beginning and end of the propagation life lacks data because of the approach in which average data was plotted between

known points. Thus, Figure 3.4.2.b was constructed to illustrate the growth rates in a different manner (crack length vs. number of cycles of crack propagation) such that each plot on the graph extends from the commencement of crack propagation (end of crack initiation) all the way to failure.

These plots demonstrate that crack growth rates primarily depend on stress level as opposed to the level of corrosion damage. This is expected considering that the only role of the different salt concentrations is to impart the initial corrosion damage distribution and the assumption that residual salt product has been removed. Furthermore, this work shows that the subtlety of different corrosion morphologies associated with the different salt concentrations does not impact the crack propagation behavior. These plots also demonstrate the expected dependence of the crack propagation behavior on the crack tip driving force. While the ΔK values were not explicitly calculated, the morphology of the cracking from the corrosion damage was generally similar for each case, as such increasing the stress level increases the driving force, thus faster crack progression would be expected for higher stress levels. The slow crack growth behavior is consistent with the trends of relative initiation and propagation life previously reported.

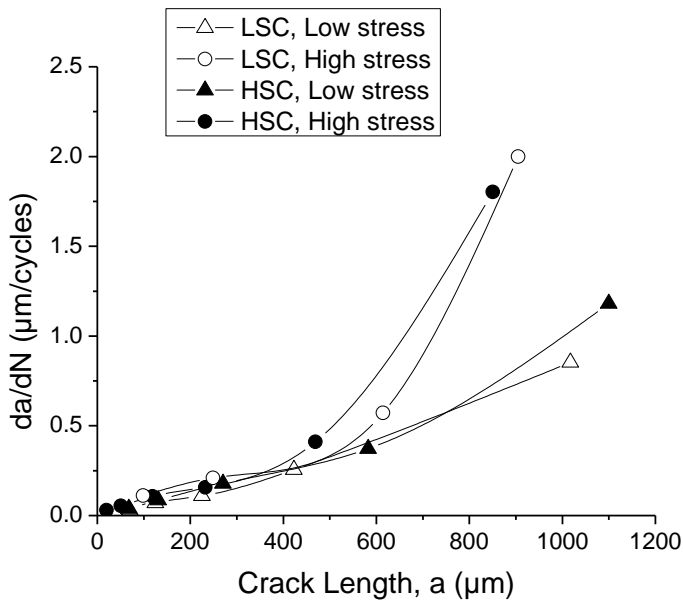


Figure 3.4.2.a

Crack growth rate vs. crack length for the most representative sample, according to crack geometry, for each category of salt concentration and stress level.

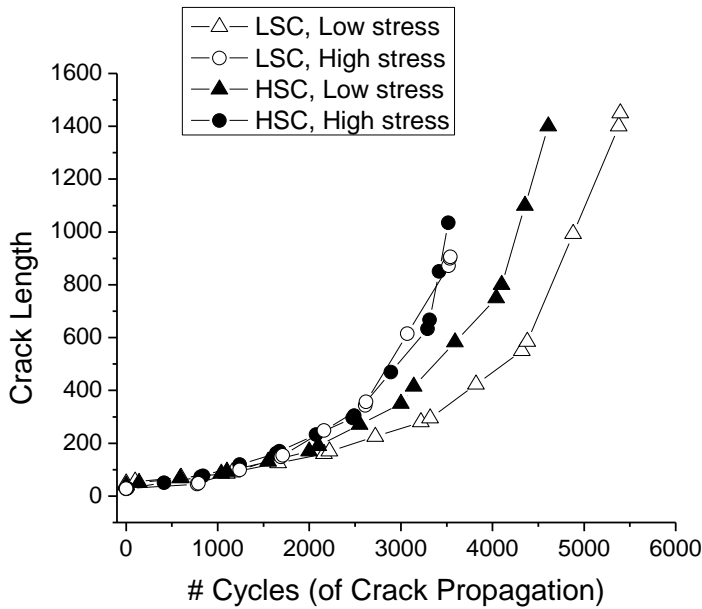


Figure 3.4.2.b

An alternative perspective to crack growth (to that of Figure 3.4.2.a) displays the entire propagation life with plots of crack length vs. cycles of crack propagation (beginning at a crack size of 25-50 μm) for the most representative sample, according to crack geometry, for each category of salt concentration and stress level.

3.4.3 Oxidation

In addition to the important trends in initiation life reported above, fractographic analysis revealed that on four specimens there were regions proximate to the crack initiation site that showed distinct topography and color under SEM on the fracture surface over lengths of 7-40 μm (Figures 3.4.3.a-d). Striations were recognized inside each of these regions, following a crack-like pattern from a common central location on the edge of the crack-initiating pit. The presence of these striations suggested that these distinguishable regions were formed after the crack nucleated, possibly at the crack tip during early crack growth.

Further investigation was performed on these regions using energy-dispersive x-ray spectroscopy (EDS/EDX). EDS line scans were taken across each of these regions to determine any compositional trends in contrast with the surrounding crack surface. An example of these scans is shown in Figure 3.4.3.e (Sample M3-157: LSC, low stress) where high oxygen counts were detected in the region of interest, even relative to nickel, the principal element of the alloy. At the point along the line where the high-oxygen region meets the remainder of the crack surface, oxygen

abruptly decreases while nickel increases. A similar pattern was shown for the other two samples that exhibited this region. These EDS results suggested that oxidation either occurred at the crack tip during early crack growth or in the crack wake as the tip extended.

This contribution of oxidation to the fatigue crack initiation process has been demonstrated in other studies on nickel-based superalloys [12–14,84–87]. Fatigue crack initiation is generally based on local factors of mechanical driving force (i.e. stress concentration), material properties (e.g. grain size, crystal structure), and environment (e.g. corrosive agents, temperature) [21]. More specifically, oxidation is deleterious for the crack initiation process by various factors, including: an oxygen or air environment, elevated temperature, and low loading frequency [18,84–87]. This study included all three of these factors. It is known that oxygen was present during testing due to the air environment. However, additional might have been active during crack initiation which could have come from residual salts that accompanied any remaining corrosion product. The tests were performed at a temperature of 704°C, providing a heightened ability for oxygen to diffuse into the material; and the loading frequency was only 0.3 Hertz.

These observations prompted three questions. First, why does this oxidation behavior occur in only a subset of the samples? Second, why does the oxidation behavior only extend a short distance? Third, why does the oxidation behavior extend different distances on different samples? Two hypotheses were proposed to explain this observation: (1) the appearance of the region was related to the time it in which the crack wake was exposed, thus related to the fatigue life, including propagation life, or (2) despite the cleaning protocol, there were residual salts that remained in the vicinity of the pit which enabled the oxidation. The first hypothesis was proposed because this oxidation region appeared only on the samples that had the longest fatigue lives whose crack initiated from a pit (and did not appear on the samples with the shortest fatigue lives), and the size of the region appeared to be related to the fatigue life as well. The second hypothesis was proposed because not all of the corrosion product could be cleaned off of the surface before testing; as such, there might have been residual salts that remained at some pits along with some corrosion product.

To test these hypotheses, first the length of the oxide region was measured from the point of crack formation to the edge of the oxide perpendicular to the crack wake. Figure 3.4.3.f shows how this length was related to the fatigue life which did show a relationship. Not only was there a

correlation, but at high stress the relation is steep, and at low stress the relation is less steep. These observations support Hypothesis 1 as a time-dependent factor is evident.

For further investigation, a cross section was taken through this oxide region, perpendicular to the crack growth direction, to reveal a profile. Results would support Hypothesis 1 if there were a gradient of the oxide layer where it would be deeper near the pit and taper in thickness to the edge of the region. This would further demonstrate a time-based dependence where the regions near the pit would experience the longest time in the wake, thus should have the deepest oxide. To test Hypothesis 2, EDS was performed to determine if the nature of the oxide was different in the region local to the corrosion damage. If there was a limited supply of sodium and/or magnesium sulfates, it would be reasonably expected that the composition of the oxide in this region would be distinct from the rest of the crack wake and probably similar to that of the corrosion product in the pit.

The analysis was performed on Sample M3-152 (HSC, low stress). The oxide region on the fracture surface of this sample was distinct yet not excessively large. A cross section was cut out of this region using a focused ion beam (FIB) lift-out technique with an FEI Helios G4 UC. First, a focused electron beam was used to deposit a small strip of platinum with a focused electron beam across the oxide region that extended 26 μm from the crack formation site (4 μm past the edge of the region into the bulk crack surface). This strip of platinum served as a protective layer for a more aggressive deposit of a thicker layer of platinum using a focused ion beam of gallium ions. After this double layer strip of platinum was deposited, trenching was done around this strip to lift out a block of the ME3 material that included the platinum strip. Figures 3.4.3.g-h show the FIB platinum deposit and lift-out, respectively. The FIB sample was then placed on a grid for further FIB thinning to make a smooth cross section directly underneath where the platinum was deposited to reveal the profile of the oxide region under an FEI Titan transmission electron microscope (TEM).

Evaluating the cross-sectional scanning transmission electron microscopy (STEM) image in Figure 3.4.3.i, regarding Hypothesis 1, it is shown that there is no gradient in the depth of the oxide region. Rather, the oxide thickness is 200-300 nm thick in the region proximate to the corrosion damage where the oxide is visible on the fracture surface. There is then a sharp transition (over 0.1 μm) to an oxide layer with a thickness of roughly 100 nm; this layer was not visible in the SEM

images of the fracture surface. This finding is not consistent with the gradient aspect of Hypothesis 1 where a more gradual transition in oxide thickness would be expected if this regions was controlled simply by the crack wake exposure time. However, what was observed is consistent with literature expectation where the growth of the oxide would be relatively constant in thickness and no thicker than 1 μm [13]. The lack of a gradient could have been due to chromia and alumina which have been suggested to passivate the fracture surface on the inner part of the oxide layer adjacent to the alloy [12,13].

In order to evaluate Hypothesis 2, EDS spectra were gathered from various regions on this profile with a primary interest in determining if there was a difference between the nature of the oxide in the vicinity of the pit and the oxide farther away from the pit. The weight percent of select elements are shown in Figure 3.4.3.j in reference to the specific locations indicated in Figure 3.4.3.i. Two main findings were noteworthy. One was that the composition of the oxide on the fracture surface changes at the transition from the oxide region near the pit and farther away from the pit, particularly between the thicker 200-300 nm region and the thinner 100 nm region. The changes were that Ni, Co, and Cr decrease to a minimum at the thin oxide (location (e)), which was non-visible under SEM, while Nb, Ta, and Ti increase to a maximum at this thin oxide. To enlighten what these could mean, previous work suggests that Al, Cr, Ti, Nb, and Ni oxidize at the crack tip for similar material in a similar without salt where Nb is concomitant with decreased Ni and Co [13,84,88]. With all of these elements present with oxygen, and with increases in Nb accompanying decreases in Ni and Co, this is evidence that the thin oxide was due to an air-only contribution. Furthermore, non-selective oxidation has been suggested to occur at freshly exposed surfaces [13]. As this alloy showed a considerable presence of Ta, Ti, and Nb in addition to respectable counts of Ni, Co, Cr, Al, and Mo at the thin oxide layer, this further suggests that this layer was due to air as it is known that the crack constantly provided freshly exposed surfaces in the crack wake as the crack grew faster and larger. This further supports that a time-based phenomenon (e.g. Hypothesis 1) was augmented by a change in the environmental conditions, supporting Hypothesis 2. The other main finding from the EDS results was that traces of sodium and sulfur were detected in the vicinity of the pit, however in very small amounts; hence, they were not included in Figure 3.4.3.j. In summary, a time-based oxidation mechanism evidently also involved a chemically-based oxidation mechanism with residual corrosive agents. The length of

the thick, SEM-visible oxide layer was related to fatigue life while it also showed different compositions than what would be expected at a crack tip in air (i.e. at the thin oxide).

As such, the oxidation mechanisms could have incorporated explanations based on both hypotheses. Deeper investigation would be required to pinpoint the mechanisms behind the appearance of these relatively thick oxide regions on the fracture surface proximate to the crack formation site. Such extent of investigation in this direction, however, would reach beyond the realm of this study.

Though the cross-sectional analysis was only based on one sample, some explanations can be postulated as possible contributing factors to what was observed regarding the oxidation. The air environment is expected to have contributed to the oxidation, however, the abrupt drop in thickness, along with the changes in composition, suggest that it was not only air that contributed to the oxidation behavior. At the drop in oxide thickness, the oxygen might have either been exhausted from its source at the pit or there might have been a transport limitation that far away from the crack nucleation site.

Interestingly, despite experiencing this pronounced oxidation during early crack growth, these samples still had among the longest fatigue lives, even similar to the lives of some of the pristine samples. This could have been possible to crack tip chemical blunting where the crack tip was blunted by the corrosion process [89], in which case the oxidation would have occurred at the crack tip rather than in the crack wake, possibly explaining the thickness variations in the oxide region to be between 200-300 rather than maintain a constant thickness as in the thin, 100-nm layer past this oxide. Premature closure also might have occurred near the crack tip where a portion of the two crack surfaces would have made contact with each other for cycles whose stress ratio, R , was 0.1 [90]. This phenomenon would have caused a similar obstruction to the oxidation mechanism during cracking.

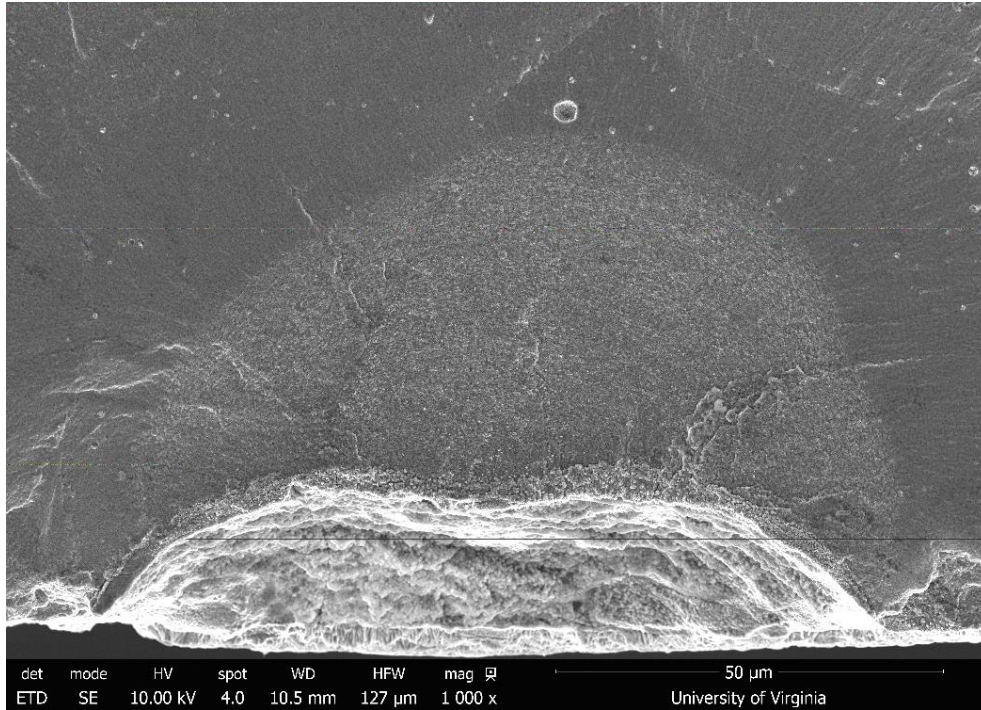


Figure 3.4.3.a
Crack initiation site of M3-157 (LSC, low stress).

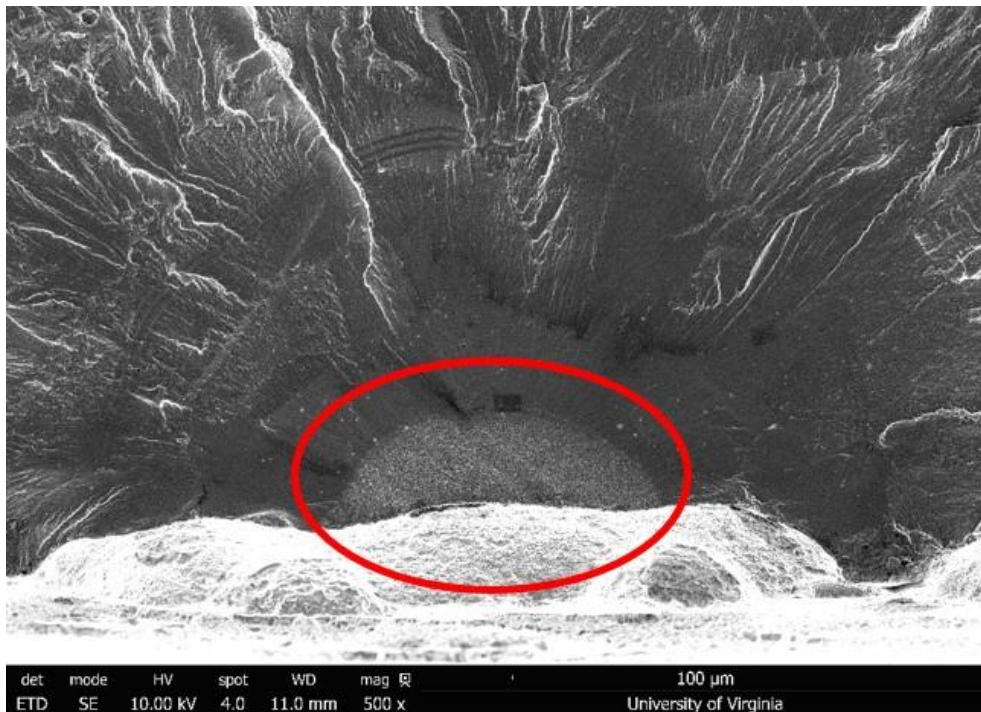


Figure 3.4.3.b
Crack initiation site of M3-152 (HSC, low stress).

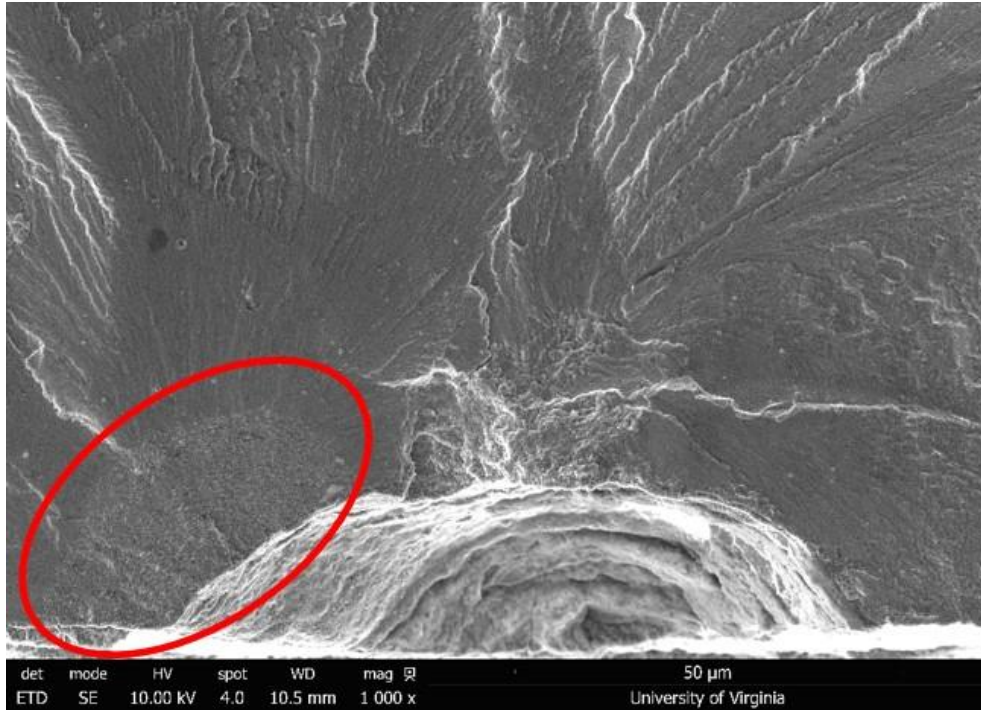


Figure 3.4.3.c
Crack initiation site of M3-155 (LSC, high stress).

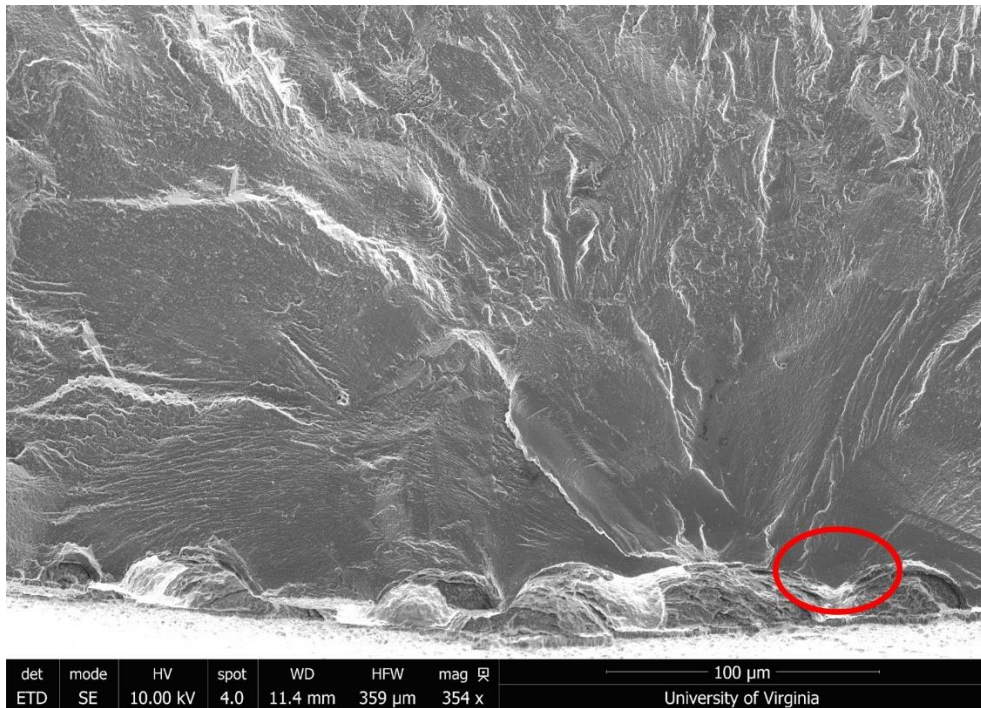


Figure 3.4.3.d
Crack initiation site of M3-127 (HSC, high stress).

Figures 3.4.3.a-d show distinguishable regions about the crack initiation site, having slightly rough topography with striations running approximately perpendicular to the crack initiation site.

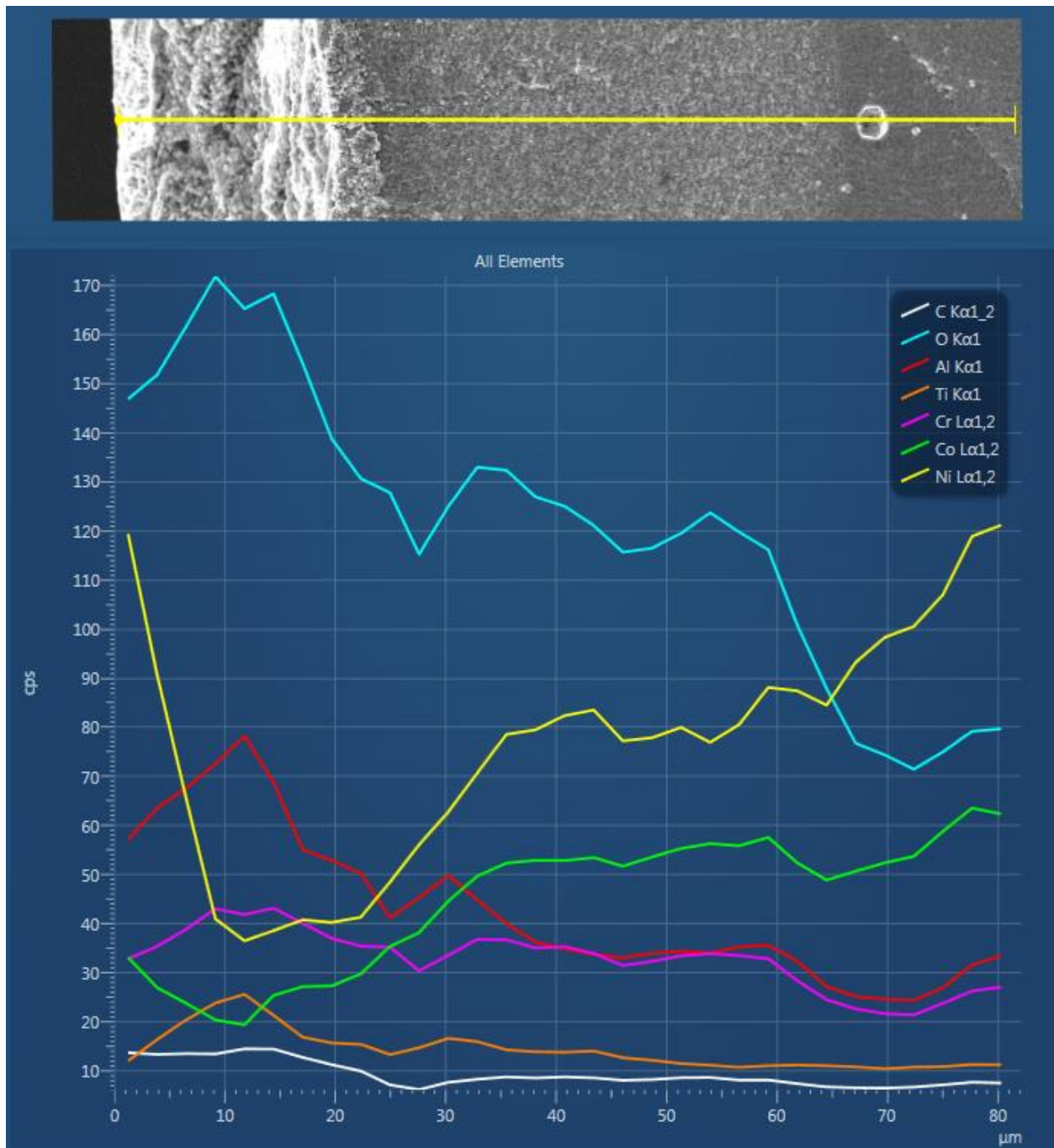


Figure 3.4.3.e

EDS line scan across the topographically distinguishable region proximate to the crack formation site on Sample M3-157 (LSC, low stress), which showed the longest region (40 μm) out of the four samples that showed such a region. Results showed high counts of oxygen with low counts of nickel in this region with an abrupt drop in oxygen at the edge of the region and into the smooth crack surface along with an abrupt increase in nickel.

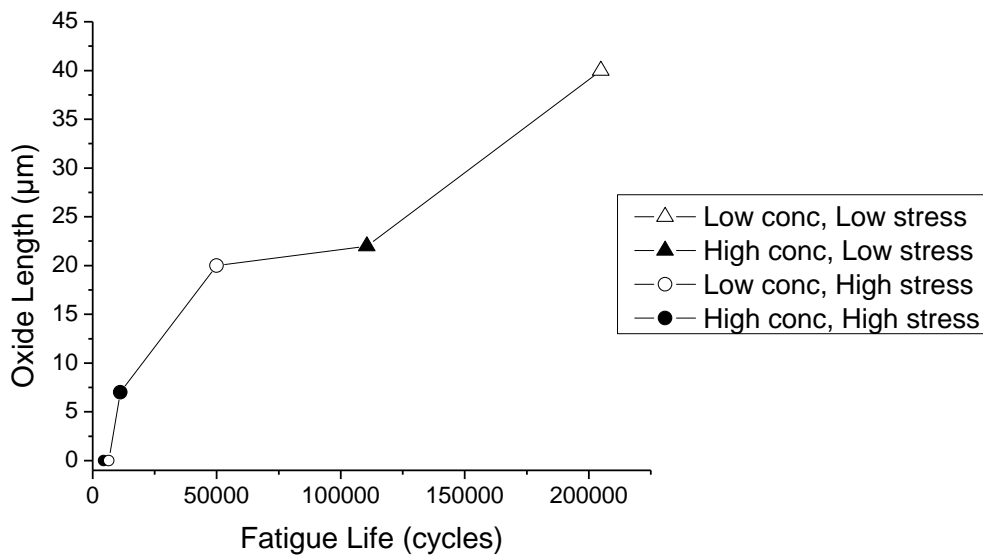


Figure 3.4.3.f

The oxide length correlated with fatigue life. The correlation is steeper at high stress and less steep at low stress. These results support the hypothesis of a time-dependent mechanism of oxidation on the crack surface.

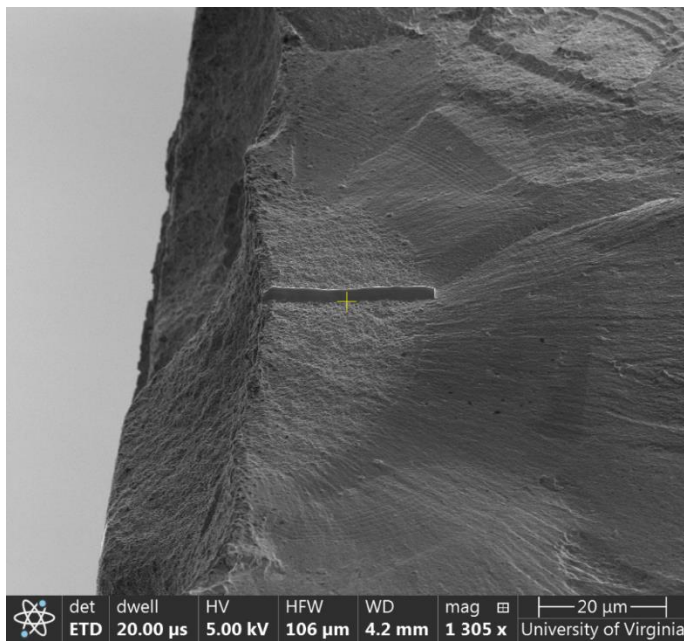


Figure 3.4.3.g

Platinum deposit over the oxide region extending from the crack formation site to the bulk crack surface perpendicular to the crack growth direction. Platinum deposit was necessary to protect material underneath it for analysis of the oxide profile.

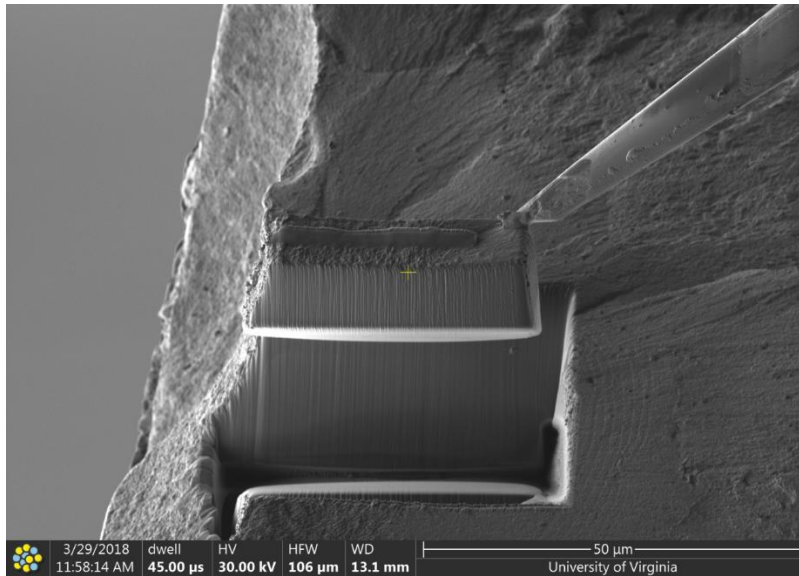


Figure 3.4.3.h

Material surrounding the deposited platinum was lifted out after trenching using FIB in preparation for trimming a profile of the oxide over the crack surface lying under the protective platinum deposit.

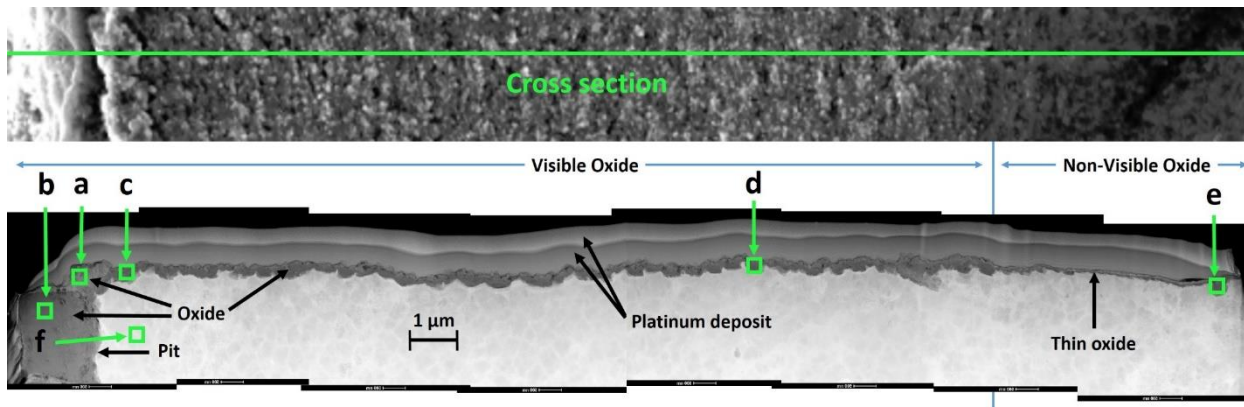


Figure 3.4.3.i (Refer to Figure 3.4.2.j)

STEM image of the cross section of the oxidation region on Sample M3-152 (HSC, Low stress) underneath the platinum deposit. A top-down view of the cross section is shown in the SEM image above. With no gradient in the oxide layer, it was 200-300 nm thick. The thin oxide layer (not visible under SEM) was 100 nm thick.

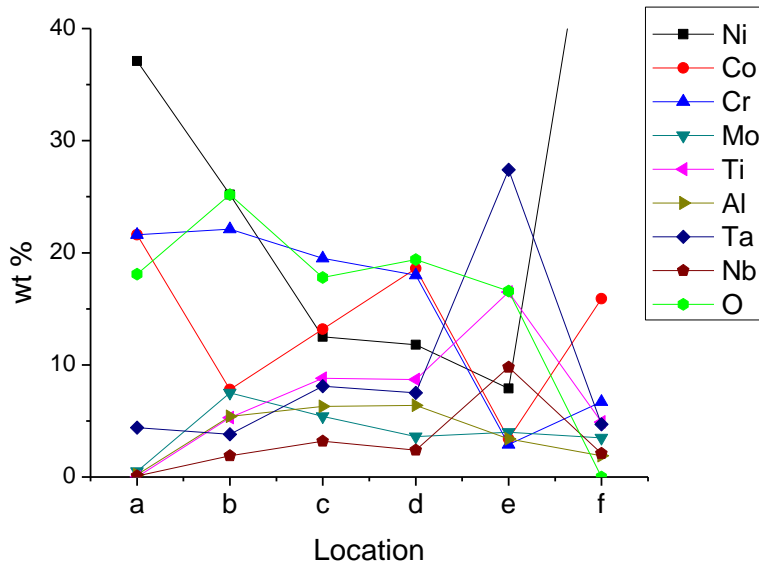


Figure 3.4.3.j (Refer to Figure 3.4.3.i)

Weight percent for select elements based on EDS spectra of oxide regions along the cross section indicated in Figure 3.4.2.i. There were notable differences in composition at the thin oxide (e) compared to the thick oxide and pit (a-d). Location (f) indicated the composition of the bulk alloy.

4 Summary/Conclusions

This study investigated the impact of hot corrosion pitting on the fatigue behavior of the nickel-based superalloy, ME3. Various pitting metrics were analyzed based on salt concentration during corrosion as well as different stress levels. Samples were divided into two categories of salt concentration used for corrosion: low ($\sim 2 \text{ mg/cm}^2$) and high ($\sim 30 \text{ mg/cm}^2$); and there were two pristine samples that were not corroded. Fatigue testing was done on these samples at two stress ranges, with a stress ratio of 0.1, at 1055 MPa for the low stress level and 1165 MPa for the high stress level (Table 2.2.3.a).

As several studies have assessed and modelled pit-to-crack transition by looking at fatigue crack-initiating pits, this study evaluated the effect of hot corrosion on fatigue by considering not only the crack-initiating-pit itself but also considering several other variables on a broader scale. Such variables included bulk metrics and regional (local) metrics of pitting. These metrics were analyzed in conjunction with two primary stress levels.

As total fatigue life could be broken down into crack initiation life and propagation life, the fatigue behavior with respect to these two phases of fatigue life was assessed in terms of their proportional contribution to the overall fatigue life.

4.1 Task I: Corrosion Characterization

Upon completion of the corrosion characterization by processing and analysis of the WLI topographic data of the corroded samples, there were only subtle trends between salt concentration and pitting metrics of pitting density and pit size—nothing particularly outstanding.

It was found that the samples corroded with low salt concentration (LSC) generally resulted in higher pitting densities and with smaller pit sizes on average (in diameter and depth) than the samples corroded with high salt concentration (HSC). However, the variability of these metrics between LSC and HSC reflected the subtlety of the trends.

A stronger trend was revealed when assessing only the pits that were within the largest 5% in both diameter and depth for each sample. It was clear that HSC samples had a greater number of large pits (particularly greater than $50 \mu\text{m}$ in diameter and $15 \mu\text{m}$ in depth) than LSC samples.

4.2 Task II: Impact of Stress and Corrosion Level on Fatigue Behavior

After testing, the general impact of salt concentration on the S-N curve of ME3 at 704°C was assessed. Though the large disparity between the two salt concentrations produced subtle differences in corrosion damage, according to the pitting metrics, LSC samples showed a slight effect on the S-N curve as they generally did not last as long as pristine samples. HSC showed a larger effect as its fatigue lives were generally shorter than both pristine and LSC samples. In summary, higher salt concentration tended to result in shorter fatigue life for a given stress level.

Upon analysis of the bulk corrosion metrics of pitting density and pit size in their relation to fatigue performance, pitting density did not show a distinct relationship with fatigue behavior, but pit size did show a slight relationship when isolating stress levels. Average pit depth showed a slightly stronger influence on the fatigue behavior than average pit diameter. This suggested that pit size is more critical than pitting density on the overall, bulk scale of the material surface; and when considering average pit size only, pit depth was evidently more critical than pit diameter.

4.3 Task III: Analysis of the Crack Initiating Pits

4.3.1 Pit Size

As post-test analysis dug deeper, corrosion metrics local to the crack initiation site were evaluated in light of the fatigue test results and the S-N curve. The size metrics of the primary crack initiating pits (the pits where the crack that led to failure originated) were assessed to show where they fell in the size distributions of all pits for each sample.

The most palpable relationship between any pitting metrics and fatigue behavior was that the primary crack initiating pits were among the largest 1% of pits on the surface of their respective sample. They were among the top 1% with respect to both pit diameter and pit depth; however, they were usually not the largest pit for either of these size metrics, and they were in no case the largest in *both* diameter and depth.

With larger pits on average, this finding explained why HSC samples showed a larger impact on the S-N curve as there were more large pits to cause higher stress concentrations to induce fatigue crack initiation. The effect of larger pits made up for a lower overall pitting density. Again, this suggested that pit size is a more important factor for fatigue behavior than pitting density.

4.3.2 Region of the Crack Initiating Pit

Regional metrics were assessed in light of where on the sample surface the primary fatigue crack originated to determine if there was a relationship between the fatigue crack initiation site and any pitting metrics in its vicinity.

Though there was variability in where the fatigue crack initiated, it was usually in a region that had high pitting density and large average pit size. Specifically, the pitting density, average pit diameter, and average pit depth of the crack initiation region were typically higher than the overall average for a given sample.

Pit spacing was also investigated. It was defined as the average distance from the center of a pit to the center of its closest neighboring pit. Shorter average nearest neighbor distance (ANNd) was not necessarily connected with the fatigue crack-initiating region. About half of the samples had a relatively small ANNd in the crack-initiation region compared to other regions on the sample, whereas other samples had relatively large ANNd in their crack initiation region. The results, however, suggested that the crack initiation region was related to smaller ANNd on HSC samples.

Of the above four regional pitting metrics, larger average pit depth had the most consistent connection with the crack initiation region. It is suggested that pit depth showed a slightly stronger influence on the fatigue behavior (from both the bulk and regional perspective) than pit diameter or other pitting metrics due to having a higher influence on the stress concentration at a pit [91].

Overall, though trends were observed, the crack initiation region usually did not have the highest pitting density, largest average pit size, or shortest ANNd. A similar observation was noted where Co and Burns [49] showed that fatigue cracks generally do not form at the most severe corrosion features. It can be concluded that fatigue crack initiation is highly variable with respect to where cracking will initiate; and it is merely more likely that cracking will occur where there is higher pitting density, where there are larger pits, and (for HSC) where pits are closer together (as observed by [77]).

4.4 Task IV: Crack Initiation and Crack Propagation

4.4.1 The Relative Roles of Crack Initiation and Propagation

The portion of crack initiation life and crack propagation life were distinguished as they additively comprise the total fatigue life. Analysis of the relative portion of each of these stages revealed the significance of the role of each in terms of the categories of salt concentration and stress level.

It was shown that fatigue crack initiation life was much larger than crack propagation life for all corrosion damage categories (pristine, LSC, and HSC) at low stress. This was also the case for the pristine sample at high stress. The relative portion of crack initiation drastically decreased at high stress with increasing salt concentration. These results revealed that the corrosion damage resulting from salt concentration, whether LSC or HSC, did not impact the relative duration of crack initiation life compared to the propagation life at low stress. As stress increased, however, salt concentration became increasingly important as the reduction of crack initiation life was more strongly related to salt concentration.

4.4.2 Crack Growth Rates

Crack growth rates were determined to reveal what influences corrosion damage (by pre-corrosion conditions of salt concentration) and stress level had on crack propagation. The crack growth rates were illustrated in two forms. It was shown that the crack growth rate was primarily dependent on the stress level at which the sample was tested. This suggested that corrosion damage impacted the total fatigue life via crack initiation as opposed to crack propagation.

4.4.3 Oxidation

A small topographically distinct region was present in the vicinity of the fatigue crack initiation site on four of the corroded samples. This region appeared on the crack surface of corroded samples that had fatigue lives longer than 10,000 cycles. This region was determined to be a pronounced oxide layer, and the conditions of these fatigue tests met the criteria behind similar observations of oxidation in other studies. Though a full investigation would have reached beyond the scope of this study, a small investigation was undertaken which found a relationship between the size of the oxide region and fatigue life, and a sample was evaluated using STEM and EDS to assess the nature of the oxide. Two hypotheses were postulated: (1) the oxidation mechanism was time-based (longer fatigue life corresponding to a larger oxide region), and (2) residual salts

remained with corrosion product in the pit. It was concluded that aspects of both hypotheses played a role, but further research would have to be performed to pinpoint the mechanisms behind these oxide regions proximate to the crack formation site.

4.5 Future Work

This study involved a relatively broad approach to the effects of corrosion damage on a nickel-based superalloy in which some knowledge gaps could still be filled, and some clarifications could still be made.

One topic where future work would benefit the materials science and engineering field would be the effects of pit spacing on fatigue. It is assumed that pits that are close together build higher stress concentration than a single pit in isolation. This study suggested that closer pit spacing is deleterious for fatigue behavior, but more data would be required to make a firm claim. Additional ME3 samples would help this endeavor, as well as provide additional support for the trends observed in this study, but decreasing the size (and therefore increasing the number) of the local regions would be insightful, at least to see the effect that the size of local regions has on the results of regional pitting metrics (and possibly on the results of the other regional metrics as well). Huang et al. [78] recently suggested that the stress/strain fields of neighboring, equally sized, pits are most significant when their centers are within two diameter lengths apart and that the interaction effects become much less significant beyond that distance. In fact, they suggested that effects of a neighboring pit enhance stress intensity when they are aligned perpendicular (or nearly perpendicular, i.e. within 20° - 30° of 90°) to an applied load and that these effects decrease when the pits move from perpendicular to parallel alignment with the load.

Another topic where future work would benefit is the role of oxidation during fatigue loading. It is understood oxidation can harm the fatigue performance of a nickel-based superalloy under fatigue loading, but the importance of its role is still not fully understood as the samples that showed oxidation on the crack surface were able to endure fatigue loading, exhibiting fatigue lives similar to those of a few pristine samples.

Future work that could provide additional insight to the effects of oxidation on fatigue of ME3 could include similar fatigue test conditions as those in this study but with all corrosion product left on the sample surfaces, i.e. no cleaning of the samples between baking and testing. Such an

investigation could be compared with the results of this study by assessing the crack initiation and propagation processes when no corrosion product is cleaned off of the surface.

References

- [1] J. Tong, S. Dalby, J. Byrne, M.B. Henderson, M.C. Hardy, Creep, fatigue and oxidation in crack growth in advanced nickel base superalloys, *Int. J. Fatigue*. 23 (2001) 897–902. doi:10.1016/S0142-1123(01)00049-4.
- [2] T.P. Gabb, J. Telesman, B. Hazel, D.P. Mourer, The effects of hot corrosion pits on the fatigue resistance of a disk superalloy, *J. Mater. Eng. Perform.* 19 (2010) 77–89. doi:10.1007/s11665-009-9399-5.
- [3] M.N. Task, B. Gleeson, F.S. Pettit, G.H. Meier, The effect of microstructure on the type II hot corrosion of Ni-base MCrAlY alloys, *Oxid. Met.* 80 (2013) 125–146. doi:10.1007/s11085-013-9405-z.
- [4] J. Belan, L. Kucharikova, A. Vasko, E. Tillova, The influence of high temperature on DV-2 jet engine Ni-based superalloy turbine blade degradation, *Mater. Today Proc.* 4 (2017) 5743–5748. doi:10.1016/j.matpr.2017.06.039.
- [5] J. Stringer, Hot corrosion of high-temperature alloys, *Annu. Rev. Mater. Sci.* 7 (1977) 477–509. doi:10.1146/annurev.ms.07.080177.002401.
- [6] K.S. Chan, M.P. Enright, J.P. Moody, Development of a Probabilistic Methodology for Predicting Hot Corrosion Fatigue Crack Growth Life of Gas Turbine Engine Disks, *J. Eng. Gas Turbines Power.* 136 (2013) 22505. doi:10.1115/1.4025555.
- [7] F. Pettit, Hot Corrosion of Metals and Alloys, *Oxid. Met.* 76 (2011) 1–21. doi:10.1007/s11085-011-9254-6.
- [8] J. Nesbitt, T. Gabb, S. Draper, B. Miller, I. Locci, Coatings for Oxidation and Hot Corrosion Protection of Disk Alloys, in: *ICMCTF*, San Diego, CA, 2017.
- [9] J.L. Smialek, J.A. Nesbitt, T.P. Gabb, A. Garg, R.A. Miller, Hot corrosion and low cycle fatigue of a Cr₂AlC-coated superalloy, *Mater. Sci. Eng. A.* 711 (2018) 119–129. doi:10.1016/j.msea.2017.10.098.
- [10] J.H. Perepezko, High temperature environmental resistant Mo-Si-B based coatings, *Int. J. Refract. Met. Hard Mater.* 71 (2018) 246–254. doi:10.1016/j.ijrmhm.2017.11.033.
- [11] D.J. Young, *High Temperature Oxidation and Corrosion of Metals*, Elsevier, Ltd., 2008.
- [12] A. Pineau, S.D. Antolovich, High temperature fatigue of nickel-base superalloys - A review with special emphasis on deformation modes and oxidation, *Eng. Fail. Anal.* 16 (2009) 2668–2697. doi:10.1016/j.engfailanal.2009.01.010.
- [13] H.S. Kitaguchi, H.Y. Li, H.E. Evans, R.G. Ding, I.P. Jones, G. Baxter, P. Bowen, Oxidation ahead of a crack tip in an advanced Ni-based superalloy, *Acta Mater.* 61 (2013) 1968–1981. doi:10.1016/j.actamat.2012.12.017.
- [14] R. Molins, G. Hochstetter, J.C. Chassigne, E. Andrieu, Oxidation effects on the fatigue crack growth behaviour of alloy 718 at high temperature, *Acta Mater.* 45 (1997) 663–674. doi:10.1016/S1359-6454(96)00192-9.

- [15] G. Cao, Y. Wang, G. Tang, Properties of NiCrAlY coatings fabricated on superalloy GH4169 by electrospark deposition, *Int. J. Adv. Manuf. Technol.* (2017). doi:10.1007/s00170-017-1162-8.
- [16] N. Eliaz, G. Shemesh, R.M. Latanision, Hot corrosion in gas turbine components, *Eng. Fail. Anal.* 9 (2002) 31–43. doi:10.1016/S1350-6307(00)00035-2.
- [17] J.T. Burns, J.M. Larsen, R.P. Gangloff, Driving forces for localized corrosion-to-fatigue crack transition in Al-Zn-Mg-Cu, *Fatigue Fract. Eng. Mater. Struct.* 34 (2011) 745–773. doi:10.1111/j.1460-2695.2011.01568.x.
- [18] R.I. Stephens, A. Fatemi, R.R. Stephens, H.O. Fuchs, Stress-Life (S-N) behavior, in: *Met. Fatigue Eng.*, 2nd ed., John Wiley & Sons, Inc., 2001.
- [19] A. Kolios, S. Srikanth, K. Salonitis, Numerical Simulation of Material Strength Deterioration due to Pitting Corrosion, *Procedia CIRP.* 13 (2014) 230–236. doi:10.1016/j.procir.2014.04.040.
- [20] D. Mantha, S. Fawaz, Standardized Test Method for Corrosion Pit-to- Fatigue Crack Transition in AA7075-T651 Aluminum Alloy, *ASTM Int.* (2014). doi:10.4028/www.scientific.net/AMR.891-892.205.
- [21] S. Zhou, A. Turnbull, Influence of pitting on the fatigue life of a turbine blade steel, *Fatigue Fract. Eng. Mater. Struct.* 22 (1999) 1083–1093. doi:10.1046/j.1460-2695.1999.00226.x.
- [22] S.I. Rokhlin, J.-Y. Kim, H. Nagy, B. Zoofan, Effect of pitting corrosion on fatigue crack initiation and fatigue life, *Eng. Fract. Mech.* 62 (1999) 425–444. doi:10.1016/S0013-7944(98)00101-5.
- [23] E. Malitckii, H. Remes, P. Lehto, Y. Yagodzinsky, S. Bossuyt, H. Hänninen, Strain accumulation during microstructurally small fatigue crack propagation in bcc Fe-Cr ferritic stainless steel, *Acta Mater.* 144 (2018) 51–59. doi:10.1016/j.actamat.2017.10.038.
- [24] R.I. Stephens, A. Fatemi, R.R. Stephens, H.O. Fuchs, Fatigue mechanisms and microscopic Features, in: *Met. Fatigue Eng.*, 2nd ed., John Wiley & Sons, Inc., 2001.
- [25] J.D. Hochhalter, D.J. Littlewood, R.J. Christ, M.G. Veilleux, J.E. Bozek, A.R. Ingraffea, A.M. Maniatty, A geometric approach to modeling microstructurally small fatigue crack formation: II. Physically based modeling of microstructure-dependent slip localization and actuation of the crack nucleation mechanism in AA 7075-T651, *Model. Simul. Mater. Sci. Eng.* 18 (2010). doi:10.1088/0965-0393/18/4/045004.
- [26] T.C. Lindley, P. McIntyre, P.J. Trant, Fatigue-crack initiation at corrosion pits, *Met. Technol.* 9 (1982). doi:https://doi.org/10.1179/030716982803286403.
- [27] S.R. Lampman, ed., *ASM Handbook*, Vol. 19, F, ASM International, Metals Park, OH, 1996.
- [28] N.E. Dowling, *Mechanical Behavior of Materials*, 2000. <http://www.tandfonline.com/doi/abs/10.1080/10426910008913020>.

- [29] K.K. Sankaran, R. Perez, K. V Jata, Effects of pitting corrosion on the fatigue behavior of aluminum alloy 7075-T6 : modeling and experimental studies, 297 (2001) 223–229.
- [30] Dolley, Lee, Wei, The effect of pitting corrosion on fatigue life, *Fatigue Fract. Eng. Mater. Struct.* 23 (2000) 555–560. doi:10.1046/j.1460-2695.2000.00323.x.
- [31] W. Zhang, G. Li, Q. Zhang, G. Yang, Comprehensive damage evaluation of localized spallation of thermal barrier coatings, *J. Adv. Ceram.* 6 (2017) 230–239.
- [32] P.S. Pao, S.J. Gill, C.R. Feng, On fatigue crack initiation from corrosion pits in 7075-T7351 aluminum alloy, *Scr. Mater.* 43 (2000) 391–396. doi:10.1016/S1359-6462(00)00434-6.
- [33] J. Congleton, R.A. Olieh, R.N. Parkins, Corrosion-fatigue crack nucleation in 1.5Mn-0.5Si Steel, *Met. Technol.* 9 (1982). doi:10.1179/030716982803286133.
- [34] G.S. Chen, C.M. Liao, K.C. Wan, M. Gao, R.P. Wei, Pitting corrosion and fatigue crack nucleation, *Am. Soc. Test. Mater.* 1298 (1997) 18–31.
- [35] G.S. Chen, K.-C. Wan, M. Gao, R.P. Wei, T.H. Flournoy, Transition from pitting to fatigue crack growth—modeling of corrosion fatigue crack nucleation in a 2024-T3 aluminum alloy, *Mater. Sci. Eng. A.* 219 (1996) 126–132. doi:10.1016/S0921-5093(96)10414-7.
- [36] X. Zhang, S. Li, R. Liang, R. Akid, Effect of corrosion pits on fatigue life and crack initiation, 13th Int. Conf. Fract. (2013) 1–9.
- [37] W.G. King, Critical corrosion pit depth for fatigue crack initiation in 2024-T3, 6061-T6 and 7075-T6 aluminum alloys, 2006. file:///C:/Users/mse334/Downloads/KingJr_okstate_0664M_2049 (2).pdf.
- [38] M. Müller, Theoretical considerations on corrosion fatigue crack initiation, *Metall. Trans.* 13 (1982) 649–655.
- [39] J. Ma, B. Zhang, J. Wang, G. Wang, E.H. Han, W. Ke, Anisotropic 3D growth of corrosion pits initiated at MnS inclusions for A537 steel during corrosion fatigue, *Corros. Sci.* 52 (2010) 2867–2877. doi:10.1016/j.corsci.2010.04.036.
- [40] Y. Huang, S.T. Tu, F.Z. Xuan, Pit to crack transition behavior in proportional and non-proportional multiaxial corrosion fatigue of 304 stainless steel, *Eng. Fract. Mech.* 184 (2017) 259–272. doi:10.1016/j.engfracmech.2017.08.019.
- [41] S. Ishihara, T. Goshima, A.J. Mcevily, S. Sunada, S. Nomata, CORROSION-PIT-GROWTH BEHAVIOUR DURING THE CORROSION FATIGUE PROCESS IN ALUMINUM, in: ICF, n.d. <http://www.gruppofrattura.it/ocs/index.php/ICF/ICF10/paper/viewFile/4504/6512>.
- [42] B.Y. Fang, R.L. Eadie, W.X. Chen, M. Elboudjaini, Pit to crack transition in X-52 pipeline steel in near neutral pH environment Part 1 - formation of blund cracks from pits under cyclic loading, *Int. J. Corros. Process. Corros. Control.* 45 (2010).
- [43] M. Cerit, K. Genel, S. Eksi, Numerical investigation on stress concentration of corrosion

- pit, Eng. Fail. Anal. 16 (2009) 2467–2472. doi:10.1016/j.engfailanal.2009.04.004.
- [44] H.M. Mohammad, Prediction of Pitting Corrosion Characteristics using Artificial Neural Networks, 60 (2012) 4–8.
- [45] K.A. Rozman, M. Ziomek-Moroz, S. Bullard, J.J. Kruzic, J.A. Hawk, Localized Corrosion and Fatigue Behavior of Ultra-Deep Drilling Alloys, Doe-Netl. (2014).
- [46] R. Ghosh, A. Venugopal, G.S. Rao, P. Ramesh Narayanan, B. Pant, R.M. Cherian, Effect of Temper Condition on the Corrosion and Fatigue Performance of AA2219 Aluminum Alloy, J. Mater. Eng. Perform. 27 (2018) 423–433. doi:10.1007/s11665-018-3125-0.
- [47] D.J. Child, J. Meldrum, P. Onwuarolu, Corrosion-fatigue testing of Ni-based superalloy RR1000, Mater. Sci. Technol. (United Kingdom). 33 (2017) 1040–1047. doi:10.1080/02670836.2016.1242827.
- [48] J.R. Donahue, J.T. Burns, Effect of chloride concentration on the corrosion-fatigue crack behavior of an age-hardenable martensitic stainless steel, Int. J. Fatigue. 91 (2016) 79–99. doi:10.1016/j.ijfatigue.2016.05.022.
- [49] N.E.C. Co, J.T. Burns, Effects of macro-scale corrosion damage feature on fatigue crack initiation and fatigue behavior, Int. J. Fatigue. 103 (2017) 234–247. doi:10.1016/j.ijfatigue.2017.05.028.
- [50] G.B. Olson, H.J. Jou, J.-W. Jung, J.T. Sebastian, A. Misra, I. Locci, D. Hull, Precipitation model validation in 3rd generation aeroturbine disc alloys, 11th Int. Symp. Superalloys. 3 (2008) 923–932. doi:10.7449/2008/Superalloys_2008_923_932.
- [51] Y.F. Gu, H. Harada, T. Fukuda, D. Ping, A. Mitsuhashi, K. Kato, T. Kobayashi, J. Fujioka, C. Cui, Development of Ni-Co base alloys for high-temperature disk applications, Superalloys. (2008) 53–61. doi:\url{10.7449/2008/Superalloys{_}2008{_}53{_}61}.
- [52] M. Ashby, H. Shercliff, D. Cebon, Materials Engineering, Science, Processing, and Design, 2nd ed., Butterworth-Heinemann, Burlington, MA, 2010. 978-1-85617-743-6.
- [53] Hardness Calculation - Vickers Indenter, Tribonet - About Tribol. (2017). <http://www.tribonet.org/hardness-calculation-vickers-indenter/>.
- [54] Hardness Conversion Table, Magmaweld. (2015). http://www.magmaweld.com/hardness_conversion_table.html.
- [55] T.P. Gabb, J. Telesman, P.T. Kantzos, K. O’Connor, Characterization of the Temperature Capabilities of Advanced Disk Alloy ME3, 2002.
- [56] G.S. Chen, M. Gao, D.G. Harlow, R.P. Wei, Corrosion and corrosion fatigue of airframe aluminum alloys, (1995) 157–173.
- [57] B. Holme, O. Lunder, Characterisation of pitting corrosion by white light interferometry, Corros. Sci. 49 (2007) 391–401. doi:10.1016/j.corsci.2006.04.022.
- [58] E.Q. Contreras, J. Huang, R.S. Posusta, D.K. Sharma, C. Yan, P. Guraieb, M.B. Tomson, R.C. Tomson, Optical measurement of uniform and localized corrosion of C1018 , SS 410

- , and Inconel 825 alloys using white light interferometry, *Corros. Sci.* 87 (2014) 383–391. doi:10.1016/j.corsci.2014.06.046.
- [59] S. Geary, H.N. McMurray, A.C.A. de Vooy, High resolution characterization of pitting corrosion using a novel environmental SVET and white light interferometry, *ECS Trans.* 50 (2013) 37–51. doi:10.1149/05047.0037ecst.
- [60] E.L. Novak, N.R. Blewett, T. Stout, **TRIBOLOGY AND CORROSION EVALUATION USING WHITE-LIGHT INTERFEROMETRY**, (n.d.).
- [61] G.N. Frantzikonis, L.B. Simon, J. Woo, T.E. Matikas, Multiscale characterization of pitting corrosion and application to an aluminum alloy, *Eur. J. Mech. A/Solids.* 19 (2000) 309–318. doi:10.1016/S0997-7538(00)00162-5.
- [62] C. Merola, H. Cheng, K. Schwenzfeier, K. Kristiansen, Y. Chen, H.A. Dobbs, J.N. Israelachvili, In situ nano- to microscopic imaging and growth mechanism of electrochemical dissolution (e . g . , corrosion) of a confined metal surface, *Proc. Natl. Acad. Sci.* 114 (2017) 9541–9546. doi:10.1073/pnas.1708205114.
- [63] Esri, How average nearest neighbor distance (spatial statistics) works, (n.d.). http://resources.esri.com/help/9.3/ArcGISDesktop/com/Gp_ToolRef/spatial_statistics_tools/how_average_nearest_neighbor_distance_spatial_statistics_works.htm.
- [64] T.P. Gabb, J. Telesman, L. Ghosn, Factors influencing dwell fatigue cracking in notches of powder metallurgy superalloys, (2011).
- [65] A.D. Spear, S. Fai, J.F. Lind, R.M. Suter, A.R. Ingraffea, Three-dimensional characterization of microstructurally small fatigue-crack evolution using quantitative fractography combined with post-mortem X-ray tomography and high-energy X-ray diffraction microscopy, *Acta Mater.* 76 (2014) 413–424.
- [66] S. Kim, J.T. Burns, R.P. Gangloff, Fatigue crack formation and growth from localized corrosion in Al – Zn – Mg – Cu, *Eng. Fract. Mech.* 76 (2009) 651–667. doi:10.1016/j.engfracmech.2008.11.005.
- [67] S.A. Barter, L. Molent, D. Science, T. Organisation, **MARKER LOADS FOR QUANTITATIVE FRACTOGRAPHY OF FATIGUE CRACKS IN AEROSPACE ALLOYS**, in: *ICAF Symp.*, 2009: pp. 15–16.
- [68] J.T. Burns, S. Kim, R.P. Gangloff, Effect of corrosion severity on fatigue evolution in Al – Zn – Mg – Cu, *Corros. Sci.* 52 (2010) 498–508. doi:10.1016/j.corsci.2009.10.006.
- [69] J.T. Burns, J.M. Larsen, R.P. Gangloff, Effect of initiation feature on microstructure-scale fatigue crack propagation in Al-Zn-Mg-Cu, *Int. J. Fatigue.* 42 (2012) 104–121. doi:10.1016/j.ijfatigue.2011.08.001.
- [70] M. McDonald, R. Boykett, M. Jones, **QUANTITATIVE FRACTOGRAPHY MARKERS FOR DETERMINING FATIGUE CRACK GROWTH RATES IN ALUMINIUM AND TITANIUM AIRCRAFT STRUCTURES**, in: *Int. Congr. Aeronaut. Sci.*, 2012: pp. 1–10. http://www.icas.org/ICAS_ARCHIVE/ICAS2012/PAPERS/413.PDF.
- [71] S.A. Willard, Use of Marker Bands for Determination and Crack Coupons of Fatigue

- Crack Growth Rates Front Shapes in Pre-Corroded, 1997.
<https://ntrs.nasa.gov/archive/nasa/casi.ntrs.nasa.gov/19980019296.pdf>.
- [72] R. Dainty, Use of “Marker Blocks” As An Aid in Quantitative Fractography in Full-Scale Aircraft Fatigue Testing : A Case Study, *ASTM Int.* (1984) 285–308.
<https://compass.astm.org/download/STP37117S.15220.pdf>.
- [73] D. Stanley, J. Awerbuch, T. Tan, Reconstruction of fatigue crack growth in aluminum lithium and aluminum copper fastened lap joints under marker band loading, *Int. J. Fatigue.* 103 (2017) 516–532. doi:10.1016/j.ijfatigue.2017.06.027.
- [74] K. van der Walde, B.M. Hillberry, Initiation and shape development of corrosion-nucleated fatigue cracking, *Int. J. Fatigue.* 29 (2007) 1269–1281.
 doi:10.1016/j.ijfatigue.2006.10.010.
- [75] O. Jilani, N. Njah, P. Ponthiaux, Transition from intergranular to pitting corrosion in fine grained aluminum processed by equal channel angular pressing, *Corros. Sci.* 87 (2014) 259–264. doi:10.1016/j.corsci.2014.06.031.
- [76] R.I. Stephens, A. Fatemi, R.R. Stephens, H.O. Fuchs, General S-N Behavior, in: *Met. Fatigue Eng.*, 2nd ed., John Wiley & Sons, Inc., 2001.
- [77] J.J. Medved, M. Breton, P.E. Irving, Corrosion pit size distributions and fatigue lives — a study of the EIFS technique for fatigue design in the presence of corrosion, *Int. J. Fatigue.* 26 (2004) 71–80. doi:10.1016/S0142-1123(03)00069-0.
- [78] Y. Huang, T. Gang, L. Chen, Interacting effects induced by two neighboring pits considering relative position parameters and pit depth, *Materials (Basel).* 10 (2017).
 doi:10.3390/ma10040398.
- [79] A. Turnbull, D.A. Horner, B.J. Connolly, Challenges in modelling the evolution of stress corrosion cracks from pits, *Eng. Fract. Mech.* 76 (2009) 633–640.
 doi:10.1016/j.engfracmech.2008.09.004.
- [80] Standard test method for measurement of fatigue crack growth rates, E647 (2013).
- [81] S. Suresh, R.O. Ritchie, Propagation of short fatigue cracks, *Int. Met. Rev.* 29 (1984) 445–475. doi:10.1179/imtr.1984.29.1.445.
- [82] Newman, J.C. Jr., A review of modelling small-crack behavior and fatigue-life predictions for aluminum alloys, *Fatigue Fract. Eng. Mater. Struct.* 17 (1994) 429–439.
 doi:10.1111/j.1460-2695.1994.tb00242.x.
- [83] W.A. Herman, R.W. Hertzberg, R. Jaccard, A simplified laboratory approach for the prediction of short crack behavior in engineering structures, *Fatigue Fract. Eng. Mater. Struct.* 11 (1988) 303–320. doi:10.1111/j.1460-2695.1988.tb01183.x.
- [84] L.G. Zhao, J. Tong, M.C. Hardy, Prediction of crack growth in a nickel-based superalloy under fatigue-oxidation conditions, *Eng. Fract. Mech.* 77 (2010) 925–938.
 doi:10.1016/j.engfracmech.2010.02.005.
- [85] D.G. Leo Prakash, M.J. Walsh, D. Maclachlan, A.M. Korsunsky, Crack growth micro-

- mechanisms in the IN718 alloy under the combined influence of fatigue, creep and oxidation, *Int. J. Fatigue*. 31 (2009) 1966–1977. doi:10.1016/j.ijfatigue.2009.01.023.
- [86] H. Ghonem, D. Zheng, Depth of intergranular oxygen diffusion during environment-dependent fatigue crack growth in alloy 718, *Mater. Sci. Eng. A*. 150 (1992) 151–160. doi:10.1016/0921-5093(92)90107-C.
- [87] M.R. Bache, W.J. Evans, M.C. Hardy, The effects of environment and loading waveform on fatigue crack growth in Inconel 718, *Int. J. Fatigue*. 21, Supple (1999) S69–S77. doi:10.1016/S0142-1123(99)00057-2.
- [88] C.F. Miller, G.W. Simmons, R.P. Wei, Evidence for internal oxidation during oxygen enhanced crack growth in P/M Ni-based superalloys, *Scr. Mater.* 48 (2003) 103–108. doi:10.1016/S1359-6462(02)00355-X.
- [89] K. Kussmaul, D. Blind, V. Lapple, New observations on the crack growth rate of low grade ferritic steels under constant active load in high-temperature water, *Nucl. Eng. Des.* 168 (1997) 53–75.
- [90] H. Andersson, C. Persson, In-situ SEM study of fatigue crack growth behaviour in IN718, *Int. J. Fatigue*. 26 (2004) 211–219. doi:10.1016/S0142-1123(03)00172-5.
- [91] A. Turnbull, L. Wright, L. Crocker, New insight into the pit-to-crack transition from finite element analysis of the stress and strain distribution around a corrosion pit, *Corros. Sci.* 52 (2010) 1492–1498. doi:10.1016/j.corosci.2009.12.004.